Journal of
Mechanics of Materials and Structures

Volume 15, No. 5 December 2020

msp

JOURNAL OF MECHANICS OF MATERIALS AND STRUCTURES

msp.org/jomms

Founded by Charles R. Steele and Marie-Louise Steele

Cover photo: Wikimedia Commons

See msp.org/jomms for submission guidelines.

JoMMS (ISSN 1559-3959) at Mathematical Sciences Publishers, 798 Evans Hall #6840, c/o University of California, Berkeley, CA 94720-3840, is published in 10 issues a year. The subscription price for 2020 is US $660/year for the electronic version, and $830/year (+$60, if shipping outside the US) for print and electronic. Subscriptions, requests for back issues, and changes of address should be sent to MSP.

JoMMS peer-review and production is managed by EditFLOW® from Mathematical Sciences Publishers.

PUBLISHED BY

mathematical sciences publishers

nonprofit scientific publishing

http://msp.org/

JOURNAL OF MECHANICS OF MATERIALS AND STRUCTURES
Vol. 15, No. 5, 2020
https://doi.org/10.2140/jomms.2020.15.555

APPROXIMATE CONFORMAL MAPPINGS AND ELASTICITY PROBLEMS FOR NONCIRCULAR TUBES

DAMIR F. ABZALILOV, PYOTR N. IVANSHIN AND ELENA A. SHIROKOVA

We present a method for analytic stress evaluation in elliptic and oval tubes based on approximate conformal mappings from annuli onto oval and elliptical doubly connected domains. The approximate conformal mapping is realized by the boundary reparametrization method. We also solve two elasticity problems for such tubes.

1. Introduction

Elastic deformations of circular tubes always attracted attention of scientists [Yella Reddy and Reid 1979; Moore 1990; Nayak and Mondal 2011]. Recently the researchers began to consider noncircular tubes with flattened, quasi-triangular, quasi-square, elliptical, rectangular and hexagon cross sections [Bazehhouri and Rezaeepazhand 2012; Baroutaji et al. 2014]. Such tubes can serve, for example, as energy absorbers in different mechanisms. Also the scientists analyzed the stresses in tubes under different load, compression and twist deformations applying both FEM and analytical methods [Zheng et al. 2015; Rizzetto et al. 2019]. Elliptic and oval tubes are manufactured and sold by different modern firms. The developing analytic technique and the computer progress allow appearance of new analytical evaluation methods of the tube characteristics.

We apply the boundary reparametrization method [Abzalilov and Shirokova 2017] for construction of the approximate conformal mapping from an annulus onto a doubly connected domain and then consider the analytical solution of some plane problems based on the analytic function theory [Muskhelishvili 1977]. Similar problem for a simply connected domain was solved in [Ivanshin and Shirokova 2016]. We apply the formulas of [Muskhelishvili 1977] for evaluation of the tubes torsion. We also consider the 3D element of the tubes with the oval and elliptic cuts and its deformation under bending.

The basic ideas of the boundary reparametrization method were presented in [Shirokova 2014] where the author constructed a method of the unit disk conformal mapping onto a simply connected domain. The boundary reparametrization method is based on application of an integral equation solution to finding the reparametrization function $t(\theta)$, $\theta \in [0, 2\pi]$. This reparametrization function transformes the representation $z(t)$ of the given domain boundary to the boundary value $z(t(\theta))$ of the function analytic in some circular domain (e.g., the unit disk, the annulus, the unit disk with concentric circular slits). We restore the analytic function in the circular domain via the Cauchy integral formula after we find the boundary values of the function.

We find the approximate solution of the integral equation reducing the integral equation to an infinite linear system and then to a truncated finite system. We reduce the Cauchy integral representation of

Keywords: conformal mapping, elasticity theory, stresses.

the analytic function in an annulus to a Laurent series in this annulus. We find the essential coefficients of the Laurent series in order to construct the approximate analytic function in the form of a Laurent polynomial applicable to further investigations.

2. Laurent polynomial approximate conformal mapping from an annulus onto an oval cut and an elliptic cut

We approximately map the annuli onto the oval tube cross-section (Figure 1, left) and onto the elliptical tube cross-section (Figure 1, right) applying the boundary reparametrization method [Abzalilov and Shirokova 2017].

First we approximate the boundary curves – the interior curve $z = z_1(t)$, $t \in [0, 2\pi]$, and the exterior curve $z = z_2(t)$, $t \in [0, 2\pi]$ – of each of the cross-sections by the Fourier polynomials

$$z_j(t) = \sum_{k=-T_j}^{T_j} C_k^j e^{ikt}, \quad t \in [0, 2\pi], \quad j = 1, 2.$$

The boundary reparametrization method is to find the reparametrizing functions $t_j(\theta)$, $\theta \in [0, 2\pi]$, $j = 1, 2$, such that the expressions

$$\sum_{k=-T_j}^{T_j} C_k^j e^{ikt_j(\theta)} = \sum_{k=-M_j}^{M_j} D_k^j e^{ik\theta}, \quad j = 1, 2,$$

are the boundary values (at the interior circle $|\zeta| = r$ and at the exterior circle $|\zeta| = 1$) of a function analytic in the annulus $r < |\zeta| < 1$.

Consider a finite doubly-connected domain D_z bounded by the curves $z = z_j(t)$, $t \in [0, 2\pi]$, $j = 1, 2$. We consider at first the analytic in the domain D_z function $\zeta(z)$ which maps the domain D_z to an annulus $D_\zeta = \{\zeta : r < |\zeta| < 1\}$ and the analytic in D_z function $\log \frac{z}{\zeta(z)}$. Let $\theta_s(t)$, $s = 1, 2$, be the polar angle of the annulus boundary point corresponding to the boundary point $z_s(t)$ of the domain D_z. We introduce the function $q_s(t) = \arg z_s(t) - \theta_s(t)$, $s = 1, 2$. We apply the necessary and sufficient condition for $\log \frac{z}{\zeta(z)}$ to be analytic in D_z and obtain the integral Fredholm equation for the vector function $(q_1(t), q_2(t))$, $t \in [0, 2\pi]$:

$$q_s(t) = -\sum_{j=1}^{2} \frac{1}{\pi} \int_0^{2\pi} \log \frac{|z_j(\tau)|}{R_j} \left(\log |z_j(\tau) - z_s(t)|\right)'_\tau d\tau + \sum_{j=1}^{2} \frac{1}{\pi} \int_0^{2\pi} q_j(\tau) \left(\arg[z_j(\tau) - z_s(t)]\right)'_\tau d\tau, \quad s = 1, 2,$$

as in [Abzalilov and Shirokova 2017], where $R_1 = r$, $R_2 = 1$. Now the principal value singular integral can be represented as

$$\frac{1}{\pi} \int_0^{2\pi} \log \frac{|z_j(\tau)|}{R_j} \left(\log |z_j(\tau) - z_j(t)|\right)'_\tau d\tau \equiv \frac{1}{2\pi} \int_0^{2\pi} \log \frac{|z_j(\tau)|}{R_j} \cot \frac{\tau - t}{2} d\tau + \frac{1}{\pi} \int_0^{2\pi} \log \frac{|z_j(\tau)|}{R_j} L_j(\tau, t)\, d\tau;$$

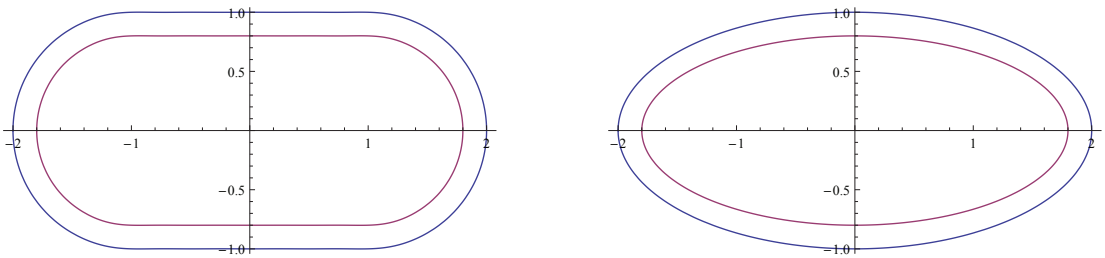

Figure 1. Shape of the cross-section of the oval (left) and elliptical (right) tubes.

here the kernel $L_j(\tau, t)$ is continuous. If the value of r were known, the integral

$$\frac{1}{2\pi}\int_0^{2\pi} \log\frac{|z_1(\tau)|}{r}\cot\frac{\tau-t}{2}d\tau$$

could be calculated via the Hilbert formula. Similar integral equation was applied to find the function $q(t)$ and the reparametrizing function $t(\theta)$ in the case of a simply connected domain [Shirokova 2014].

We do not know the value of r in the case of a doubly connected domain. So we have to differentiate both sides of the previous integral equation. After integrating the right-hand side of the resulting equation by parts, we obtain the following relations on the functions $q_s'(t)$:

$$q_s'(t) = -\sum_{j=0}^{1}\frac{1}{\pi}\int_0^{2\pi} q_j'(\tau)\left(\arg[z_j(\tau)-z_s(t)]\right)_t' d\tau + \sum_{j=0}^{1}\frac{1}{\pi}\int_0^{2\pi}[\log|z_j(\tau)|]'\left(\log|z_j(\tau)-z_s(t)|\right)_t' d\tau,$$
$$s = 1, 2.$$

We separate the singularities in the kernel $(\log|z_s(\tau)-z_s(t)|)_t'$ in the form of $\cot\frac{\tau-t}{2}$ and obtain the corresponding integrals with this principal value singular kernel exactly as it was described above.

The final integral equation can be represented as the Fredholm equation with an unknown vector function $M = (q_1'(s), q_2'(s))$ in the form of $M = AM + B$. If the unknown functions have the form

$$q_s'(t) = \sum_{j=1}^{\infty}\alpha_{j,s}\cos jt + \beta_{j,s}\sin jt,\ \ t\in[0, 2\pi],\quad s = 1, 2.$$

we reduce the integral equation to the solution of an infinite linear system with unknown Fourier coefficients of the functions $q_s'(t)$, $s = 1, 2$. Then we reduce the infinite linear system to a truncated linear system, a 2D generalization of the following result:

Lemma [Ivanshin and Shirokova 2016]. Let there exist the numbers $j, m > 1$ and a constant $U > 0$ so that $\left|\partial^{j+m}G(\tau, t)/\partial t^j\partial\tau^m\right| \le U$ and the function $Y(t)$ possess the bounded second derivative: $|Y''(t)| < T$. Then the approximate solution of the uniquely resolvable Fredholm integral equation of the second kind

$$X(t) = \int_0^{2\pi} G(\tau, t)X(\tau)\,d\tau + Y(t),$$

where $Y(t)$ is 2π periodic and $G(\tau, t)$ is 2π periodic with respect to both variables, can be reduced to

the solution of a finite linear system with error estimated by $O(1/N^2)$. Here N is the rank of the finite linear system.

Now we obtain the monotone functions $\theta_s(t) = \arg z_s(t) - q_s(t)$, $s = 1, 2$. Note that one of the functions $q_s(t)$, $s = 1, 2$, can be restored via its derivative with an arbitrary constant summand, e.g. 0, but the other one must contain the special constant summand, because the function $\log(z(\zeta)/\zeta)/\zeta$ must be analytical in the annulus D_ζ. So the relation

$$\int_0^{2\pi} q_1(t)\theta_1'(t)\,dt = -\int_0^{2\pi} q_2(t)\theta_2'(t)\,dt$$

holds true due to Cauchy theorem. We put the expressions $\theta_s(t) = \arg z_s(t) - q_s(t)$ into the last relation and achieve the equality

$$\int_0^{2\pi} q_1(t)(\arg z_1(t))'dt + \int_0^{2\pi} q_2(t)(\arg z_2(t))'dt = 0,$$

which determines the value of the constant summand for the second function $q_s(t)$ restored via its derivative.

After the relations between t and θ are found at the both boundary components we can obtain the mapping function $z(\zeta)$. We restore this function via its boundary values $z(t(\theta))$ by the Cauchy integral formula. This Cauchy integral and its derivatives vanish at the point $\zeta = 0$. Therefore the inner radius r of the annulus D_ζ can be found via one of the formulas

$$\int_0^{2\pi} z_1(t)e^{ik\theta_0(t)}\theta_1'(t)\,dt + r^k \int_0^{2\pi} z_2(t)e^{ik\theta_1(t)}\theta_2'(t)\,dt = 0, \quad k = 1, 2, \ldots$$

or by the least-squares method.

The Laurent series coefficients of the analytic function $z(\zeta)$ mapping the annulus $r < |\zeta| < 1$ onto the domain D_z can be restored via the formulas

$$c_k = \frac{1}{2\pi}\int_0^{2\pi} z_1(t)e^{-ik\theta_1(t)}\theta_0'(t)\,dt, \quad k = 0, 1, 2, \ldots,$$
$$c_{-k} = -\frac{r^k}{2\pi}\int_0^{2\pi} z_1(t)e^{ik\theta_1(t)}\theta_1'(t)\,dt, \quad k = 1, 2, \ldots.$$

We tested the reparametrization method in the approximate conformal mapping of the annulus given by $2 - \sqrt{3} < |\zeta| < 1$ onto the doubly connected domain $D_z = \{z \mid |z| < 2, |z - 0.5| < 0.5\}$. The function

$$z = 2\frac{\zeta(2 + \sqrt{3}) - 1}{\zeta - 2 - \sqrt{3}}.$$

gives the exact conformal mapping of the annulus onto the given domain. We took the mapping polynomial with 200 coefficients and compared the values of the exact mapping function and the approximate mapping function at the points of the circle $|\zeta| = 0.5$. The error was less than 0.0005.

k	a_k	b_k	k	a_k	b_k	k	a_k	b_k
−17	−0.00040	0.00001	−5	−0.00165	0.00354	7	−0.00911	0.01532
−15	0.00036	0.00002	−3	−0.04314	0.01779	9	0.00178	0.00723
−13	0.00088	0.00005	−1	0.39657	0.40846	11	0.00195	0.00368
−11	−0.00135	0.00013	1	1.52248	1.44051	13	−0.00121	0.00197
−9	−0.00112	0.00035	3	0.16082	0.12051	15	−0.00035	0.00109
−7	0.00543	0.00103	5	0.00369	0.03707	17	0.00071	0.00061

Table 1. Coefficients of Laurent polynomial for oval cut and for the elliptical cut.

We apply the described reparametrization method for the oval domain and for the elliptical domain. We find the following analytic functions. The function

$$z_o(\zeta) = \sum_{k=0}^{17} a_k \zeta^k + \sum_{k=-17}^{-1} a_k \left(\frac{\zeta}{r_o}\right)^k$$

maps approximately the annulus $r_o < |\zeta| < 1$, ($r_o = 0.87785$) onto the given oval cross-section presented in Figure 1, left. The function

$$z_e(\zeta) = \sum_{k=0}^{17} b_k \zeta^k + \sum_{k=-17}^{-1} b_k \left(\frac{\zeta}{r_e}\right)^k$$

maps approximately the annulus $r_e < |\zeta| < 1$, ($r_e = 0.87432$) onto the given elliptical cross-section presented on Figure 1, right. The coefficients a_k and b_k are presented in Table 1. The absolute values of the Laurent coefficients vanish while the absolute values of their numbers increase. Therefore we take the essential polynomial coefficients' indices only in the range $[-17, 17]$. The other coefficients do not bring significant difference to the results of calculations.

We apply these mappings to the solution of two elasticity theory problems.

3. Solution of the torsion problem for the oval tube and for the elliptical tube

We consider the boundary shear stresses on the exterior surfaces of the given tubes twisted in the plane cross-sections over the center point of the cross-section. We base the torsion problem solution on relation (13) of [Muskhelishvili 1977], Chapter 7: the value of the shear stress on the outer boundary of the orthogonal cross-section of a tube is proportional to the expression

$$S(\theta) = \frac{1}{|z'(e^{i\theta})|} \operatorname{Im}\left[e^{i\theta}\left(\varphi'(e^{i\theta}) - i\overline{z(e^{i\theta})}z'(e^{i\theta})\right)\right].$$

Here $z(\zeta)$ is the Laurent polynomial mapping the corresponding annulus onto the tube cut and $\varphi(\zeta)$ is the analytic in the annulus function with the boundary condition

$$\operatorname{Im}\varphi(re^{i\theta}) = |z(re^{i\theta})|^2/2,$$

where $r = 1$ for each tube at the exterior boundary and $r = r_o$ for the oval tube or $r = r_e$ for the elliptical tube at the interior boundary.

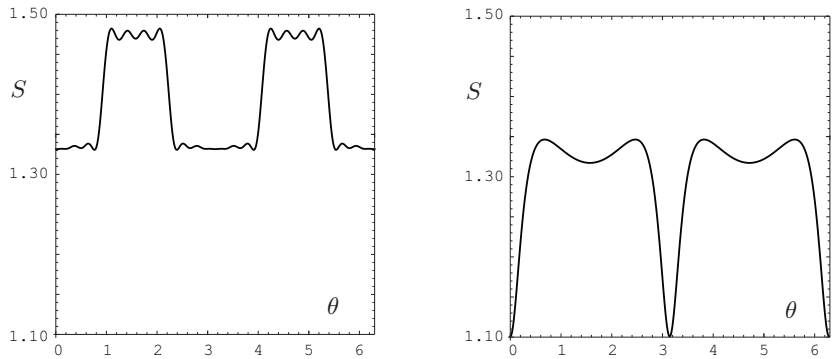

Figure 2. Stress $S(\theta)$ in the twisted oval (left) and elliptical (right) tubes.

The corresponding graphs of the function $S(\theta)$ for the oval and elliptical tubes are presented on Figure 2.

We see that the boundary shear stress of each of the given tubes twisted in the plane xOy over the cross-section center of symmetry changes from its minimal value to its maximal value in small neighbourhoods of four symmetrically located boundary points. The maximal shear stress values are larger for the oval tube. So the oval tube is more destructible then the elliptical one under twisting.

4. Spline-interpolation solution of the bending problem for the oval tube and for the elliptical tube

Consider the stresses at the exterior surfaces of the tubes in the space (x, y, h) with the cut cross-sections D parallel to the plane xOy. Let the exterior surfaces of both tubes be fixed at the level $h = 0$ and the shift in Ox direction on the exterior surfaces at the level $h = H$ equal a. Such a deformation happens when one bends the tube in Ox direction. We assume that the interior surfaces of the tubes are free from stresses. For small values of H and a we apply the linear spline-interpolation method [Ivanshin and Shirokova 2011; Shirokova 2004]. The linear spline-interpolation method of 3D elasticity problem solution for a tube is to find the stresses in this tube when the displacement coordinates at the points of a small segment $D \times [0, H]$ are assumed to be linear over the coordinate h. The problem is reduced to a set of mixed boundary value problems in an annulus.

According to the assumption the coordinates of the displacement vector take the form

$$\begin{aligned} u &= u_0(x, y) + u_1(x, y)h, \quad v = v_0(x, y) + v_1(x, y)h, \\ w &= w_0(x, y) + w_1(x, y)h, \quad (x, y) \in D, \quad h \in [0, H]. \end{aligned} \tag{1}$$

The interior surface null pressure assumption gives the relations

$$[\sigma_{k1}\cos(n, x) + \sigma_{k2}\cos(n, y) + \sigma_{k3}\cos(n, h)]_{x=x_1(s), y=y_1(s)} = 0, \quad k = 1, 2, 3,$$

for the points (x, y, h) on the interior surface of the tube segment, where σ_{kj}, $k, j = 1, 2, 3$, are tensor components, n is the unit normal to the interior surface at the corresponding point. Note that $\cos(n, h) = 0$ on the interior surface of the tube.

Due to coordinate linearity (1) on h the latter relations take the following form for the points $(x, y) = (x_1(s), y_1(s))$ of the interior boundary of D:

$$\left\{\left(\lambda\left[\frac{\partial u_0}{\partial x}+\frac{\partial v_0}{\partial y}+w_1\right]+2\mu\frac{\partial u_0}{\partial x}\right)dy_1(s)-\mu\left(\frac{\partial u_0}{\partial y}+\frac{\partial v_0}{\partial x}\right)dx_1(s)\right\}_{x=x_1(s),y=y_1(s)}=0, \tag{2}$$

$$\left\{\left(\lambda\left[\frac{\partial u_0}{\partial x}+\frac{\partial v_0}{\partial y}+w_1\right]+2\mu\frac{\partial v_0}{\partial y}\right)dx_1(s)-\mu\left(\frac{\partial u_0}{\partial y}+\frac{\partial v_0}{\partial x}\right)dy_1(s)\right\}_{x=x_1(s),y=y_1(s)}=0, \tag{3}$$

$$\left\{\left(u_1+\frac{\partial w_0}{\partial x}\right)dy_1(s)-\left(v_1+\frac{\partial w_0}{\partial y}\right)dx_1(s)\right\}_{x=x_1(s),y=y_1(s)}=0, \tag{4}$$

$$\left\{\left(\lambda\left[\frac{\partial u_1}{\partial x}+\frac{\partial v_1}{\partial y}\right]+2\mu\frac{\partial u_1}{\partial x}\right)dy_1(s)-\mu\left(\frac{\partial u_1}{\partial y}+\frac{\partial v_1}{\partial x}\right)dx_1(s)\right\}_{x=x_1(s),y=y_1(s)}=0, \tag{5}$$

$$\left\{\left(\lambda\left[\frac{\partial u_1}{\partial x}+\frac{\partial v_1}{\partial y}\right]+2\mu\frac{\partial v_1}{\partial y}\right)dx_1(s)-\mu\left(\frac{\partial u_1}{\partial y}+\frac{\partial v_1}{\partial x}\right)dy_1(s)\right\}_{x=x_1(s),y=y_1(s)}=0, \tag{6}$$

$$\left\{\frac{\partial w_1}{\partial x}dy_1(s)-\frac{\partial w_1}{\partial y}dx_1(s)\right\}_{x=x_1(s),y=y_1(s)}=0, \tag{7}$$

where λ and μ are Lame coefficients.

The boundary conditions on the exterior surface of the tube segment yield the following relations at the points $(x, y) = (x_2(s), y_2(s))$ of the exterior boundary of D:

$$u_0(x_2(s), y_2(s))=0,\quad v_0(x_2(s), y_2(s))=0,\quad w_0(x_2(s), y_2(s))=0,$$
$$u_1(x_2(s), y_2(s))H=a,\quad v_1(x_2(s), y_2(s))=0,\quad w_1(x_2(s), y_2(s))=0.$$

The equilibrium equations

$$\frac{\partial\sigma_{k1}}{\partial x}+\frac{\partial\sigma_{k2}}{\partial y}+\frac{\partial\sigma_{k3}}{\partial h}=0,\quad k=1,2,3,$$

must be met everywhere in the tube segment. Due to the displacement coordinates linearity in h the equilibrium equations take the form

$$\lambda\left\{\frac{\partial^2 u_0}{\partial x^2}+\frac{\partial^2 v_0}{\partial x\partial y}+\frac{\partial w_1}{\partial x}+\left(\frac{\partial^2 u_1}{\partial x^2}+\frac{\partial^2 v_1}{\partial x\partial y}\right)h\right\}+\mu\left\{\sum_{k=0}^{1}\left(2\frac{\partial^2 u_k}{\partial x^2}+\frac{\partial^2 u_k}{\partial y^2}+\frac{\partial^2 v_k}{\partial x\partial y}\right)h^k+\frac{\partial w_1}{\partial x}\right\}=0, \tag{8}$$

$$\lambda\left\{\frac{\partial^2 u_0}{\partial x\partial y}+\frac{\partial^2 v_0}{\partial y^2}+\frac{\partial w_1}{\partial y}+(\frac{\partial^2 u_1}{\partial x\partial y}+\frac{\partial^2 v_1}{\partial y^2})h\right\}+\mu\left\{\sum_{k=0}^{1}\left(2\frac{\partial^2 v_k}{\partial y^2}+\frac{\partial^2 u_k}{\partial x\partial y}+\frac{\partial^2 v_k}{\partial x^2}\right)h^k+\frac{\partial w_1}{\partial y}\right\}=0, \tag{9}$$

$$\lambda\left(\frac{\partial u_1}{\partial x}+\frac{\partial v_1}{\partial y}\right)+\mu\left(\frac{\partial u_1}{\partial x}+\frac{\partial v_1}{\partial y}+\frac{\partial^2 w_0}{\partial x^2}+\frac{\partial^2 w_0}{\partial y^2}+\left[\frac{\partial^2 w_1}{\partial x^2}+\frac{\partial^2 w_1}{\partial y^2}\right]h\right)=0. \tag{10}$$

The coefficients with h in relations (8) and (9) form the system

$$\begin{cases} \dfrac{\partial}{\partial x}\left[(\lambda+2\mu)\left(\dfrac{\partial u_1}{\partial x}+\dfrac{\partial v_1}{\partial y}\right)\right]-\dfrac{\partial}{\partial y}\left[\mu\left(\dfrac{\partial v_1}{\partial x}-\dfrac{\partial u_1}{\partial y}\right)\right]=0, \\ \dfrac{\partial}{\partial y}\left[(\lambda+2\mu)\left(\dfrac{\partial u_1}{\partial x}+\dfrac{\partial v_1}{\partial y}\right)\right]+\dfrac{\partial}{\partial x}\left[\mu\left(\dfrac{\partial v_1}{\partial x}-\dfrac{\partial u_1}{\partial y}\right)\right]=0, \end{cases}$$

which is equivalent to the equation

$$\frac{\partial}{\partial \bar z}\left[(\lambda+2\mu)\left(\frac{\partial u_1}{\partial x}+\frac{\partial v_1}{\partial y}\right)+i\mu\left(\frac{\partial v_1}{\partial x}-\frac{\partial u_1}{\partial y}\right)\right]=0,$$

where $z=x+iy$, $\bar z=x-iy$. So

$$(\lambda+2\mu)\left(\frac{\partial u_1}{\partial x}+\frac{\partial v_1}{\partial y}\right)+i\mu\left(\frac{\partial v_1}{\partial x}-\frac{\partial u_1}{\partial y}\right)=F_1(z),$$

where $F_1(z)$ is a function analytical in D. Now we express the derivative $\frac{\partial}{\partial z}(u_1+iv_1)$ in terms of F_1 and obtain

$$u_1(x,y)+iv_1(x,y)=\frac{\lambda+3\mu}{4\mu(\lambda+2\mu)}\int F_1(z)dz-\frac{\lambda+\mu}{4\mu(\lambda+2\mu)}z\overline{F_1(z)}+\overline{G_1(z)},$$

where $G_1(z)$ is a function analytical in D. Finally we have this representation of the plane displacement vector u_1+iv_1, analogous to the plane displacement vector representation of [Muskhelishvili 1977]:

$$-2\mu(u_1(x,y)+iv_1(x,y))=-\kappa f_1(z)+z\overline{f_1'(z)}+\overline{g_1(z)},$$

where

$$\frac{\lambda+\mu}{2(\lambda+2\mu)}\int F_1(z)dz\equiv f_1(z),\quad -2\mu G_1(z)\equiv g_1(z),\quad \frac{\lambda+3\mu}{\lambda+\mu}\equiv\kappa.$$

The coefficient with h in (10) yields $\dfrac{\partial^2 w_1}{\partial x^2}+\dfrac{\partial^2 w_1}{\partial y^2}=0$. So $w_1=\operatorname{Re} q_1(z)$, where $q_1(z)$ is a function analytical in D.

We have to restore the analytical in D functions $f_1(z)$, $g_1(z)$ and $q_1(z)$ using the boundary conditions (5)–(7) on the interior boundary of D and using the given displacements $u_1(x_2(s),y_2(s))H=a$, $v_1(x_2(s),y_2(s))=0$, $w_1(x_2(s),y_2(s))=0$ at the exterior boundary of D.

So we have the following boundary conditions for the functions $f_1(z)$ and $g_1(z)$, which are analytical in D:

$$\left[f_1(z)+z\overline{f_1'(z)}+\overline{g_1(z)}\right]_{z=x_1(s)+iy_1(s)}=0,\quad \left[-\kappa f_1(z)+z\overline{f_1'(z)}+\overline{g_1(z)}\right]_{z=x_2(s)+iy_2(s)}=-2\mu\frac{a}{H},\quad (11)$$

The interior boundary condition in relation (11) is the boundary condition of the first boundary value problem of the plane elasticity theory, the exterior boundary condition is the boundary condition of the second boundary value problem of the plane elasticity theory [Muskhelishvili 1977].

We have the following boundary conditions for the function $q_1(z)$, analytical in D:

$$\frac{\partial}{\partial n}\left[\operatorname{Re} q_1(z)\right]_{z=x_1(s)+iy_1(s)}=0,\quad \left[\operatorname{Re} q_1(z)\right]_{z=x_2(s)+iy_2(s)}=0.\quad (12)$$

The interior boundary condition in (12) is the Neumann condition for a harmonic function which can

be rewritten as $\frac{\partial}{\partial s}[\operatorname{Im} q_1(z)]_{z=x_1(s)+iy_1(s)} = 0$; the exterior boundary condition is the Dirichlet boundary condition for a harmonic function.

Clearly this boundary value problem has the solution $f_1(z) \equiv \dfrac{2\mu a}{(1+\kappa)H}$, $g_1(z) \equiv -\dfrac{2\mu a}{(1+\kappa)H}$, $q_1(z) \equiv 0$, $z \in D$.

After restoring the components $u_1(x, y) \equiv a/H$, $v_1(x, y) \equiv 0$ and $w_1(x, y) \equiv 0$ we reconstruct the components $u_0(x, y)$, $v_0(x, y)$ and $w_0(x, y)$. To do this we apply the interior boundary conditions (2)–(4) and the exterior boundary conditions $u_0(x_2(s), y_2(s)) = 0$, $v_0(x_2(s), y_2(s)) = 0$, $w_0(x_2(s), y_2(s)) = 0$ and introduce functions $f_0(z)$, $g_0(z)$ and $q_0(z)$, analytical in D. We have for these functions the boundary relations

$$\begin{aligned} \left[f_0(z) + z\overline{f_0'(z)} + \overline{g_0(z)}\right]_{z=x_1(s)+iy_1(s)} &= 0, \qquad \frac{\partial}{\partial n}[\operatorname{Re} q_0(z)]_{z=x_1(s)+iy_1(s)} = -\frac{a}{H}, \\ \left[-\kappa f_0(z) + z\overline{f_0'(z)} + \overline{g_0(z)}\right]_{z=x_2(s)+iy_2(s)} &= 0, \qquad [\operatorname{Re} q_0(z)]_{z=x_2(s)+iy_2(s)} = 0. \end{aligned} \tag{13}$$

The boundary conditions in the left column of (13) yield $f_0(z) \equiv 0$, $g_0(z) \equiv 0$, so $u_0(x, y) \equiv 0$, $v_0(x, y) \equiv 0$, but the problem of the function $q_0(z)$ restoration via boundary conditions (14) is not so easy. Application of the additional mapping from an annulus to the domain D allows us to solve this boundary value problem. Let $z(\zeta)$ be the analytic function mapping the annulus $r < |\zeta| < 1$ onto D. Consider $\chi_0(\zeta) = q_0(z(\zeta))$. Now in order to restore the function $\chi_0(\zeta)$ in the annulus $r < |\zeta| < 1$ we have the boundary conditions

$$[\operatorname{Re}(\zeta \chi_0'(\zeta))]_{z=re^{i\theta}} = -\frac{a}{H}|z'(re^{i\theta})|, \quad \operatorname{Re}(\chi_0(e^{i\theta})) = 0.$$

This boundary value problem in the annulus is resolvable approximately through the relative series expansion and coefficient comparison.

We consider $z(\zeta) = z_o(\zeta)$ for the oval tube, $z(\zeta) = z_e(\zeta)$ for the elliptical tube, $r = r_o$ for the oval tube, $r = r_e$ for the elliptical tube and examine the resulting exterior boundary stresses for the oval and elliptical tubes.

We find the absolute value of the stress vector $\sqrt{\sigma_{n1}^2 + \sigma_{n2}^2}$ at the level $h = 0$ on the exterior surfaces for both tubes and for $\kappa = 2$. The formula expressing the stresses value dependence on the polar angle is $100a\, V_o(\theta)/H$ for the oval tube and $100a\, V_e(\theta)/H$ for the elliptical tube. The graphs of $V_o(\theta)$ and $V_e(\theta)$ are shown in Figure 3. The maximal absolute value of stress vector for the bent tube reaches maximum both at the bending points and at the points opposite to them, this maximal value for the elliptical tube is larger than that for the oval one but the difference is not essential.

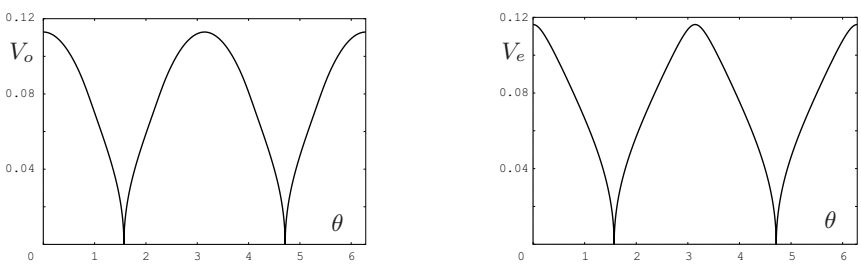

Figure 3. Stresses in the bent oval (left) and elliptical (right) tubes.

5. Conclusion

The conformal mapping method presented here is computationally efficient for twisted and bent tubes with noncircular cross-sections. It provides us with a Fourier polynomial mapping function. This approximate conformal mapping method makes it possible to apply the conformal mapping approach to many problems of elasticity.

References

[Abzalilov and Shirokova 2017] D. F. Abzalilov and E. A. Shirokova, "The approximate conformal mapping onto simply and doubly connected domains", *Complex Var. Elliptic Equ.* **62**:4 (2017), 554–565.

[Baroutaji et al. 2014] A. Baroutaji, E. Morris, and A. G. Olabi, "Quasi-static response and multi-objective crashworthiness optimization of oblong tube under lateral loading", *Thin-Walled Struct* **82** (2014), 262–277.

[Bazehhouri and Rezaeepazhand 2012] B. G. Bazehhouri and J. Rezaeepazhand, "Simplified approach for torsional analysis of non-homogenous tubes with noncircular cross-sections", *IJE Transactions A* **25**:3 (2012), 277–287.

[Ivanshin and Shirokova 2011] P. N. Ivanshin and E. A. Shirokova, *Spline-interpolation solution of one elasticity theory problem*, Bentham Science, 2011.

[Ivanshin and Shirokova 2016] P. N. Ivanshin and E. A. Shirokova, "Approximate conformal mappings and elasticity theory", *J. Complex Anal.* (2016), Art. ID 4367205, 8.

[Moore 1990] I. D. Moore, "Three-dimensional response of elastic tubes", *Int. J. Solids Struct.* **26**:4 (1990), 391–400.

[Muskhelishvili 1977] N. I. Muskhelishvili, *Some basic problems of the mathematical theory of elasticity*, Noordhoff International Publishing, Leiden, 1977.

[Nayak and Mondal 2011] P. Nayak and S. C. Mondal, "Analysis of a functionally graded thick cylindrical vessel with radially varying properties", *Int. J. Engng. Sci. Tech.* **3**:2 (2011), 1551–1562.

[Rizzetto et al. 2019] F. Rizzetto, E. Jansen, M. Strozzi, and F. Pellicano, "Nonlinear dynamic stability of cylindrical shells under pulsating axial loading via Finite Element analysis using numerical time integration", *Thin-Walled Struct.* **143** (2019), 106213.

[Shirokova 2004] E. A. Shirokova, "Elastic solutions for a pressurised tube with given exterior displacements", *Int. J. Press. Vessels Pip.* **81**:9 (2004), 731–738.

[Shirokova 2014] E. A. Shirokova, "On the approximate conformal mapping of the unit disk on a simply connected domain", *Russian Math.* (*Iz. VUZ*) **58**:3 (2014), 47–56.

[Yella Reddy and Reid 1979] T. Yella Reddy and S. R. Reid, "Lateral compression of tubes and tube-systems with side constraints", *Int. J. Mech. Sci.* **21**:3 (1979), 187–199.

[Zheng et al. 2015] M. Zheng, Y. Zhao, H. Teng, J. Hu, and L. Yu, "Elastic limit analysis for elliptical and circular tubes under lateral tension", *Arab. J. Sci. Eng.* **40**:6 (2015), 1727–1732.

Received 15 Mar 2018. Revised 18 Jul 2018. Accepted 24 Jul 2020.

DAMIR F. ABZALILOV: damir.abzalilov@kpfu.ru
N. I. Lobachevsky Institute of Mathematics and Mechanics, Kazan Federal University, Kazan, 420008, Russia

PYOTR N. IVANSHIN: pivanshi@yandex.ru
N. I. Lobachevsky Institute of Mathematics and Mechanics, Kazan Federal University, Kazan, 420008, Russia

ELENA A. SHIROKOVA: elena.shirokova@kpfu.ru
N. I. Lobachevsky Institute of Mathematics and Mechanics, Kazan Federal University, Kazan, 420008, Russia

JOURNAL OF MECHANICS OF MATERIALS AND STRUCTURES
Vol. 15, No. 5, 2020
https://doi.org/10.2140/jomms.2020.15.565

MAGNETORHEOLOGICAL ELASTOMER ISOLATOR IN COMPRESSION MODE FOR IMU VIBRATION ISOLATION

YANG FUFENG AND TAO YU

Magnetorheological elastomer (MRE) is a new class of smart materials, whose mechanical properties can be continuously and rapidly controlled by an applied magnetic field. A compression MRE isolator was designed and fabricated. The mechanical tests were conducted by instron. The dynamic properties of MRE isolator were studied by frequency sweeping tests, using vibration table under 1 g acceleration excitation with different currents. The peak value of the transmissibility was decreased by 29.7% and the natural frequency of the single degree of freedom (SDOF) system approximately increased by 18.54% while the current varied from 0.0 A to 4.0 A. Moreover, the equivalent stiffness and damping coefficients were identified from experimental data. In order to further evaluate the effectiveness of MRE isolator for vibration control, the SDOF inertial measurement unit (IMU) isolation system was simulated under random vibration conditions. The peak acceleration of power spectral density (PSD) was decreased by 48.8% when applying a series of constant currents. The study verifies that the compression MRE isolator is capable of increasing system stiffness, changing system natural frequency and decreasing system vibration.

1. Introduction

Vibration isolation is the most popular structures protection technique for many engineering structures. However, research has revealed that the traditional passive vibration isolation systems, due to the passive nature, are inable to adapt to changes in structural parameters over time, which results in reduced performance. Any changes of the mechanical system such as varying mass or uncertain external excitations and disturbances are not well supported by a passive isolation system. A great deal of efforts have been dedicated to improve the performance of the traditional passive vibration isolation system. A series of research efforts have been made for the development of novel adaptive vibration isolators utilizing magnetorheological elastomers (MREs) [Brancati et al. 2017; Tao et al. 2019; Yang et al. 2016]. MRE is a type of smart rubber, generally fabricated by dispersing magnetized particles in a solid polymer medium such as natural rubber and curing under an applied magnetic field, which causes the magnetic particles to align in chains. The elastic modulus or stiffness of MRE increases monotonically with the applied magnetic field. This unique and controllable stiffness property of MREs offers a great opportunity for the development of adaptive vibration isolators [Liao et al. 2012; Behrooz et al. 2014]. The tunable automotive mounts and bushings based on MRE were developed in [Ginder et al. 2000]. They found that the suspension resonances excited by torque variation could be suppressed by shifting the resonance away from the excitation frequency. Another similar adaptive tuned vibration buffer based on MRE was studied in [Deng et al. 2006]. MRE are currently being researched by many industries including the

Keywords: vibration isolation, magnetorheological elastomer, isolator, dynamics.

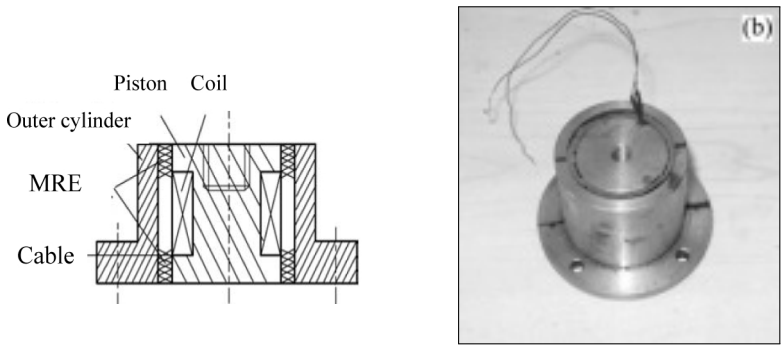

Figure 1. Schematic configuration and photograph of MRE with shear deformation [Dong et al. 2009].

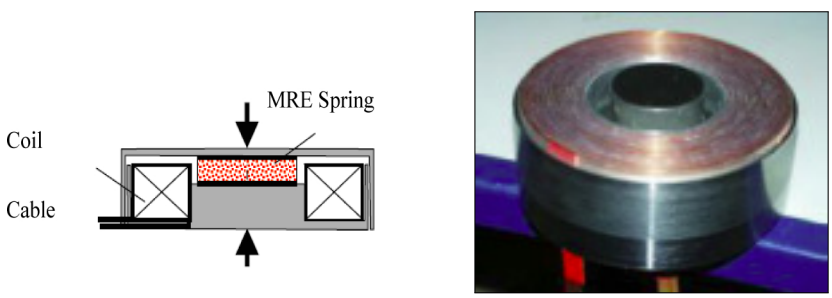

Figure 2. Schematic configuration and photograph of MRE with compression deformation [Kallio 2005].

automotive, building, and space industries. Such as, space applications include isolation of payloads from rocket stages during launch and isolation of mirrors in space telescopes.

There is a wide variety of non-magnetic matrices of MREs, like natural rubbers, silicone rubbers and polyurethanes with a varying filler volume fraction. MREs can be classified into two types: isotropic and anisotropic. Isotropic MRE is a homogeneous mixture of host matrix and magnetic particles. Anisotropic MRE is fabricated by aligning the magnetic particles into a chain-like structure when cured with an applied magnetic field. Under the influence of a magnetic field the MRE becomes stiffer due to decreased distance between the magnetic particles. The effect is usable for the applications of vibration isolation. The MRE magnetostrictive effect is the most important feature for the vibration control application. Shearing of the cured composite in the presence of a magnetic field causes MRE work dependent shear modulus. Aligned MREs are shown to have a field dependent shear modulus, but the other elastic properties are still quite unexplored, especially when the MREs are measured without the applied magnetic field. As shown in Figure 1, the shear deformation of MRE appears by the motion of the piston. The magnetic field exists in the MRE which is perpendicular to the motion of the piston after the current is applied to the coil [Dong et al. 2009].

As the same, aligned MREs are shown to have a field dependent compression modulus. As shown in Figure 2, the magnetic field in the MRE spring element is along the same direction as its cylinder axis (in the chain direction of aligned MREs) during the compression tests [Kallio 2005].

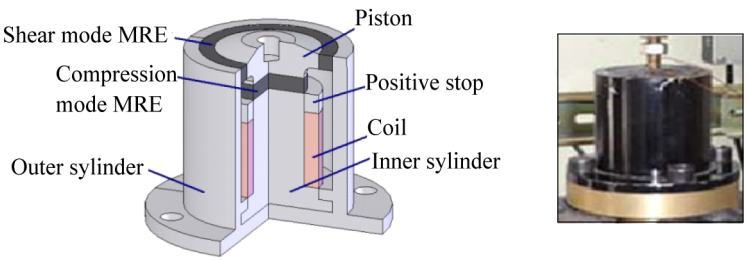

Figure 3. Magnetorheological elastomer isolator in shear-compression mixed mode [Liu 2012].

Figure 3 shows a magnetorheological elastomer isolator working in shear-compression mixed mode, which is composed of two pieces of MREs, one works in shear mode and another works in compression mode. Excitation magnetic field of the isolator is generated by the excitation coil, its direction is parallel with the pressure direction and vertical with shear direction. As the modulus of MRE in compression mode is higher than that in shear mode, the structure can effectively reduce the static strain caused by the quality of the isolation device [Liu 2012].

In this study, a novel MRE isolator working in compression mode is proposed. The design, fabrication and tests of compression MRE isolator are introduced. The experimental study on the mechanical properties of MRE isolator is performed by instron and vibrating table, respectively. Then the compression force and displacement test results are presented and discussed. The stiffness and damping ratio coefficients are identified from frequency sweeping test data. The SDOF IMU isolator system with four MRE isolators is developed and simulated under random excitation input. The simulation results of PSD and displacement are discussed and the performance of MRE isolator is evaluated. The compression MRE isolator proposed in this paper can meet the requirements of the working environment and installation space for the IMU. It has the characteristics of small volume, integrated preparation and controllable output force.

2. Fabrication of the compression MRE isolator

The schematic design of the compression MRE isolator is shown in Figure 4. As can be seen, the design consists of a cylindrical MRE, two electromagnetic coils, two iron core connectors and an outer magneto-conductivity casing. The structure of isolator allows the MRE to work in compression mode. The motion of payload can be controlled in both up and down directions. The magnetic field is generated by the coils and controlled by tuning the current. Moreover, the direction of magnetic field in the MRE is parallel to the motion of the iron cores after the current is applied to the coils. One end of each iron core is embedded inside the MRE. The diameter of the MRE is 35 mm, and the diameter of the coil wire is 0.50 mm with a total winding number of 300 turns. Each coil has electric resistance of 1.38 Ω.

Natural rubber is a flexible, rubbery polymer obtained from the tree Hevea Brasiliensis. Natural rubber is a popular choice for the preparation of MRE because of its advantageous mechanical characteristics. The particles used are BASF EW carbonyl iron powders and the mass fraction of iron particles is 60%. A compound of the uncured rubber is accomplished on a laboratory scale two-roll mill. After the rubber is well mixed, the iron particles are introduced into the rubber again on the two-roll mill. After the final compounding, the MREs are prepared in electromagnetic mold, as shown in Figure 5. The mold

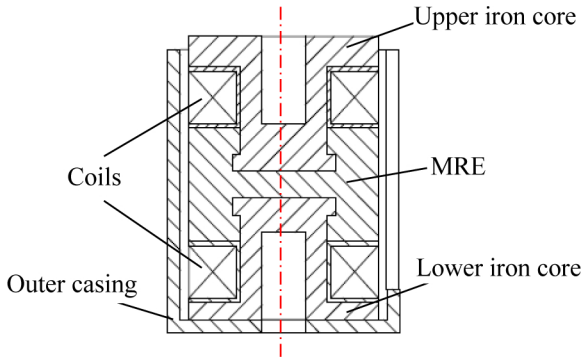

Figure 4. Schematic of the MRE isolator.

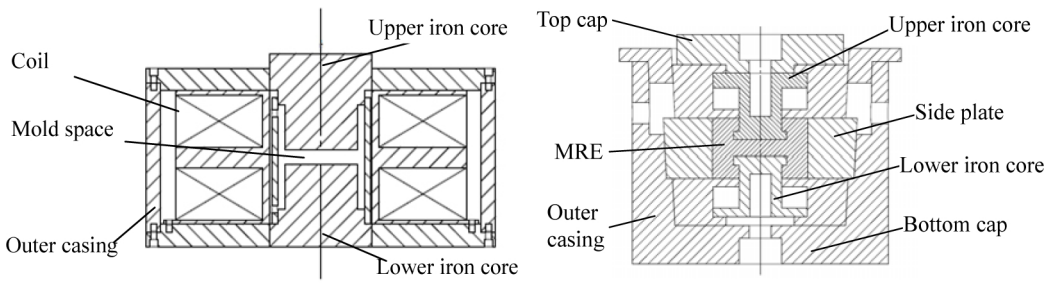

Figure 5. Schematic of the electromagnetic device (left) and the MRE mold (right).

Figure 6. Different assembly forms of MRE isolator: compound structure (left), compound structure with coils (middle), and complete structure (right).

is pre-heated in the vulcanizing machine, and the high pressure is applied to the polymer during the curing process. Current is applied to the electromagnet coils to produce the desired alignment magnetic field, with a magnetic induction of 1 Tesla. Natural rubber MREs are cured for 15 min before taken out. Figure 6 presents different assembly forms of MRE isolator. The compound structure is made up of MRE, magnetizers and coil skeletons.

3. Test and discussion

The quasi-static and dynamic tests are carried out to verify the performances of the MRE isolators and to obtain the relationship among stiffness, damping and current.

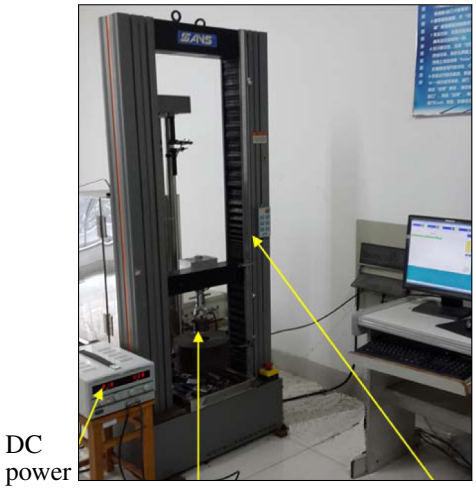

Figure 7. MRE experimental test setup.

3.1. ***Compression force and displacement test.*** The experimental study on the mechanical properties of the compound structure as shown in Figure 6(b) is performed. The purpose of the quasi-static tests is to evaluate and record the physical properties of MRE isolators under different magnetic fields and different displacement amplitudes. The experimental test setup is shown in Figure 7. MRE isolator is located in the electromagnetic device and connected to the instron (CMT-4254). DC power source provides current to the coils inside the electromagnetic device which generates the magnetic field surrounding the MRE isolators. And the magnetic field intensity is measured by magnetometer. Controlled compression displacement of the MRE isolator is supplied by the instron. The experiments are conducted with room temperature 25 °C and the loading rate 1 mm/Min. The compression force and displacement curves of the MRE are shown in Figure 8. It can be seen that the force of the MRE isolator increases as the increasement of applied magnetic field and displacement, respectively. The displacement is almost 0 mm when the static force of MRE isolator is about 20 N. It means that the static stiffness of MRE isolator is enough to support IMU and meet the installation conditions.

3.2. ***Frequency sweeping test.*** The MRE isolator is evaluated by the frequency sweeping test. It is carried out by a vibration table with 1g acceleration and different currents. The experimental setup of frequency sweeping test with MRE isolator is shown in Figure 9. The SDOF vibration system is composed of a payload and a MRE isolator. The payload of the SDOF system is supported by MRE isolator, which is mounted on the vibration table. The payload acceleration and vibration table input acceleration are measured by two accelerometers (PCB Model 352C33) respectively. DC power source provides current to the coils inside MRE isolator which generates the magnetic field surrounding the MRE. The parameters of the frequency sweeping test are as follows:

Sweep frequency: 20 Hz to 200 Hz Payload: 2.0 kg Acceleration: 1 g Current: 0, 1, 2, 3, 4 A

Figure 10 Experimental results with different currents shows the acceleration transmissibility results for a frequency range between 20–100 Hz and the acceleration amplitude of 1 g with different currents

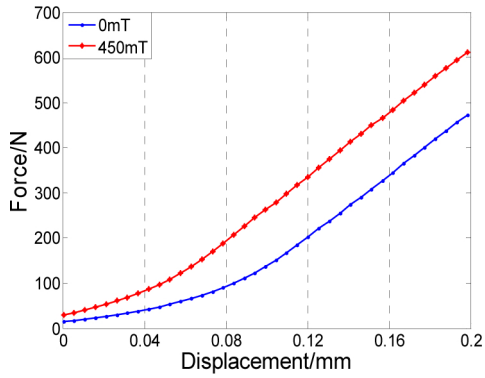

Figure 8. Compression force and displacement curves.

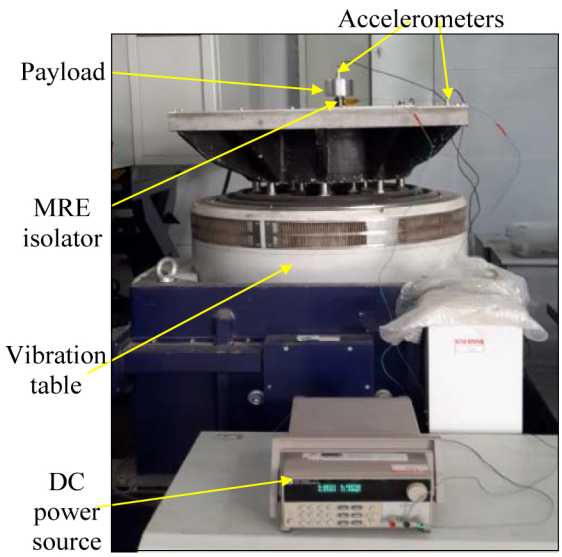

Figure 9. Experimental setup of frequency sweeping test with MRE isolator.

applied to the MRE isolator. As can been seen, the natural frequency of the SDOF system increases from 42.23 Hz at 0 A to 50.06 Hz at 4 A. The peak value of the transmissibility is reduced from 5.403 to 3.796. The natural frequency of the SDOF system approximate increase equals to 19.8%. The peak value has the total reduction of 29.7% in the acceleration transmissibility approximately.

3.3. ***The identification of stiffness and damping ratio coefficients.*** The stiffness and damping ratio coefficients are identified by using the experimental results of acceleration transmissibility as shown in Figure 10. The steps are listed as follows:

1) The peak value of the acceleration transmissibility is H_m, and it represents the value of half power point H_p. The relationship between them can be written as

$$H_p = \frac{H_m}{\sqrt{2}} \approx 0.707 H_m. \tag{1}$$

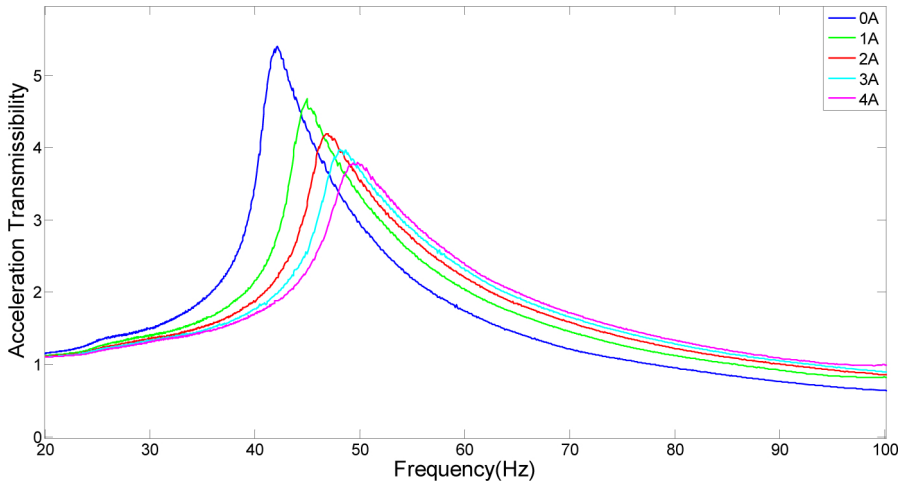

Figure 10. Experimental results with different currents.

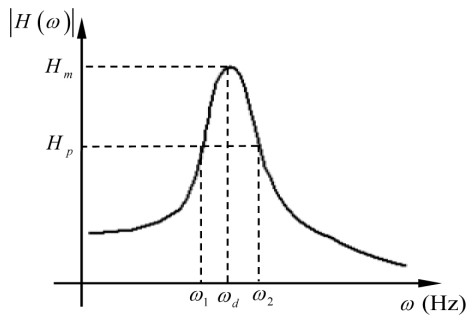

Figure 11. Relation of half power points and frequency.

The frequencies ω_1 and ω_2 correspond to half power points of the acceleration transmissibility are shown in Figure 12, right. The coefficient is given by the equation

$$n = \frac{\omega_2 - \omega_1}{2}. \tag{2}$$

2) The resonance frequency ω_d can be obtained through the frequency response curve, and the natural frequency is given by

$$\omega_n = \sqrt{{\omega_d}^2 + n^2}. \tag{3}$$

The damping ratio is defined as

$$\zeta = n/\omega_n. \tag{4}$$

3) The stiffness of MRE isolator is calculated through the equation

$$k = 4\pi^2 {\omega_n}^2 m, \tag{5}$$

where m is the payload mass.

Table 1 lists the normalized equivalent stiffness and damping coefficients from experimental data. The maximum value of effective stiffness is 197.9 kN/m and the maximum increase of the effective stiffness

current	natural frequency	stiffness	damping ratio
0 A	42.23 Hz	140.8 kN/m	0.071
1 A	45.08 Hz	160.5 kN/m	0.080
2 A	47.03 Hz	174.6 kN/m	0.094
3 A	48.40 Hz	184.9 kN/m	0.103
4 A	50.06 Hz	197.9 kN/m	0.110

Table 1. Equivalent stiffness and damping coefficients of MRE isolator.

is 40.55% as current varies from 0.0 A to 4.0 A. The maximum increase of damping ratio is 54.9%. The test results reveal that as the applied magnetic field increases, the natural frequency, stiffness and damping ratio of the MRE isolator increase in value. The relationships of frequency (Hz), stiffness (kN/m), damping ratio and current (A), obtained by polynomial fitting, are as follows:

$$f(I) = 0.0229I^4 - 0.0842I^3 - 0.3579I^2 + 3.2692I + 42.23, \tag{6}$$

$$K(I) = 0.1958I^4 - 0.875\ \ I^3 - 1.5458I^2 + 21.925I + 140.8, \tag{7}$$

$$\zeta(I) = 0.0005I^4 - 0.0049I^3 + 0.0135I^2 - 0.0001I + 0.071. \tag{8}$$

4. Theoretical model and calculation method

The IMU usually works in the random vibration environment. The control relationships of the single MRE isolators are substituted into the dynamics simulation of IMU isolation system. Then the IMU output power spectrum under the typical random vibration environment is obtained. Thus, the aim of predicting the isolation effect of MRE isolators for IMU is achieved.

4.1. ***Dynamics model of IMU system.*** The dynamics model of IMU system is established as shown in Figure 12, left. According to the dynamics properties of IMU system, it is considered as a multibody system comprising rigid bodies, springs and dampers. The motion of the carrier 0 is the input of the IMU system. Platform 5 and three gyros 9∼11 are considered as rigid bodies, respectively; platform and carrier are linked by MRE isolators 1∼4, which are regarded as controlled spring-and-damper hinges longitudinally vibrating in space. The connections 6∼8 between platform and gyros are considered as spatial spring-and-damper hinges.

Isolators 1∼4 can be treated as one equivalent hinge element, which will be shown in the following, thus the dynamics model of IMU system can be dealt with a tree system. Its topology figure can be got easily as shown in Figure 12, right. In the topology figure, the circles represent body elements wherein the numbers indicate the corresponding body element number; the arrows denote hinge elements and the transfer directions of state vectors, the numbers aside are the sequence numbers of the hinge elements. The boundaries are all numbered as 0. The boundaries corresponding to elements 1∼4 are considered as output boundaries, and the boundaries corresponding to elements 9∼11 are considered as input boundaries. So the IMU isolation system is considered as a multibody system composed of 4 rigid bodies and 3 hinges.

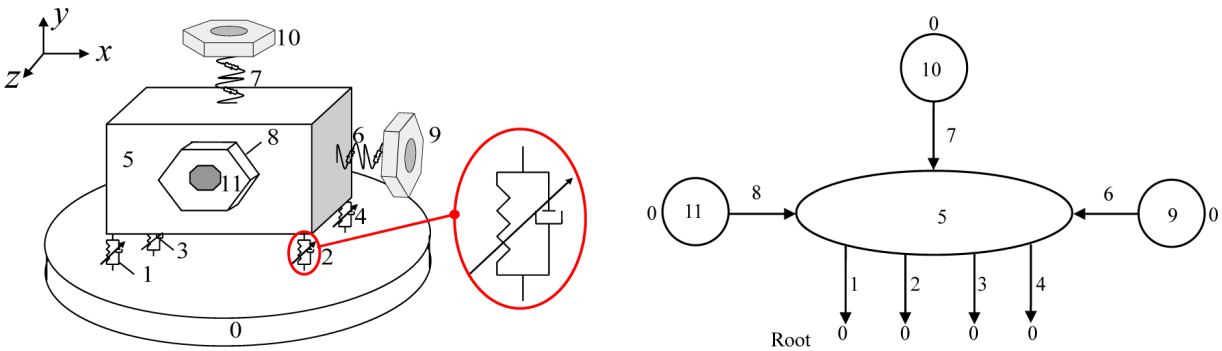

Figure 12. Left: dynamics model of laser IMU isolation system. Right: Topology of laser gyro SIMU system.

The state vectors of the input and output points of every element and the boundary points are defined as

$$\boldsymbol{Z} = \begin{bmatrix} X & Y & Z & \Theta_x & \Theta_y & \Theta_z & M_x & M_y & M_z & Q_x & Q_y & Q_z \end{bmatrix}^{\mathrm{T}} \tag{9}$$

The state variables in the state vector are the linear displacements, angular displacements, internal forces and internal torques in the modal coordinates. The specific derivation of the transfer matrix of one degree of freedom system can refer to reference [Chen et al. 2013].

4.2. *Transfer equation and transfer matrix of system components.*

Transfer equation and transfer matrix of elements 1∼4. Each MRE isolator is regarded as a spatial stiffness-and-damper hinge, which contains stiffness along the X, Y and Z directions. As four isolators are sandwiched between two rigid bodies, they can be treated as one new element, namely, an equivalent spring-and-damper hinge with single input end and single output end. The principal vectors and principal moments of the element at the output end and the input end are the same. We obtain

$$\begin{bmatrix} M_x \\ M_y \\ M_z \\ Q_x \\ Q_y \\ Q_z \end{bmatrix}_{\mathrm{O}} = \begin{bmatrix} M_x \\ M_y \\ M_z \\ Q_x \\ Q_y \\ Q_z \end{bmatrix}_{\mathrm{I}} = \boldsymbol{K}_{1-4} \begin{bmatrix} X \\ Y \\ Z \\ \Theta_x \\ \Theta_y \\ \Theta_z \end{bmatrix}_{\mathrm{O}} - \boldsymbol{K}_{1-4} \begin{bmatrix} X \\ Y \\ Z \\ \Theta_x \\ \Theta_y \\ \Theta_z \end{bmatrix}_{\mathrm{I}}, \qquad \begin{bmatrix} X \\ Y \\ Z \\ \Theta_x \\ \Theta_y \\ \Theta_z \end{bmatrix}_{\mathrm{O}} = \begin{bmatrix} X \\ Y \\ Z \\ \Theta_x \\ \Theta_y \\ \Theta_z \end{bmatrix}_{\mathrm{I}} + \boldsymbol{K}_{1-4}^{-1} \begin{bmatrix} M_x \\ M_y \\ M_z \\ Q_x \\ Q_y \\ Q_z \end{bmatrix}_{\mathrm{I}}. \tag{10}$$

The transfer equation of elements 1∼4 is

$$\boldsymbol{Z}_{1\sim4,\mathrm{O}} = \boldsymbol{U}_{1\sim4} \boldsymbol{Z}_{1\sim4,\mathrm{I}}. \tag{11}$$

The transfer matrix is

$$\boldsymbol{U}_{1\sim4} = \begin{bmatrix} \boldsymbol{I}_6 & \boldsymbol{K}_{1\sim4}^{-1} \\ \boldsymbol{O}_{6\times6} & \boldsymbol{I}_6 \end{bmatrix}, \tag{12}$$

where

$$\boldsymbol{K}_{1\sim4}=\begin{bmatrix} 0 & -\sum_{i=1}^{4}k_{yi}c_i & \sum_{i=1}^{4}k_{zi}b_i & \sum_{i=1}^{4}(k_{yi}c_i^2+k_{zi}b_i^2) & -\sum_{i=1}^{4}k_{zi}a_ib_i & -\sum_{i=1}^{4}k_{yi}a_ic_i \\ \sum_{i=1}^{4}k_{xi}c_i & 0 & -\sum_{i=1}^{4}k_{zi}a_i & -\sum_{i=1}^{4}k_{zi}b_ia_i & \sum_{i=1}^{4}(k_{xi}c_i^2+k_{zi}a_i^2) & -\sum_{i=1}^{4}k_{xi}b_ic_i \\ -\sum_{i=1}^{4}k_{xi}b_i & \sum_{i=1}^{4}k_{yi}a_i & 0 & -\sum_{i=1}^{4}k_{yi}c_ia_i & -\sum_{i=1}^{4}k_{xi}c_ib_i & \sum_{i=1}^{4}(k_{xi}b_i^2+k_{yi}a_i^2) \\ -\sum_{i=1}^{4}k_{xi} & 0 & 0 & 0 & -\sum_{i=1}^{4}k_{xi}c_{\mathrm{i}} & \sum_{i=1}^{4}k_{xi}b_{\mathrm{i}} \\ 0 & -\sum_{i=1}^{4}k_{yi} & 0 & \sum_{i=1}^{4}k_{yi}c_{\mathrm{i}} & 0 & -\sum_{i=1}^{4}k_{yi}a_{\mathrm{i}} \\ 0 & 0 & -\sum_{i=1}^{4}k_{zi} & -\sum_{i=1}^{4}k_{zi}b_{\mathrm{i}} & \sum_{i=1}^{4}k_{zi}a_{\mathrm{i}} & 0 \end{bmatrix}$$

Here (a_i, b_i, c_i) $(i = 1\sim4)$ denote the positions of isolators 1∼4 on the carrier and platform, and (k_{xi}, k_{yi}, k_{zi}) are the initial stiffness coefficients of the isolators.

The transfer equation and transfer matrix of element 5. Platform 5 is considered as a rigid body with three input ends and single output end, and its transfer equation is

$$\begin{cases} \boldsymbol{Z}_{5,\mathrm{O}}=\boldsymbol{U}_5\boldsymbol{Z}_{5,\mathrm{I}_1}+\boldsymbol{U}_{5,\mathrm{I}_2}\boldsymbol{Z}_{5,\mathrm{I}_2}+\boldsymbol{U}_{5,\mathrm{I}_3}\boldsymbol{Z}_{5,\mathrm{I}_3}, \\ \boldsymbol{H}_5\boldsymbol{Z}_{5,\mathrm{I}_1}=\boldsymbol{H}_{5,\mathrm{I}_2}\boldsymbol{Z}_{5,\mathrm{I}_2}, \\ \boldsymbol{H}_5\boldsymbol{Z}_{5,\mathrm{I}_1}=\boldsymbol{H}_{5,\mathrm{I}_3}\boldsymbol{Z}_{5,\mathrm{I}_3}. \end{cases} \tag{13}$$

The transfer matrix is given by

$$\boldsymbol{U}_5=\begin{bmatrix} \boldsymbol{I}_3 & -\tilde{\boldsymbol{l}}_{\mathrm{I}_1\mathrm{O}} & \boldsymbol{O}_{3\times3} & \boldsymbol{O}_{3\times3} \\ \boldsymbol{O}_{3\times3} & I_3 & \boldsymbol{O}_{3\times3} & \boldsymbol{O}_{3\times3} \\ m\Omega^2\tilde{\boldsymbol{l}}_{\mathrm{CO}} & -\omega^2(m\tilde{\boldsymbol{l}}_{\mathrm{I}_1\mathrm{O}}\tilde{\boldsymbol{l}}_{\mathrm{I}_1\mathrm{C}}+\boldsymbol{J}_{\mathrm{I}_1}) & \boldsymbol{I}_3 & \tilde{\boldsymbol{l}}_{\mathrm{I}_1\mathrm{O}} \\ m\Omega^2\boldsymbol{I}_3 & -m\Omega^2\tilde{\boldsymbol{l}}_{\mathrm{I}_1\mathrm{C}} & \boldsymbol{O}_{3\times3} & \boldsymbol{I}_3 \end{bmatrix}, \tag{14}$$

$$\boldsymbol{U}_{5,\mathrm{I}_r}=\begin{bmatrix} \boldsymbol{O}_{3\times3} & \boldsymbol{O}_{3\times3} & \boldsymbol{O}_{3\times3} & \boldsymbol{O}_{3\times3} \\ \boldsymbol{O}_{3\times3} & \boldsymbol{O}_{3\times3} & \boldsymbol{O}_{3\times3} & \boldsymbol{O}_{3\times3} \\ \boldsymbol{O}_{3\times3} & \boldsymbol{O}_{3\times3} & \boldsymbol{I}_3 & \tilde{\boldsymbol{l}}_{\mathrm{I}_r\mathrm{O}} \\ \boldsymbol{O}_{3\times3} & \boldsymbol{O}_{3\times3} & \boldsymbol{O}_{3\times3} & \boldsymbol{I}_3 \end{bmatrix} \quad (r=2,3), \tag{15}$$

$$\boldsymbol{H}_5=\begin{bmatrix} \boldsymbol{I}_3 & \boldsymbol{O}_{3\times3} & \boldsymbol{O}_{3\times3} & \boldsymbol{O}_{3\times3} \\ \boldsymbol{O}_{3\times3} & \boldsymbol{I}_3 & \boldsymbol{O}_{3\times3} & \boldsymbol{O}_{3\times3} \end{bmatrix}, \tag{16}$$

$$\boldsymbol{H}_{5,\mathrm{I}_\mathrm{r}}=\begin{bmatrix} \boldsymbol{I}_3 & \tilde{\boldsymbol{l}}_{\mathrm{I}_1\mathrm{I}_\mathrm{r}} & \boldsymbol{O}_{3\times3} & \boldsymbol{O}_{3\times3} \\ \boldsymbol{O}_{3\times3} & \boldsymbol{I}_3 & \boldsymbol{O}_{3\times3} & \boldsymbol{O}_{3\times3} \end{bmatrix} \quad (r=2,3) \tag{17}$$

where ω is the natural frequency of the IMU system, C denotes the center of mass, m is the mass of rigid body, $\boldsymbol{J}_{\mathrm{I}}$ is moment of inertia matrix relative to the input point I_1, and $\tilde{\boldsymbol{l}}_{\mathrm{I,O}}$ are the cross product matrices from point I to point O.

Transfer equation and transfer matrix of elements 8. The transfer equation of elements 6∼8 are

$$\boldsymbol{Z}_{i,\mathrm{O}} = \boldsymbol{U}_i \boldsymbol{Z}_{i,\mathrm{I}} \ (i = 6, 7, 8). \tag{18}$$

The transfer matrices are

$$\boldsymbol{U}_i = \begin{bmatrix} \boldsymbol{I}_3 & \boldsymbol{O}_{3\times3} & \boldsymbol{O}_{3\times3} & \boldsymbol{U}_{14} \\ \boldsymbol{O}_{3\times3} & \boldsymbol{I}_3 & \boldsymbol{U}_{23} & \boldsymbol{O}_{3\times3} \\ \boldsymbol{O}_{3\times3} & \boldsymbol{O}_{3\times3} & \boldsymbol{I}_3 & \boldsymbol{O}_{3\times3} \\ \boldsymbol{O}_{3\times3} & \boldsymbol{O}_{3\times3} & \boldsymbol{O}_{3\times3} & \boldsymbol{I}_3 \end{bmatrix} \ (i = 6, 7, 8), \tag{19}$$

where

$$\boldsymbol{U}_{14} = \begin{bmatrix} -1/k_x & 0 & 0 \\ 0 & -1/k_y & 0 \\ 0 & 0 & -1/k_z \end{bmatrix}, \qquad \boldsymbol{U}_{23} = \begin{bmatrix} 1/k'_x & 0 & 0 \\ 0 & 1/k'_y & 0 \\ 0 & 0 & 1/k'_z \end{bmatrix}.$$

Here k_x, k_y and k_z represent the stiffness coefficients of linear spring. k'_x, k'_y and k'_z denote the stiffness coefficients of rotary spring respectively.

Transfer equation and transfer matrix of elements 9∼11. The gyros 9∼11 are rigid bodies with single input and single output; their transfer equations are

$$\boldsymbol{Z}_{i,\mathrm{O}} = \boldsymbol{U}_i \boldsymbol{Z}_{i,\mathrm{I}} \ (i = 9, 10, 11). \tag{20}$$

The transfer matrices are

$$\boldsymbol{U}_i = \begin{bmatrix} \boldsymbol{I}_3 & -\tilde{\boldsymbol{l}}_{\mathrm{IO}} & \boldsymbol{O}_{3\times3} & \boldsymbol{O}_{3\times3} \\ \boldsymbol{O}_{3\times3} & \boldsymbol{I}_3 & \boldsymbol{O}_{3\times3} & \boldsymbol{O}_{3\times3} \\ m\Omega^2\tilde{\boldsymbol{l}}_{\mathrm{CO}} & -\omega^2(m\tilde{\boldsymbol{l}}_{\mathrm{IO}}\tilde{\boldsymbol{l}}_{\mathrm{IC}} + \boldsymbol{J}_I) & \boldsymbol{I}_3 & \tilde{\boldsymbol{l}}_{\mathrm{IO}} \\ m\Omega^2\boldsymbol{I}_3 & -m\Omega^2\tilde{\boldsymbol{l}}_{\mathrm{IC}} & \boldsymbol{O}_{3\times3} & \boldsymbol{I}_3 \end{bmatrix} \ (i = 9, 10, 11). \tag{21}$$

4.3. ***Overall transfer equation and overall transfer matrix of IMU system.*** According to the automatic deduction theorem of overall transfer equation of multibody system [Yang et al. 2014], the overall transfer equation can be obtained as follows:

$$\boldsymbol{U}_{\mathrm{all}} \boldsymbol{Z}_{\mathrm{all}} = \boldsymbol{0} \tag{22}$$

The overall transfer matrix is

$$\boldsymbol{U}_{\mathrm{all}} = \begin{bmatrix} -\boldsymbol{I}_{12} & \boldsymbol{T}_{9-1\sim4} & \boldsymbol{T}_{10-1\sim4} & \boldsymbol{T}_{11-1\sim4} \\ \boldsymbol{O}_{6\times12} & \boldsymbol{G}_{9-5} & \boldsymbol{G}_{10-5} & \boldsymbol{O}_{6\times12} \\ \boldsymbol{O}_{6\times12} & \boldsymbol{G}_{9-5} & \boldsymbol{O}_{6\times12} & \boldsymbol{G}_{11-5} \end{bmatrix}, \tag{23}$$

where

$$\begin{aligned} \boldsymbol{T}_{9-1\sim4} &= \boldsymbol{U}_{1\sim4}\boldsymbol{U}_5\boldsymbol{U}_6\boldsymbol{U}_9, & \boldsymbol{G}_{9-5} &= -\boldsymbol{H}_5\boldsymbol{U}_6\boldsymbol{U}_9, \\ \boldsymbol{T}_{10-1\sim4} &= \boldsymbol{U}_{1\sim4}\boldsymbol{U}_{5,7}\boldsymbol{U}_7\boldsymbol{U}_{10},, & \boldsymbol{G}_{10-5} &= \boldsymbol{H}_{5,7}\boldsymbol{U}_7\boldsymbol{U}_{10}, \\ \boldsymbol{T}_{11-1\sim4} &= \boldsymbol{U}_{1\sim4}\boldsymbol{U}_{5,8}\boldsymbol{U}_8\boldsymbol{U}_{11}, & \boldsymbol{G}_{11-5} &= \boldsymbol{H}_{5,8}\boldsymbol{U}_8\boldsymbol{U}_{11}. \end{aligned}$$

$\boldsymbol{Z}_{all}$ is a column matrix consisting of the state vectors of system boundary points:

$$\boldsymbol{Z}_{all} = [\boldsymbol{Z}^{\mathrm{T}}_{1\sim4,0} \quad \boldsymbol{Z}^{\mathrm{T}}_{9,0} \quad \boldsymbol{Z}^{\mathrm{T}}_{10,0} \quad \boldsymbol{Z}^{\mathrm{T}}_{11,0}]^{\mathrm{T}}. \tag{24}$$

The boundary conditions of the system are

$$\begin{aligned}
\boldsymbol{Z}_{1\sim4,0} &= [0 \quad 0 \quad 0 \quad 0 \quad 0 \quad 0 \quad M_x \quad M_y \quad M_z \quad Q_x \quad Q_y \quad Q_z]^{\mathrm{T}}_{1\sim4,0}, \\
\boldsymbol{Z}_{9,0} &= [X \quad Y \quad Z \quad \Theta_x \quad \Theta_y \quad \Theta_z \quad 0 \quad 0 \quad 0 \quad 0 \quad 0 \quad 0]^{\mathrm{T}}_{9,0}, \\
\boldsymbol{Z}_{10,0} &= [X \quad Y \quad Z \quad \Theta_x \quad \Theta_y \quad \Theta_z \quad 0 \quad 0 \quad 0 \quad 0 \quad 0 \quad 0]^{\mathrm{T}}_{10,0}, \\
\boldsymbol{Z}_{11,0} &= [X \quad Y \quad Z \quad \Theta_x \quad \Theta_y \quad \Theta_z \quad 0 \quad 0 \quad 0 \quad 0 \quad 0 \quad 0]^{\mathrm{T}}_{11,0}.
\end{aligned} \tag{25}$$

Substituting the boundary conditions into (11) yields

$$\bar{\boldsymbol{U}}_{all}\bar{\boldsymbol{Z}}_{\mathrm{all}} = \boldsymbol{0}, \tag{26}$$

where $\bar{\boldsymbol{U}}_{\mathrm{all}}$ is a 24×24 square matrix composed of the 1st∼6th, 19th∼30th and 37th∼42nd columns of $\boldsymbol{U}_{\mathrm{all}}$, $\bar{\boldsymbol{Z}}_{\mathrm{all}}$ is a column matrix consisting of the unknown elements in $\boldsymbol{Z}_{\mathrm{all}}$. For (20) to have nontrivial solutions, the determinant of its coefficient matrix must be zero, namely

$$\det(\bar{\boldsymbol{U}}_{\mathrm{all}}) = 0. \tag{27}$$

The eigenfrequencies ω_k $(k = 1, 2, 3, \ldots)$ of the IMU system can be obtained by solving (22). For each ω_k, using (20) and the transfer equations of elements, the state vector of any point can be got easily.

The body dynamics equations of IMU system can be written as

$$\boldsymbol{M}_j\boldsymbol{v}_{j,tt} + \boldsymbol{C}_j\boldsymbol{v}_{j,t} + \boldsymbol{K}_j\boldsymbol{v}_j = \boldsymbol{f}_j, \tag{28}$$

where j is the number of body element, the mass matrix $\boldsymbol{M}_j$ denotes the mass distribution of body element, displacement array $\boldsymbol{v}_j$ represents the motion state, consisting of the displacement and angular displacement variables of the body component and subscript t represents the time derivative time. The product of $\boldsymbol{K}_j$ and $\boldsymbol{v}_j$ represents all internal forces on the component and their action positions other than the damper force; $\boldsymbol{K}_j$ is called the stiffness parameter matrix; $\boldsymbol{C}_j$ acting on $\boldsymbol{v}_{j,t}$ represents the damping force on the body element and its action position, which is called a damping parameter matrix; $\boldsymbol{f}_j$ is the external force and torque of the body element. $\boldsymbol{f} = [\boldsymbol{f}_5^{\mathrm{T}} \quad \boldsymbol{f}_9^{\mathrm{T}} \quad \boldsymbol{f}_{10}^{\mathrm{T}} \quad \boldsymbol{f}_{11}^{\mathrm{T}}]^{\mathrm{T}}$; and $\boldsymbol{f}_j = [m_x, m_y, m_z, f_x, f_y, f_z]_j^{\mathrm{T}}$ is the column matrix of force (including torque) acted on the body j $(j = 5,\ 9,\ 10,\ 11)$.

4.4. ***Power spectrum analysis method.*** Using the modal superposition technology, the physical coordinates can be expanded in the form of augmented eigenvectors and generalized coordinates, i.e.,

$$\boldsymbol{v}_j = \sum_{k=1}^{n} \boldsymbol{V}_j^k q^k(t). \tag{29}$$

Substitute (29) into (28), make the inner product of $\boldsymbol{V}_j^k$ and sum up with j, then according to the orthogonality of the augmented eigenvector, it can be written as

$$\ddot{q}^k(t) + \frac{\sum\limits_j \left\langle \sum\limits_{k=1}^{n} (\boldsymbol{C}_j\boldsymbol{V}_j^k)\dot{q}^k(t), \boldsymbol{V}_j^k \right\rangle}{d^k} + \boldsymbol{\omega}_k^2 q^k(t) = \frac{\sum\limits_j \langle \boldsymbol{f}_j, \boldsymbol{V}_j^k \rangle}{d^k} \tag{30}$$

where

$$d^k = \sum_j \langle \boldsymbol{M}_j \boldsymbol{V}_j^k, \boldsymbol{V}_j^k \rangle = \langle \boldsymbol{M}_1 \boldsymbol{V}_1^k, \boldsymbol{V}_1^k \rangle + \langle \boldsymbol{M}_3 \boldsymbol{V}_3^k, \boldsymbol{V}_3^k \rangle + \cdots\cdots + \langle \boldsymbol{M}_{20} \boldsymbol{V}_{20}^k, \boldsymbol{V}_{20}^k \rangle,$$

$$\sum_j \langle \boldsymbol{f}_j, \boldsymbol{V}_j^k \rangle = \langle \boldsymbol{f}_1, \boldsymbol{V}_1^k \rangle + \langle \boldsymbol{f}_3, \boldsymbol{V}_3^k \rangle + \cdots\cdots + \langle \boldsymbol{f}_{20}, \boldsymbol{V}_{20}^k \rangle.$$

Then let

$$\frac{\sum_j \left\langle \sum_{k=1}^n (\boldsymbol{C}_j \boldsymbol{V}_j^k) \dot{q}^k(t), \boldsymbol{V}_j^k \right\rangle}{d^k} = 2\zeta_k \omega_k. \tag{31}$$

Substituting (29) and (31) into (30), one obtains

$$\ddot{q}^k(t) + 2\zeta_k \omega_k \dot{q}^k(t) + {\omega_k}^2 q^k(t) = \omega_k^2 p^k(t), \tag{32}$$

where

$$p^k(t) = \frac{\sum_j \langle \boldsymbol{f}_j, \boldsymbol{V}_j^k \rangle}{\omega_k^2 d^k} = \frac{\boldsymbol{V}^{k\mathrm{T}} \boldsymbol{f}(t)}{\omega_k^2 d^k}. \tag{33}$$

Then $q^1, \ldots, q^n$ are calculated by means of numerical integration. The dynamic response of the isolation system can be obtained by substituting them into (29). If each component of $\boldsymbol{f}(t)$ is a steady-state stochastic process, then the components of $\boldsymbol{v}_j(t)$, $p^k(t)$, $q^k(t)$ are all steady-state stochastic processes. The correlation matrix of response $\boldsymbol{v}_j$ and generalized coordinates $\boldsymbol{q}^k$ are defined as

$$\boldsymbol{R}_{v_j}(\tau) = \lim_{T\to\infty} \frac{1}{T} \int_{-T/2}^{T/2} \boldsymbol{v}_j(t) \boldsymbol{v}_j(t+\tau)^{\mathrm{T}} dt \tag{34}$$

$$R_{q^k}(\tau) = \lim_{T\to\infty} \frac{1}{T} \int_{-T/2}^{T/2} q^k(t) q^k(t+\tau)^{\mathrm{T}} dt, \tag{35}$$

$$\boldsymbol{R}_q(\tau) = \lim_{T\to\infty} \frac{1}{T} \int_{-T/2}^{T/2} \boldsymbol{q}(t) \boldsymbol{q}(t+\tau)^{\mathrm{T}} dt = \begin{bmatrix} R_{q^1} & \cdots & R_{q^1 q^k} & \cdots & R_{q^1 q^n}, \\ \vdots & \ddots & & & \\ R_{q^k q^1} & & R_{q^k} & & R_{q^k q^n} \\ \vdots & & & \ddots & \\ R_{q^n q^1} & \cdots & R_{q^n q^k} & \cdots & R_{q^n} \end{bmatrix}. \tag{36}$$

According to (36), this yields

$$\boldsymbol{R}_{v_j}(\tau) = \boldsymbol{V}_j \boldsymbol{R}_q(\tau) \boldsymbol{V}_j{}^{\mathrm{T}}. \tag{37}$$

The correlation matrices of generalized force p and external force f are

$$R_{p^k}(\tau) = \lim_{T\to\infty} \frac{1}{T} \int_{-T/2}^{T/2} p^k(t) p^k(t+\tau)^{\mathrm{T}} dt, \qquad \boldsymbol{R}_f(\tau) = \lim_{T\to\infty} \frac{1}{T} \int_{-T/2}^{T/2} \boldsymbol{f}(t) \boldsymbol{f}(t+\tau)^{\mathrm{T}} dt, \tag{38}$$

Then one gets

$$R_{p^k}(\tau) = \frac{\boldsymbol{V}^{k\mathrm{T}} \boldsymbol{R}_f(\tau) \boldsymbol{V}^k}{\omega_k^4 d^{k2}}, \quad k = 1, \ldots, n, \qquad R_{p^r p^s}(\tau) = \frac{\boldsymbol{V}^{r\mathrm{T}} \boldsymbol{R}_f(\tau) \boldsymbol{V}^s}{\omega_r^2 \omega_s^2 d^r d^s}, \quad r, s = 1, \ldots, n,\ r \neq s. \tag{39}$$

The power spectral matrix is deduced by Fourier transformation of the correlation matrix of the response in physical coordinates

$$\boldsymbol{S}_{v_j}(\omega) = \int_{-\infty}^{+\infty} \boldsymbol{R}_{v_j}(\tau) e^{-i\omega\tau} d\tau \tag{40}$$

The transformation relationships between $\boldsymbol{S}_{v_j}(\omega)$ and $\boldsymbol{S}_q(\omega)$, $S_{p^k}(\omega)$ and $\boldsymbol{S}_f(\omega)$ can be obtained as

$$\boldsymbol{S}_{v_j}(\omega) = \boldsymbol{V}_j \boldsymbol{S}_{\boldsymbol{q}}(\omega) \boldsymbol{V}_j{}^{\mathrm{T}}, \qquad S_{p^k}(\omega) = \frac{\boldsymbol{V}^{k\mathrm{T}} \boldsymbol{S}_f(\omega) \boldsymbol{V}^k}{\omega_k^4 d^{k2}}, \quad k = 1, \ldots, n, \tag{41}$$

$$S_{p^r p^s}(\omega) = \frac{\boldsymbol{V}^{r\mathrm{T}} \boldsymbol{S}_f(\omega) \boldsymbol{V}^s}{\omega_r^2 \omega_s^2 d^r d^s}, \quad r, s = 1, \ldots, n. \tag{42}$$

Taking the Laplace transform of (32) and substituting $s = j\omega$, one gets

$$H^k(\omega) = \frac{q^k(\omega)}{p^k(\omega)} = \frac{\omega_k^2}{\omega_k^2 - \omega^2 + 2\zeta_k \omega_k j\omega}, \quad k = 1, \ldots, n, \tag{43}$$

$$S_{q^k}(\omega) = H^{k^*}(\omega) S_{p^k}(\omega) H^k(\omega), \qquad k = 1, \ldots, n, \tag{44}$$

where $H^{k^*}(\omega)$ is the conjugate function of $H^k(\omega)$. The relationships between the power spectra of system output in physical coordinate and system physical force are as follows:

$$S_{p^k}(\omega) = \frac{\boldsymbol{V}^{k\mathrm{T}} \boldsymbol{S}_f(\omega) \boldsymbol{V}^k}{\omega_k^4 d^{k2}}, \qquad k = 1, \ldots, n, \tag{45}$$

$$S_{p^r p^s}(\omega) = \frac{\boldsymbol{V}^{r\mathrm{T}} \boldsymbol{S}_f(\omega) \boldsymbol{V}^s}{\omega_r^2 \omega_s^2 d^r d^s}, \qquad r, s = 1, \ldots, n, \tag{46}$$

$$S_{q^k}(\omega) = H^{k^*}(\omega) S_{p^k}(\omega) H^k(\omega), \qquad k = 1, \ldots, n, \tag{47}$$

$$S_{q^r q^s}(\omega) = H^{r^*}(\omega) S_{p^r p^s}(\omega) H^s(\omega), \quad r, s = 1, \ldots, n, r \neq s, \tag{48}$$

$$\boldsymbol{S}_q(\omega) = \begin{bmatrix} S_{q^1} & \cdots & S_{q^1 q^k} & \cdots & S_{q^1 q^n} \\ \vdots & \ddots & & & \\ S_{q^k q^1} & & S_{q^k} & & S_{q^k q^n} \\ \vdots & & & \ddots & \\ S_{q^n q^1} & \cdots & S_{q^n q^k} & \cdots & S_{q^n} \end{bmatrix}, \tag{49}$$

$$\boldsymbol{S}_{v_j}(\omega) = \boldsymbol{V}_j \boldsymbol{S}_{\boldsymbol{q}}(\omega) \boldsymbol{V}_j{}^{\mathrm{T}}. \tag{50}$$

The correlation function of the response power spectrum is

$$\boldsymbol{R}_{v_j}(\tau) = \frac{1}{2\pi} \int_{-\infty}^{+\infty} \boldsymbol{S}_{v_j}(\omega) e^{i\omega\tau} d\omega. \tag{51}$$

Let $\tau = 0$. The root mean square (RMS) σ_{v_j} of the response v_j is

$$\boldsymbol{\sigma}_{v_j}^2 = \boldsymbol{R}_{v_j}(0) = \frac{1}{2\pi} \int_{-\infty}^{+\infty} \boldsymbol{S}_{v_j}(\omega) d\omega. \tag{52}$$

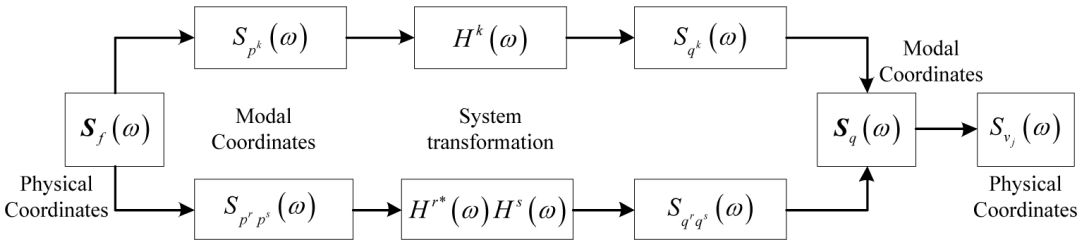

Figure 13. Transformation flow of PSD.

The transformation flow of PSD is shown in Figure 13.

According to the displacement PSD in physical coordinates, the velocity and acceleration PSD in physical coordinates can be obtained:

$$\boldsymbol{S}_{\dot{v}_j}(\omega) = \omega^2 \boldsymbol{S}_{v_j}(\omega), \tag{53}$$

$$\boldsymbol{S}_{\ddot{v}_j}(\omega) = \omega^4 \boldsymbol{S}_{v_j}(\omega). \tag{54}$$

When frequency is expressed in Hz, the relationship between the power spectra is described by

$$\boldsymbol{S}_{v_j}(f) = 2\pi \boldsymbol{S}_{v_j}(\omega). \tag{55}$$

5. Simulation results and analysis

It is supposed that the random vibration as input is a stationary Gauss process $\ddot{y}(t)$. The sampling function of $\ddot{y}(t)$ can be written approximately as Fourier series $\ddot{y}^d(t)$:

$$\ddot{y}^d(t) = \sum_{k=1}^{N} a_k \cos(\omega_k t + \varphi_k), \tag{56}$$

where the phase angle φ_k is an independent random variable with range $[0, 2\pi]$. The amplitude a_k is

$$a_k^2 = 4 S_{\ddot{y}}(\omega_k) \Delta\omega, \tag{57}$$

where $S_{\ddot{y}}(\omega)$ is the input PSD, $\Delta\omega = (\omega_u - \omega_l)/N$, ω_u and ω_l are frequency upper limit and lower limit value for input PSD. The frequency ω_k can be written as

$$\omega_k = \omega_l + (k - 1/2)\Delta\omega, \quad k = 1, 2, \ldots, N. \tag{58}$$

Equation (56) presents a stationary and ergodic Gaussian random process. The mean value is

$$E(\ddot{y}^d(t)) = \lim_{T\to\infty} \frac{1}{T} \sum_{k=1}^{N} a_k \int_0^T \cos(\omega_k t + \varphi_k)\, dt = 0. \tag{59}$$

The autocorrelation function is

$$\varphi_{\ddot{y}}^d(\tau) = \lim_{T\to\infty} \frac{1}{T} \int_0^T \ddot{y}^d(t)\ddot{y}^d(t+\tau) dt = \frac{1}{2} \sum_{k=1}^{N} a_k^2 \cos\omega_k \tau. \tag{60}$$

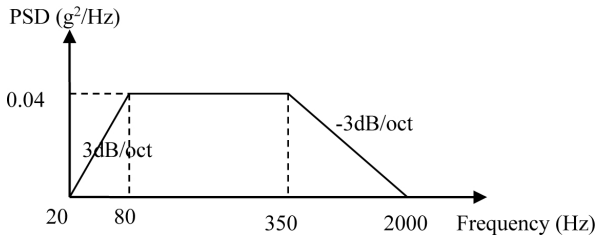

Figure 14. PSD of input acceleration.

The PSD of input acceleration is shown in Figure 14 with RMS value of 6.7 g. The input displacement and velocity time history is illustrated in Figure 15. Figure 16 demonstrates the theoretical simulation results for the displacement curve of payload when the MRE isolator is applied with a series of constant currents. The RMS values of payload with different currents are listed in Table 2 on page 582. It can be seen that with the increasing current, the RMS of displacement decreases and acceleration increases.

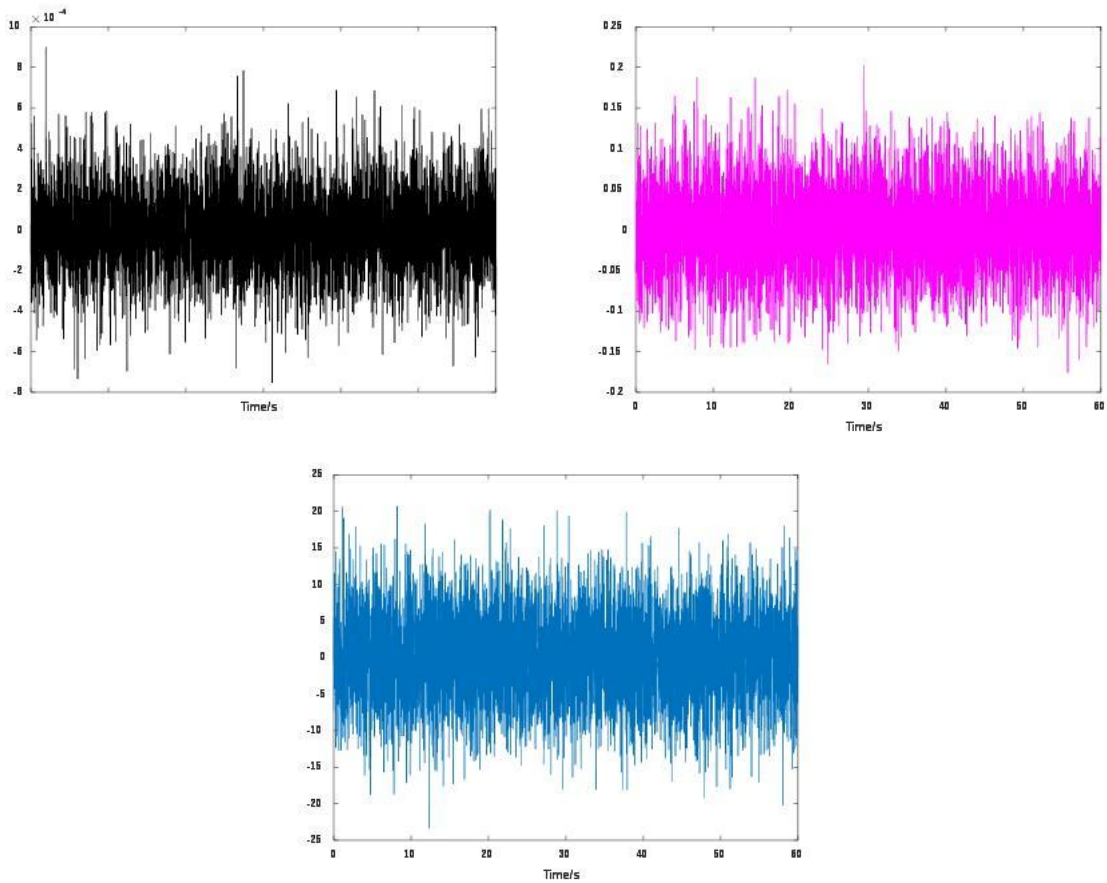

Figure 15. Input signals in time domain: displacement (top left), velocity (top right) and acceleration (bottom).

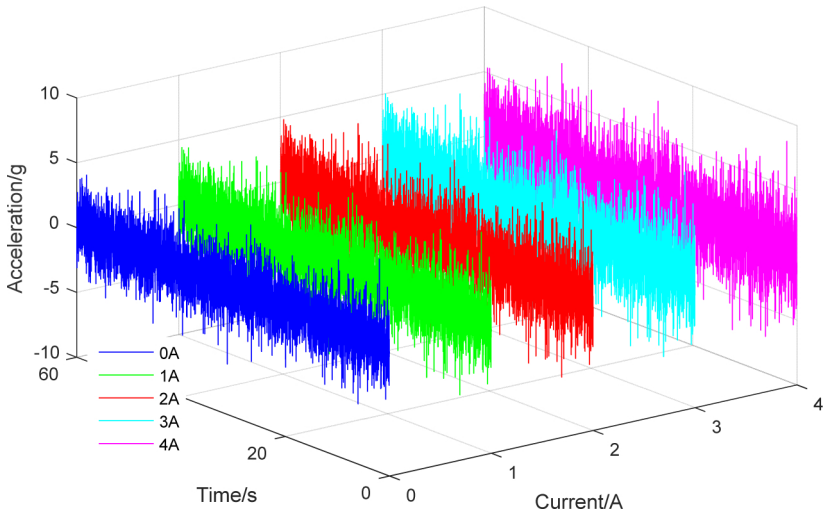

Figure 16. Acceleration of payload with a series of constant currents.

The changes of RMS values of displacement and acceleration are 11.38% and 39.71%, respectively. Figure 17 shows the PSD of the acceleration for payload when the MRE isolator is applied with a series of constant currents. The peak value of PSD is 1.07 g^2/Hz at 0.0 A. The peak value of PSD decreases by 48.8% when current is increased from 0.0 A to 4.0 A. The minimal root mean square value is 2.97 g when the current is 4.0 A. The resonance peak apparently shifts with the increasing current. The natural frequency change of a SDOF system is affected by changing the MRE isolator stiffness. These changes indicate that it is possible to control MRE isolator over varying stiffness and damping.

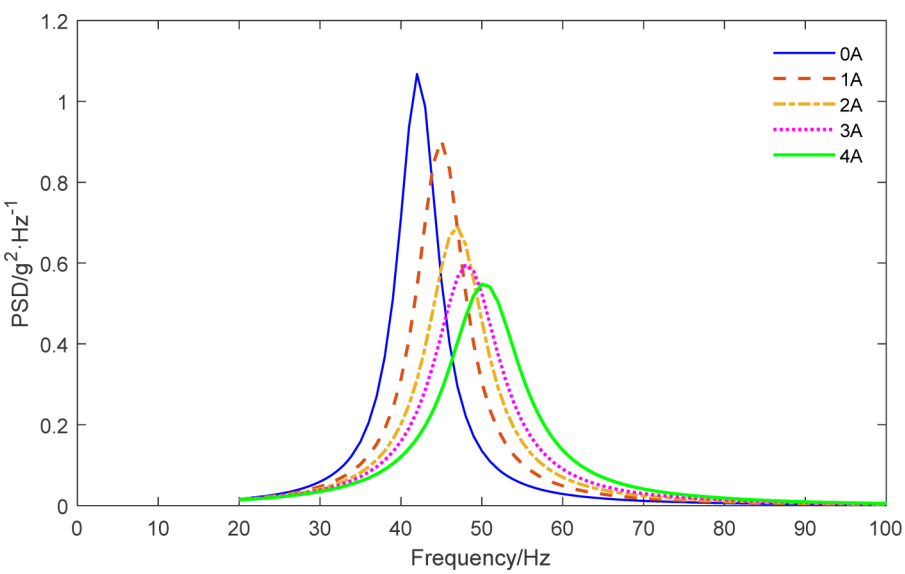

Figure 17. PSD of the payload acceleration with a series of constant currents.

	current/A					
root mean square	0	1	2	3	4	change
displacement/m	$5.91 \cdot 10^{-5}$	$5.79 \cdot 10^{-5}$	$5.47 \cdot 10^{-5}$	$5.32 \cdot 10^{-5}$	$5.24 \cdot 10^{-5}$	−11.38%
velocity/(m/s)	0.016	0.016	0.016	0.016	0.016	5.10%
acceleration/g	1.43	1.63	1.77	1.87	2.00	39.73%

Table 2. RMS values of payload with a series of constant currents.

6. Conclusions

This paper reports the design, fabrication, experimental tests and model simulation of the compression MRE isolator. The experimental results of MRE isolator exhibit that both its stiffness and the damping ratio are controllable with input currents. The simulation results show that the peak of PSD is reduced with increasing input current under random input vibration. Thus, it is demonstrated that the MRE isolator, whose mechanical properties can be controlled by an applied magnetic field, has potential applications where tuning vibration characteristics are desired.

Acknowledgements

The research was supported by Science Challenge Project (No. JCKY2016212A506-0104).

References

[Behrooz et al. 2014] M. Behrooz, X. Wang, and F. Gordaninejad, "Performance of a new magnetorheological elastomer isolation system", *Smart Mater. Struct.* **23**:4 (2014), art. id. 045014.

[Brancati et al. 2017] R. Brancati, G. Di Massi, and S. Pagano, "A vibration isolator based on magneto-rheological elastomer", pp. 483–490 in *Advances in Italian mechanism science* (Vincenza, Italy, 2016), edited by G. Boschetti and A. Gasparetto, Mech. Mach. Sci. **47**, Springer, 2017.

[Chen et al. 2013] G. Chen, X. Rui, F. Yang, J. Zhang, and Q. Zhou, "Study on the dynamics of laser gyro strapdown inertial measurement unit system based on transfer matrix method for multibody system", *Adv. Mech. Eng.* **5** (2013), art. id. 854583.

[Deng et al. 2006] H.-x. Deng, X.-l. Gong, and L.-h. Wang, "Development of an adaptive tuned vibration absorber with magnetorheological elastomer", *Smart Mater. Struct.* **15**:5 (2006), N111–N116.

[Dong et al. 2009] X.-m. Dong, M. Yu, C.-r. Liao, and W.-m. Chen, "A new variable stiffness absorber based on magneto-rheological elastomer", *Trans. Nonferr. Met. Soc. China* **19**:suppl. 3 (2009), S611–S615.

[Ginder et al. 2000] J. M. Ginder, M. E. Nichols, L. D. Elie, and S. M. Clark, "Controllable-stiffness components based on magnetorheological elastomers", pp. 418–425 in *Smart structures and materials* (Newport Beach, CA, 2000), edited by N. M. Wereley, Proc. SPIE **3985**, SPIE, Bellingham, WA, 2000.

[Kallio 2005] M. Kallio, "The elastic and damping properties of magnetorheological elastomers", technical report 565, Department of Materials Science, Tampere University of Technology, Finland, 2005.

[Liao et al. 2012] G. J. Liao, X.-L. Gong, S. H. Xuan, C. J. Kang, and H. Zong, "Development of a real-time tunable stiffness and damping vibration isolator based on magnetorheological elastomer", *J. Intell. Mater. Syst. Struct.* **23**:1 (2012), 25–33.

[Liu 2012] X. Liu, *Magnetorheological elastomer isolator in shear-compression mixed mode*, master's thesis, Chongqing University, 2012.

[Tao et al. 2019] Y. Tao, X. Rui, F. Yang, and B. Hao, "Development of a MRE isolation system for strapdown inertial measurement unit", *Mech. Syst. Signal Process.* **117** (2019), 553–568.

[Yang et al. 2014] F. Yang, X. Rui, Z. Song, and G. Chen, "Vibration effects analysis of IMU by transfer matrix method for multibody system", pp. 101–106 in *Proceedings of the Fifth International Conference on Mechanical Engineering and Mechanics* (Jiangsu, China, 2014), China Acad. J. Elect. Publ., Beijing, 2014.

[Yang et al. 2016] J. Yang, S. Sun, T. Tian, W. Li, H. Du, G. Alici, and M. Nakano, "Development of a novel multi-layer MRE isolator for suppression of building vibrations under seismic events", *Mech. Syst. Signal Process.* **70-71** (2016), 811–820.

Received 5 Feb 2020. Revised 2 Jun 2020. Accepted 27 Jun 2020.

YANG FUFENG: fufengyang@aliyun.com
, *Nanjing University of Science and Technology, 200 Xiaoling Wei Street, Jiangsu Province, Nanjing, 210094, China*

TAO YU: shirleyo0o@163.com
, *Xi'an Technological University, 2 Xuefu Middle Road, Weiyang District, Shaanxi Province, Xi'an, 710021, China*

JOURNAL OF MECHANICS OF MATERIALS AND STRUCTURES
Vol. 15, No. 5, 2020
https://doi.org/10.2140/jomms.2020.15.585

ANALYTICAL SOLUTIONS FOR DISPLACEMENTS AND STRESSES IN FUNCTIONALLY GRADED THICK-WALLED SPHERES SUBJECTED TO A UNIDIRECTIONAL OUTER TENSION

CHENYI ZHENG AND CHANGWEN MI

In the context of infinitesimal theory of elasticity, we derived analytical solutions for displacements and stresses in functionally graded thick-walled spheres under the application of a uniaxial outer tension. While the shear modulus in the graded sphere is allowed to vary as a power-law function of radial coordinate, the Poisson's ratio is treated as a constant. The semiinverse method of elasticity is first employed for proposing correct function forms of the radial and longitudinal displacements. The elastostatic Navier's equations of the power-law graded sphere lead to a system of second-order differential equations of the Euler type. The order is then reduced and the system is recast into a first-order differential matrix equation. Analytical solutions are subsequently developed by the coupling of differential equation and eigenvalue theories. Successfully solving this particular problem provides a valid analytical solution scheme for exploring elastic fields in graded hollow spheres subjected to nonhydrostatic boundary loads. In order to examine the effects of the power-law gradation and the radii ratio of the thick-walled sphere on stress distributions and stress concentration factors, extensive parametric studies are conducted. Analytical solutions of the graded thick-walled sphere are further compared with those of the homogeneous case as well as with the numerical results due to finite element modelings. The obtained results show that the property gradation significantly affects stress distributions through the thickness direction of the graded thick-walled sphere. When the shear modulus is designed as an increasing function of the radial coordinate, the high stress zone conventionally occurring near the inner boundary of homogeneous thick-walled spheres tends to shift toward to the outer surface vicinity. For a given radii ratio, an optimal power-law gradation leading to the lowest stress concentration factor can always be identified. The proposed method of solution and the obtained results are useful for the design and manufacturing of better performing spherical vessels.

1. Introduction

It is a well accepted fact that stress concentration (SC) is an inherent threatening to the structural integrity of pressure vessels. The concentration of stresses typically occurs near the reentrant boundaries, geometric defects and points of force application. The maximum stress may be as high as several times of the applied load. In the literature, this ratio is defined as the stress concentration factor (SCF) for a certain combination of structure and loading conditions [Barber 1992]. Scientists and engineers have been working hard to reduce and avoid SC both in theory and in engineering practice. One idea is to replace

Changwen Mi is the corresponding author.

Keywords: functionally graded spheres, unidirectional loading, analytical solution, stress concentration factor, finite element modeling.

the completely homogeneous material of an engineering component with functionally graded materials (FGMs). Within the context of mechanics, FGMs are a relatively new design strategy to regulate and optimize the stress distributions in engineering materials and structures. The most typical example is the combination of ceramic and metallic materials [Evci and Gülgeç 2018]. Fukui and Yamanaka [1992] evaluated the stresses in graded thick-walled tubes made by the combination of a matrix composed of three low-modulus materials and high-modulus particles. The gradation profile through the tube thickness is controlled by the volume fraction of the reinforcement particles. Suresh et al. [1999] demonstrated that a thin coating made of graded alumina-glass composite significantly reduces the sliding contact damage of a polycrystalline alumina surface. As a direct result of the replacement, the modulus of elasticity is allowed to vary through one or more spatial dimensions. In any theory of mechanics, both deformations and stresses are closely related to elastic modulus. It is hoped that, through the proper regulation of elastic modulus, stresses may redistribute following a desired pattern.

Materials and structures with graded modulus of elasticity [Birman and Byrd 2007; Ghayesh and Farajpour 2019] have been designed and manufactured since 1980s and gained many applications in contact mechanics [Suresh et al. 1999; Yan et al. 2019; Yan and Mi 2019] and fracture mechanics [Jin and Batra 1996]. Tutuncu and Ozturk [2001] derived closed-form displacements and stresses of graded cylindrical and spherical vessels under internal pressure alone. The shear modulus was also assumed to vary as a power-law function through the wall thickness. Tutuncu [2007] further derived power series solutions to a thick-walled cylinder under the application of internal pressure only. This time, the elastic modulus of the cylinder is assumed to be an exponential function of the radial coordinate. Due to this change of gradation function, an analytical solution to the axisymmetric equilibrium equations of the radial displacement becomes more difficult. As a result, the author presented the solution in the form of power series by employing the Frobenius method. The closed-form solution of this problem was later derived by Nejad et al. [2016] in the plain strain condition. Atashipour et al. [2014] solved the elastic fields in a homogeneous hollow sphere internally coated with a graded layer under hydrostatic boundary pressures. Analytical solutions were derived for graded coating with both linearly and exponentially-varying shear modulus. More recently, Evci and Gülgeç [2018] developed an analytical solution in a graded hollow cylinder whose thermoelastic material properties are assumed to be power functions of the radial coordinate.

As a powerful numerical approach, finite element (FE) analysis has also been employed for solving cylindrical and spherical vessels under the application of hydrostatic loads. Nejad et al. [2016] compared their analytical solutions with those resulting from the FE modelings. Ghannad and Nejad [2012] first derived a complete analytical solution to thick-walled spheres with power-law gradation of elastic modulus. The distribution of displacements and stresses were compared with those obtained by the FE method. Apart from completely graded vessels [Ghannad 2013; Dryden and Batra 2013; Xin et al. 2014; Yang et al. 2015], thick-walled cylinders and spheres reinforced with a graded coating have also been studied. Sburlati and Cianci [2015] investigated the effects of a graded interphase zone bridging a spherical inclusion and a matrix subjected to a far-field pressure loading. The same structure under the application of a uniform heating has also been considered [Sburlati et al. 2017].

All works reviewed above dealt with hollow cylinders and spheres under the application of hydrostatic pressures. Nonhydrostatic traction loads did not receive reasonable attentions until the last decade. Based on the multiple isoparametric FE formulation, Kubair and Bhanu-Chandar [2008] numerically

determined the SCF in a cylindrical panel containing a circular hole under the application of a far-field uniaxial tension. Since the problem was numerically solved, both the power-law and exponential variations of elastic modulus were considered. By the use of Airy stress function approach, Nie and Batra [2010] derived analytical solutions of a graded hollow cylinder under normal and shear tractions applied at its both boundaries. Mohammadi et al. [2011] evaluated the SCFs around a circular hole in a radially graded plate subjected to either equal-biaxial or pure shear far-field tractions. Kubair [2013] further derived closed-form elastic fields for the same panel geometry under the application of a far-field antiplane shear loading. This time, only the exponential variation of elastic modulus was considered. Sburlati [2013] derived an analytical solution to a circularly voided homogeneous plate reinforced by a graded ring under the application of a far-field uniaxial tension. On this basis, Sburlati et al. [2014] further considered the same geometry under the application of four different far-field loads, including uniaxial tension, equal-biaxial tension and two forms of pure shear. Yang and Gao [2016] evaluated the SCFs in a homogenous panel containing an elliptic hole that is reinforced by a graded coating layer. Arbitrary loads and property gradations in the graded coating can be considered. Le [2017] developed an asymptotically exact two-dimensional theory for functionally graded piezoelectric shells by synthesizing the variational and asymptotic methods. As an application, the analytical solution to the forced vibration of a graded piezoceramic cylindrical shell excited by a harmonic voltage was derived. Li et al. [2018] considered a homogeneous thick-walled cylinder reinforced by a graded coating subjected to an arbitrary biaxial outer loading. The effects of the graded coating on the reduction of SC and the optimization of stress distributions were analyzed.

The references reviewed above demonstrate that fewer works have devoted to graded thick-walled spheres subjected to nonhydrostatic loads. Poultangari et al. [2008] first proposed a series solution for a power-law graded hollow sphere under the application of nonhydrostatic thermomechanical loads. Later, the same research group further employed this solution method for solving the piezothermoelastic fields in standalone graded hollow spheres [Jabbari et al. 2013] and graded hollow spheres perfectly bonded by piezoelectric layers [Barati and Jabbari 2015; Jabbari et al. 2017]. Also based on the series solution principle, Bayat and EkhteraeiToussi [2015] investigated the thermomechanical fields in a transversely isotropic hollow sphere rotating at a constant angular velocity. Sburlati et al. [2018] derived elastic solutions in an inhomogeneous spherical interphase separating a solid spherical inclusion and a finite matrix. By assuming a power-law variation in shear modulus and a constant Poisson's ratio, closed-form solutions to both hydrostatic and pure-shear outer tractions were developed. In another recent paper, Zheng et al. [2019] developed a semianalytical solution to a homogeneous hollow sphere interiorly coated with a graded layer. Although a uniaxial outer tension was considered, displacements and stresses of the graded coating were not directly solved within the elasticity theory of an inhomogeneous medium. Instead, the solution was approximated by its homogeneous counterpart through discretizing the graded coating into a few perfectly bonded homogeneous sublayers [Yang et al. 2009; Yang and Gao 2016].

The goal of this work is to continue the efforts in this line of research. Here, we consider the fundamental problem of a graded thick-walled sphere under the application of a uniaxial outer tension. The hollow sphere is assumed to possess power-law variation of shear modulus through its thickness. Since the Poisson's ratio is treated as a constant, Young's modulus of the isotropic thick-walled sphere also varies by the same power-law function. Following the basic equations of an inhomogeneous elastic medium, the boundary value problem is solved by the collective use of semiinverse method of elasticity

theory, reduced-order method of differential equations and eigenvalue theory. In addition to analytical solutions, FE modelings are also implemented to validate the correctness of stress distributions and SCFs. The remainder of this paper is structured as follows. Section 2 describes the mechanical formulation and analytical solutions to the graded thick-walled sphere under the application of a uniaxial outer tension. In Section 3, extensive parametric studies are conducted for illustrating the effects of property gradation and radii ratio on stress distributions and reduction of SCFs. FE modeling results are also presented to validate the correctness of analytical solutions. Finally, in Section 4, concluding remarks are delivered.

2. Method of solution

Figure 1 shows a graded thick-walled sphere under the application of a unidirectional outer tension of magnitude T. The inner and outer radius of the sphere are represented by a and b, respectively. Given the spherical symmetry of the geometry, spherical coordinates (R, φ, θ) are employed for the subsequent mechanical formulation, where R, φ and θ denote the radial, longitudinal and latitudinal coordinates, respectively. In view of its limited influence on stress distributions, the Poisson's ratio (ν) of the graded sphere is assumed to be a constant [Sburlati 2013]. The shear modulus of the graded sphere varies as a power-law function of the radial coordinate:

$$G = G_o R^m / b^m, \tag{1}$$

where G_o denotes the shear modulus value at the outer boundary of the graded sphere and m is the grading index, indicating the varying gradient of the shear modulus. It is worth noting that shear modulus instead of Young's modulus has been used in Equation (1). For the method of displacement potentials used in this work, the combination of shear modulus and Poisson's ratio is able to formulate the solution in the simplest form than any other combinations of elastic constants.

In spherical coordinates, the unidirectional tension applied at the outer boundary of the graded sphere can be expressed as

$$\frac{\sigma_R(b,\zeta)}{T} = \zeta^2, \quad \frac{\sigma_{R\varphi}(b,\zeta)}{T} = -\zeta\sqrt{1-\zeta}, \tag{2}$$

where $\zeta = \cos\varphi$. At the inner surface of the graded sphere, both the normal and the shear tractions are zero:

$$\sigma_R(a,\zeta) = 0, \quad \sigma_{R\varphi}(a,\zeta) = 0. \tag{3}$$

In spite of the dependence of shear modulus on the radial coordinate, the governing equations for the graded thick-walled sphere are not different from those for a homogeneous medium. The strain-displacement relations are given by

$$\begin{gathered}\varepsilon_R = \frac{\partial u_R}{\partial R}, \quad \varepsilon_\varphi = \frac{u_R}{R} - \frac{\sqrt{1-\zeta^2}}{R}\frac{\partial u_\varphi}{\partial \zeta}, \quad \varepsilon_\theta = \frac{u_R}{R} + \frac{\zeta u_\varphi}{R\sqrt{1-\zeta^2}}, \\ \varepsilon_{R\varphi} = \frac{1}{2}\left(\frac{\partial u_\varphi}{\partial R} - \frac{\sqrt{1-\zeta^2}}{R}\frac{\partial u_R}{\partial \zeta} - \frac{u_\varphi}{R}\right).\end{gathered} \tag{4}$$

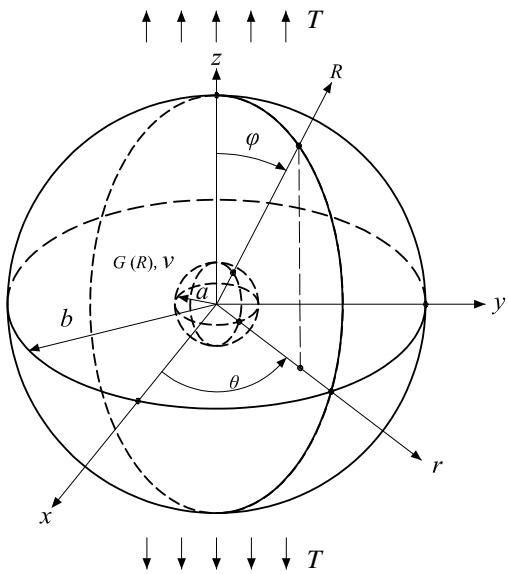

Figure 1. A thick-walled sphere with radially graded shear modulus under the application of a unidirectional outer tension.

In terms of the inhomogeneous shear modulus (1), the linear constitutive relations still assume the form

$$\sigma_R=\frac{2G(R)\nu}{1-2\nu}(\varepsilon_R+\varepsilon_\theta+\varepsilon_\varphi)+2G(R)\varepsilon_R,\quad \sigma_\varphi=\frac{2G(R)\nu}{1-2\nu}(\varepsilon_R+\varepsilon_\theta+\varepsilon_\varphi)+2G(R)\varepsilon_\varphi,$$
$$\sigma_\theta=\frac{2G(R)\nu}{1-2\nu}(\varepsilon_R+\varepsilon_\theta+\varepsilon_\varphi)+2G(R)\varepsilon_\theta,\quad \sigma_{R\varphi}=2G(R)\varepsilon_{R\varphi}. \tag{5}$$

In the absence of body forces, the axisymmetric equations of equilibrium in spherical coordinates are given by [Barber 1992]

$$\frac{\partial\sigma_R}{\partial R}+\frac{\zeta\sigma_{R\varphi}}{R\sqrt{1-\zeta^2}}-\frac{\sqrt{1-\zeta^2}}{R}\frac{\partial\sigma_{R\varphi}}{\partial\zeta}+\frac{2\sigma_R-\sigma_\theta-\sigma_\varphi}{R}=0,$$
$$\frac{\zeta(\sigma_\varphi-\sigma_\theta)}{R\sqrt{1-\zeta^2}}-\frac{\sqrt{1-\zeta^2}}{R}\frac{\partial\sigma_\varphi}{\partial\zeta}+\frac{\partial\sigma_{R\varphi}}{\partial R}+\frac{3\sigma_{R\varphi}}{R}=0. \tag{6}$$

In view of the traction distributions (2), the constitutive equations (5) and the strain-displacement relations (4), it can be inferred that the radial and longitudinal displacements in the graded sphere must follow the form

$$u_R=P_1(R)+\zeta^2P_2(R),\quad u_\varphi=\zeta\sqrt{1-\zeta^2}P_3(R). \tag{7}$$

Only when the displacements are in these forms, the traction boundary conditions (2) can possibly be satisfied. By the substitution of the proposed displacements (7) back into the three sets of governing equations (4), (5) and (6), the equations of equilibrium of the graded sphere become

$$\frac{G_o R^{m-2}}{(1-2\nu)\, b^m}\left(H_1(R)+\zeta^2 H_2(R)\right)=0, \quad \frac{G_o R^{m-2}}{(1-2\nu)\, b^m}\zeta\sqrt{1-\zeta^2}H_3(R)=0, \tag{8}$$

where $H_1(R)$, $H_2(R)$ and $H_3(R)$ are functions of the radial coordinate:

$$\begin{aligned} H_1(R) = &-2(1-\nu)\, P_1''(R)R^2 - \left[2(1-\nu)(m+2)\, P_1'(R) - P_3'(R)\right] R \\ &+4(1-\nu-m\nu)\, P_1(R) - 2(1-2\nu)\, P_2(R) - (3-2\nu(m+2))\, P_3(R), \end{aligned} \tag{9a}$$

$$\begin{aligned} H_2(R) = &-2(1-\nu)\, P_2''(R)R^2 - \left[2(1-\nu)(m+2)\, P_2'(R) + 3P_3'(R)\right] R \\ &+2(5-2\nu(m+4))\, P_2(R) + 3(3-2\nu(m+2))\, P_3(R), \end{aligned} \tag{9b}$$

$$\begin{aligned} H_3(R) = &-(1-2\nu)\, P_3''(R)R^2 - \left[(1-2\nu)(m+2)\, P_3'(R) - 2P_2'(R)\right] R \\ &+2(4(1-\nu) - m(1-2\nu))\, P_2(R) + (12(1-\nu) + m(1-2\nu))\, P_3(R). \end{aligned} \tag{9c}$$

Since $\zeta = \cos\varphi$ may take any value within the closed interval $[-1, 1]$, equations (8) can be satisfied if and only if

$$H_1(R)=0, \quad H_2(R)=0, \quad H_3(R)=0. \tag{10}$$

These are three coupled differential equations of Euler type with respect to the three unknown functions $P_1(R)$, $P_2(R)$ and $P_3(R)$. By replacing the radial coordinate with $R = e^t$ in (9), equations (10) reduce to a system of coupled ordinary differential equations:

$$\begin{aligned} &-2(1-\nu)\, P_1''(t) - 2(1-\nu)(m+1)\, P_1'(t) + P_3'(t) \\ &\quad +4(1-\nu-m\nu)\, P_1(t) - 2(1-2\nu)\, P_2(t) - (3-2\nu(m+2))\, P_3(t) = 0, \end{aligned} \tag{11a}$$

$$\begin{aligned} &-2(1-\nu)\, P_2''(t) - 2(1-\nu)(m+1)\, P_2'(t) - 3P_3'(t) \\ &\quad +2(5-2\nu(m+4))\, P_2(t) + 3(3-2\nu(m+2))\, P_3(t) = 0, \end{aligned} \tag{11b}$$

$$\begin{aligned} &-(1-2\nu)\, P_3''(t) + 2P_2'(t) - (1-2\nu)(m+1)\, P_3'(t) \\ &\quad +(8(1-\nu) + 2m(1-2\nu))\, P_2(t) + (12(1-\nu) + m(1-2\nu))\, P_3(t) = 0. \end{aligned} \tag{11c}$$

These three ordinary differential equations may further be expressed in matrix form as

$$\mathrm{d}\boldsymbol{W}/\mathrm{d}t = \boldsymbol{Q}\boldsymbol{W}, \tag{12}$$

with $\boldsymbol{W}$ denoting a column vector composed of the three unknown functions and their derivatives:

$$\boldsymbol{W} = \left[\, P_1(t) \;\; P_2(t) \;\; P_3(t) \;\; P_1'(t) \;\; P_2'(t) \;\; P_3'(t) \,\right]^T, \tag{13}$$

and $\boldsymbol{Q}$ representing a 6×6 square matrix:

$$\boldsymbol{Q} = \begin{bmatrix} 0 & 0 & 0 & 1 & 0 & 0 \\ 0 & 0 & 0 & 0 & 1 & 0 \\ 0 & 0 & 0 & 0 & 0 & 1 \\ \frac{2(1-\nu-m\nu)}{1-\nu} & -\frac{1-2\nu}{1-\nu} & -\frac{3-2\nu(2+m)}{2(1-\nu)} & -1-m & 0 & \frac{1}{2(1-\nu)} \\ 0 & \frac{5-2\nu(4+m)}{1-\nu} & \frac{9-6\nu(2+m)}{2(1-\nu)} & 0 & -1-m & -\frac{3}{2(1-\nu)} \\ 0 & \frac{8(1-\nu)+2m(1-2\nu)}{1-2\nu} & \frac{12(1-\nu)+m(1-2\nu)}{1-2\nu} & 0 & \frac{2}{1-2\nu} & -1-m \end{bmatrix}. \tag{14}$$

Equation (12) can be solved by coupling the solutions of an inhomogeneous first-oder differential equation and eigenvalue problems of a square matrix. To this end, the six eigenvalues of the coefficient matrix $\boldsymbol{Q}$ must first be found:

$$\lambda_{1,2} = \frac{k_1 \pm \sqrt{k_2}}{k_0}, \quad \lambda_{3,4} = \frac{k_1 \pm \sqrt{k_3 - 2\sqrt{k_4}}}{k_0}, \quad \lambda_{5,6} = \frac{k_1 \pm \sqrt{k_3 + 2\sqrt{k_4}}}{k_0}, \tag{15}$$

where k_0 through k_4 are five dimensionless parameters that can be expressed in terms of Poisson's ratio and the grading index:

$$\begin{aligned}
k_0 &= 2(1-\nu)(1-2\nu),\\
k_1 &= -(1-\nu)(1-2\nu)(m+1),\\
k_2 &= (1-\nu)(1-2\nu)^2\big((1-\nu)(9+m^2)+2m(1-5\nu)\big),\\
k_3 &= m^2(1-\nu)^2(1-2\nu)^2 + 4m(1-\nu)(1-2\nu)^3 + 29 - 174\nu + 377\nu^2 - 348\nu^3 + 116\nu^4,\\
k_4 &= (1-\nu)^2(1-2\nu)^4\big(m^2(1-22\nu+25\nu^2) + 4m(11-36\nu+25\nu^2) + 100(1-\nu)^2\big).
\end{aligned} \tag{16}$$

For Poisson's ratio $\nu \in (0, 0.5)$, all six eigenvalues of the coefficient matrix (15) are real for the grading index $0 < m \leq 2$. As a result, the general solution of the differential matrix equation (12) can be given by the linear combination of the six eigenvalues:

$$P_1(t) = \sum_{k=1}^{6} \frac{A_k}{a^{\lambda_k - 1}} e^{\lambda_k t}, \quad P_2(t) = \sum_{k=1}^{6} \frac{B_k}{a^{\lambda_k - 1}} e^{\lambda_k t}, \quad P_3(t) = \sum_{k=1}^{6} \frac{C_k}{a^{\lambda_k - 1}} e^{\lambda_k t}. \tag{17}$$

In these equations, replacing the independent variable t with $\ln R$ leads to

$$P_1(R) = \sum_{k=1}^{6} \frac{A_k}{a^{\lambda_k - 1}} R^{\lambda_k}, \quad P_2(R) = \sum_{k=1}^{6} \frac{B_k}{a^{\lambda_k - 1}} R^{\lambda_k}, \quad P_3(R) = \sum_{k=1}^{6} \frac{C_k}{a^{\lambda_k - 1}} R^{\lambda_k}. \tag{18}$$

Recall that, altogether, these three functions must satisfy the two equations of equilibrium (8). The three groups of coefficients, A_k, B_k and C_k, are therefore not independent. By the substitution of (18) back into (8), we can obtain

$$B_k = S(\lambda_k) A_k, \quad C_k = L(\lambda_k) A_k, \tag{19}$$

where $S(\lambda_k)$ and $L(\lambda_k)$ are given by

$$\begin{aligned}
S(\lambda_k) &= \frac{\big(2m\nu - (1-\nu)(2-(m+1)\lambda_k - \lambda_k^2)\big)\big(12(1-\nu) + (1-2\nu)(m - (m+1)\lambda_k - \lambda_k^2)\big)}{2\big((1-\nu)(m+4\nu-6\nu m - 2\nu(m+1+\lambda_k)\lambda_k) - m^2\nu(1-2\nu)\big)},\\
L(\lambda_k) &= -\frac{\big(2m\nu - (1-\nu)(2-(m+1)\lambda_k - \lambda_k^2)\big)\big(4(1-\nu) + m(1-2\nu) + \lambda_k\big)}{(1-\nu)\big(m+4\nu-6\nu m - 2\nu(m+1+\lambda_k)\lambda_k\big) - m^2\nu(1-2\nu)}.
\end{aligned} \tag{20}$$

With equations (19), the 18 unknown coefficients have reduced to only six: A_1, A_2, A_3, A_4, A_5, A_6. They remain to be determined by implementing the traction boundary conditions at the outer surface (2) and the inner surface (3) of the graded sphere.

Given the general solutions of the three unknown functions (18) in the radial and longitudinal displacement (7), it is straightforward to derive the general expressions of displacements. The four nontrivial

strain components can be further derived from the strain-displacement relations (4). Finally, with the help of the shear modulus distribution (1), the radial and longitudinal stresses (5) can be recast

$$\frac{\sigma_R}{T} = \frac{R^m}{b^m}\sum_{k=1}^{6} A_k\left(\alpha_k + \zeta^2\beta_k\right)\frac{a^{1-\lambda_k}}{R^{1-\lambda_k}}, \quad \frac{\sigma_{R\varphi}}{T} = \zeta\sqrt{1-\zeta^2}\frac{R^m}{b^m}\sum_{k=1}^{6} A_k\gamma_k\frac{a^{1-\lambda_k}}{R^{1-\lambda_k}}, \tag{21}$$

where α_k, β_k and γ_k $(k = 1, \ldots, 6)$ are all dimensionless functions of the shear modulus G_o, the magnitude of the applied uniaxial tension T, Poisson's ratio ν, the grading index m and the eigenvalues λ_k:

$$\alpha_k = \frac{2G_o}{(1-2\nu)\,T}\left((1-\nu)\,\lambda_k + \nu\,(2 - L\,(\lambda_k))\right), \tag{22a}$$

$$\beta_k = \frac{2G_o}{(1-2\nu)\,T}\left((1-\nu)\,\lambda_k S\,(\lambda_k) + \nu\,(2S\,(\lambda_k) + 3L\,(\lambda_k))\right), \tag{22b}$$

$$\gamma_k = -\frac{G_o}{T}\left(2S\,(\lambda_k) + (1-\lambda_k)\,L\,(\lambda_k)\right). \tag{22c}$$

Equations (21) are valid expressions of the radial and shear stresses for any graded hollow sphere with the shear modulus distribution given by (1). The six unknown coefficients $(A_1, \ldots, A_6)$ are adjustable parameters that remain to be determined by satisfying specific traction or displacement boundary conditions at both the inner and the outer surfaces of the hollow sphere. Upon implementing the uniaxial outer tension condition (2) at $R = b$ and the traction-free condition (3) at $R = a$, we arrive at four simultaneous algebraic equations. In these equations, equating those terms independent of the variable ζ, preceding ζ^2 and $\zeta\sqrt{1-\zeta^2}$ leads to six linear equations about the six unknown coefficients $(A_1, \ldots, A_6)$. This set of equations may be restructured into a single matrix equation:

$$[\boldsymbol{U}]\,\{\boldsymbol{X}\} = \{\boldsymbol{V}\}, \tag{23}$$

where the components of the 6×6 square matrix $\boldsymbol{U}$ are given by

$$U_{1k} = \alpha_k, \quad U_{2k} = \beta_k, \quad U_{3k} = \gamma_k, \quad U_{4k} = \frac{\alpha_k a^{1-\lambda_k}}{b^{1-\lambda_k}}, \quad U_{5k} = \frac{\beta_k a^{1-\lambda_k}}{b^{1-\lambda_k}}, \quad U_{6k} = \frac{\gamma_k a^{1-\lambda_k}}{b^{1-\lambda_k}}; \tag{24}$$

$\boldsymbol{X}$ is column vector composed of the six unknowns

$$\boldsymbol{X} = \left\{\begin{array}{cccccc} A_1 & A_2 & A_3 & A_4 & A_5 & A_6 \end{array}\right\}^T; \tag{25}$$

and $\boldsymbol{V}$ is also a column vector with the simple form

$$\boldsymbol{V} = \left\{\begin{array}{cccccc} 0 & 0 & 0 & 0 & 1 & -1 \end{array}\right\}^T. \tag{26}$$

The algebraic matrix equation (23) is linear with respect to the six unknowns. As a result, its solution procedure follows the standard linear algebra algorithm. The six unknowns can be easily found:

$$A_k = (\boldsymbol{U}^{-1})_{k5} - (\boldsymbol{U}^{-1})_{k6} = \frac{(\boldsymbol{U})'_{5k} - (\boldsymbol{U})'_{6k}}{|\boldsymbol{U}|}, \tag{27}$$

where $\boldsymbol{U}^{-1}$, $\boldsymbol{U}'$ and $|\boldsymbol{U}|$ are the inverse, matrix of cofactors and determinant of the coefficient matrix $\boldsymbol{U}$. Since there are only two nonzero components in the column vector $\boldsymbol{V}$, only the last two rows of the matrices of inverse and cofactors are required in the solutions.

In view of equations (24), closed-form expressions of the unknowns A_k can be further developed without difficulty. Nonetheless, the results are quite lengthy. For brevity, they are not presented in the manuscript. Interested readers are invited to implement the solution procedure in a symbolic mathematical software.

3. Results and discussion

In the last section, we developed an analytical solution to a graded thick-walled sphere subjected to a uniaxial outer tension. For brevity, the closed-form expressions of the final results were not presented. The purpose of the present section is to further explore the effects of the power-law grading index m and the radii ratio b/a on both the stress distributions and the SCFs in terms of numerical experiments.

As can be concluded from previous studies on graded cylinders and spheres [Sburlati 2013], the effects of Poisson's ratio on stress fields are inessential when compared with those of the shear modulus. Xin et al. [2014] further provided one theoretical foundation for justifying the assumption of constant Poisson's ratio extensively adopted in the literature. They indicated that, although the effects of Poisson's ratio on the radial displacement of a thick-walled tube under internal pressure are appreciable, those on stresses are not obvious. As a result, the Poisson's ratio was fixed as $\nu = 0.3$ in all our case studies.

As a means of verifying and validating the correctness of the developed theoretical formulation, FE solutions calculated through ABAQUS/Standard software were also prepared for most examples. In all numerical experiments, the shear modulus at the outer boundary of the thick-walled sphere was taken as $G_o = 80\,\text{GPa}$. The magnitude of the uniaxial outer tension was chosen as $T = 50\,\text{MPa}$.

Previous studies demonstrate that high moduli of elasticity near the inner boundary of a thick-walled sphere tend to worsen stress concentrations [Zheng et al. 2019]. In order to relieve the stress concentrations that typically occur at the inner surface of hollow spheres, their modulus of elasticity should be designed as an increasing function of the radial coordinate. In other words, near the conventional stress concentration zone, soft materials should be employed. For regions far way from the void, hard materials can still be used. This design principle helps to drive the high-stress zone near the spherical void toward to the outer boundary of the thick-walled sphere. On the basis of such an argument, only positive grading indices should be considered in (1). For the special case of zero grading, the proposed graded thick-walled sphere of course reduces to a completely homogeneous medium.

Figure 2 shows the distribution of the longitudinal stress along the inner surface of the graded thick-walled sphere for the particular radii ratio $b/a = 3$. To investigate the effects of modulus inhomogeneity, five positive grading indices were considered. For completeness, the classical solution of a homogeneous thick-walled sphere is included in the figure. It can be seen from the figure that, the introduction of an inhomogeneous shear modulus does not change the distribution pattern of the longitudinal stress along the inner boundary. For any grading index, the maximum value of this stress component still occurs along the equator of the inner surface ($\varphi = \pi/2, 0 \le \theta \le 2\pi$). Due to symmetry, the minimum value of the longitudinal stress takes place at both poles of the inner surface ($\varphi = 0, \pi$). The longitudinal stress varies monotonically with the grading index. As m increases, the magnitude of both the maximum and the minimum longitudinal stress decreases, indicating the desired effects of modulus inhomogeneity on stress concentrations.

Because, on the inner surface of a graded thick-walled sphere, stress concentrations always occur

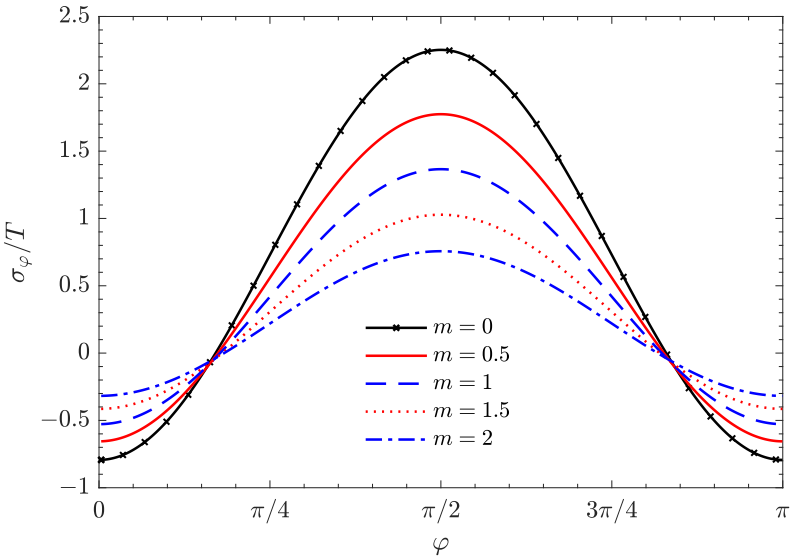

Figure 2. Variation of dimensionless longitudinal stress along the inner surface of the graded thick-walled sphere for five grading indices ($b/a = 3$, $R = a$).

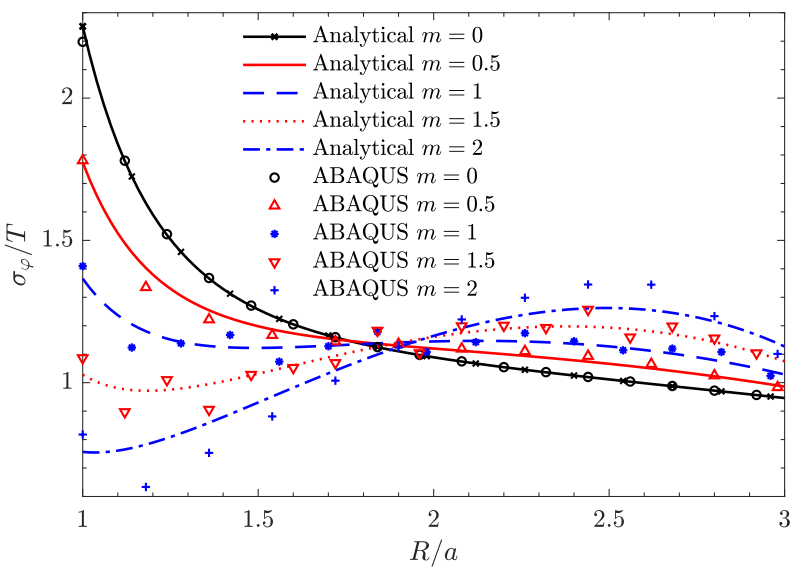

Figure 3. Variation of dimensionless longitudinal stress with radial distance for five grading indices ($b/a = 3$, $\varphi = \pi/2$).

along the equator, it is informative to further examine the variation of the longitudinal stress between the inner and the outer equators of the sphere (Figure 3). The same five grading indices as studied in Figure 2 were considered. It is now even more obvious that, at the inner surface of the graded sphere, the longitudinal stress decays monotonically with increased grading index. For the particular thickness ratio ($b/a = 3$), the highest stress concentration still occurs at the equator of the inner surface when $m = 0.5$

and 1. In particular, when $m = 0.5$, the longitudinal stress decays rapidly with the radial distance from the center of the sphere. However, the rate of decay becomes much slower as the grading index increases to $m = 1$. Near the middle interface of the sphere, a stress plateau can be clearly observed. In addition to the highest longitudinal stress occurring at the inner surface of the sphere, another local stress maximum has also appeared at $R/a = 2.12$. The variation of the longitudinal stress is no longer monotonic. Two points of inflection can be observed. As the grading index further increases to $m = 1.5$, the maximum longitudinal stress in the thick-walled sphere has shifted from its inner surface to $R/a = 2.38$. As a result, the high stress zone in the thick-walled sphere has changed to the vicinity of the outer surface. For the highest considered grading index $m = 2$, this observation becomes even more clear. The inner surface of the thick-walled sphere has become a global minimum of the longitudinal stress. For the five grading indices, the longitudinal stress values at the outer surface of the graded thick-walled sphere are all close to the applied uniaxial tension.

For comparison purpose, in Figure 3, we have also presented FE solutions for all five grading indices. The FE solutions were calculated in ABAQUS/Standard software by employing the sublayer method, in which a unidirectionally graded medium is divided into multiple homogeneous layers [Zheng et al. 2019; Liu et al. 2018; Yan et al. 2019; Yan and Mi 2019]. For brevity, the implementation details are not repeated here. It can be seen from the figure that the analytical and FE solutions agree quite well for small grading indices, validating the correctness of both methods. It is also noted that the relative error between two solutions increases with the grading index. This behavior may be attributed to three factors. First, in the FE modelings, all graded spheres were approximated with ten homogeneous sublayers. As the grading index becomes higher, the shear modulus of the graded sphere varies faster, calling for a finer FE simulation scheme. Second, among all four non-trivial components, the longitudinal stress is the most important one. The largest magnitude of latitudinal, radial and shear stresses does not exceed the applied external load, as will be presented shortly in this section. Third, for a thick-walled hollow sphere, stress concentration is most severe along its inner surface.

In Table 1, we tabulate the SCF and its appearing location for a few grading indices in the range of $0 \le m \le 2$. The rate of reduction of the SCFs as compared with that of the classical solution is also given in the table. Consistent with the stress distributions shown in Figure 3, for $m \le 1.25$, the maximum longitudinal stress always occurs at the inner surface ($R/a = 1$) of the graded thick-walled sphere and continues to decrease with the grading index. As the grading index increases to $m = 1.5$, the maximum longitudinal stress does not occur at the inner surface anymore. The location at which the maximum longitudinal stress occurs has shifted to $R/a = 2.38$ and a reduction rate of 46.8% is achieved. This value is lower than the one corresponding to the grading index $m = 1.25$. It can therefore be anticipated that an optimal grading index (m_{opt}) must exist in the interval $1.25 < m < 1.5$. For such

m	0	0.25	0.5	0.75	1	1.25	1.5	1.75	2	$m_{\text{opt}} = 1.28$
SCF	2.252	2.005	1.774	1.561	1.366	1.188	1.197	1.229	1.262	1.173
Location (R/a)	1	1	1	1	1	1	2.38	2.44	2.50	1 & 2.30
Reduction rate	0	11.0%	21.2%	30.7%	39.3%	47.2%	46.8%	45.4%	44.0%	47.9%

Table 1. The stress concentration factor and its location for a few graded thick-walled spheres under the application of a uniaxial outer tension ($b/a = 3$, $\nu = 0.3$).

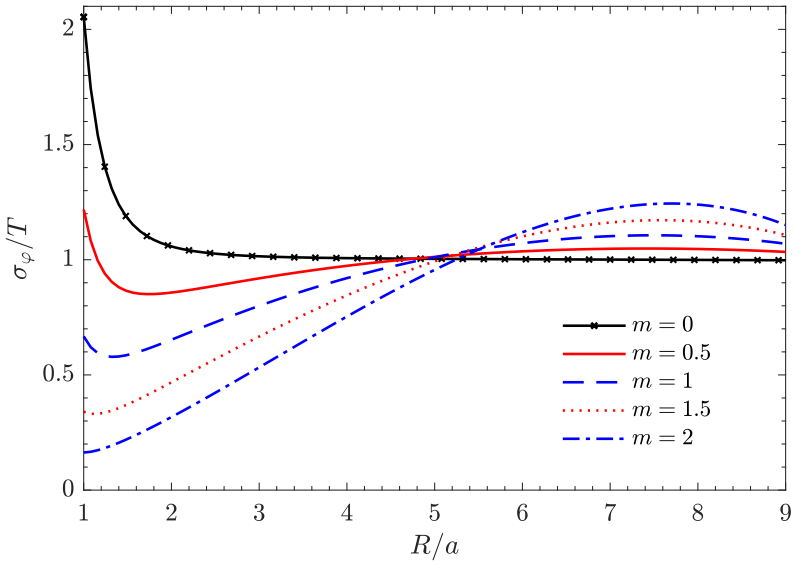

Figure 4. Variation of dimensionless longitudinal stress with radial distance for five grading indices ($b/a = 9$, $\varphi = \pi/2$).

an ideal grading index, the longitudinal stresses at the inner surface and near the outer boundary of the graded sphere become equal to each other, indicating the best longitudinal stress state along the sphere thickness. A simple numerical search reveals that the optimal grading index is $m_{\text{opt}} = 1.28$, at which the highest reduction rate (47.9%) in the maximum longitudinal stress has been achieved. In view of Figure 3, the longitudinal stress for $m_{\text{opt}} = 1.28$ should still have a nonuniform distribution. With the power-law gradation of shear modulus, it is thus impossible to achieve a completely uniformly distributed longitudinal stress. As the grading index becomes higher than the optimal value, the SCF increases again. The effects of the inhomogeneous shear modulus have therefore been weakened to a certain extent.

To investigate the influence of the radii ratio between the outer and the inner surface of the graded thick-walled sphere, we further reexamined the longitudinal stress distribution for the case of $b/a = 9$ (Figure 4). Although the overall distribution patterns are similar to those for the case of $b/a = 3$, the effects of the radii ratio is very clear. For example, when $m = 1$, the maximum longitudinal stress takes at the inner surface of the thick-walled sphere for the radii ratio $b/a = 3$. However, when $b/a = 9$, the maximum stress concentration has shifted to near the outer boundary of the sphere ($R/a = 7.48$). The reduction rate becomes 46.1%, which is higher than the one corresponding to $b/a = 3$. Consequently, for the same grading index, a larger radii ratio tends to drive the high stress zone from the inner boundary toward to the outer surface of the thick-walled sphere and results in a better SCF reduction rate. To validate this hypothesis, we further calculated the maximum longitudinal stress for a few different radii ratios.

Figure 5 shows the variation of the SCF as a function of the radii ratio within the interval $3 \le b/a \le 18$. For all five grading indices, the SCF monotonically decreases as the radii ratio of the graded sphere enlarges. For the homogeneous thick-walled sphere, the maximum longitudinal stress always occurs at its inner boundary for any radii ratio. With increased radii ratio, the SCF rapidly converges to a constant

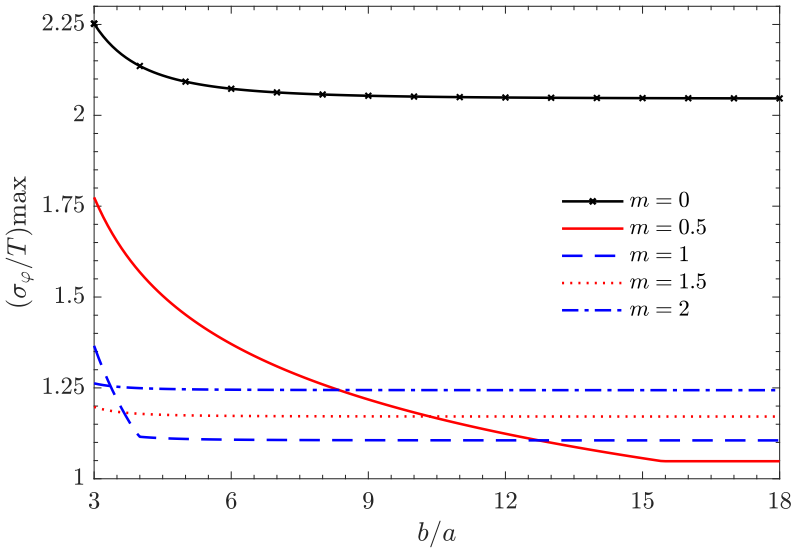

Figure 5. Variation of the maximum longitudinal stress found in the graded sphere as a function of the radii ratio b/a for five grading indices ($\varphi = \pi/2$).

(2.045) that corresponds to the SCF of an infinite hollow sphere ($\nu = 0.3$). As the shear modulus of the thick-walled sphere becomes nonuniform, the maximum longitudinal stress does not necessarily occur at its inner boundary. For the grading index $m = 0.5$ and 1, a corner in the SCF curve can clearly be found at $b/a = 15.5$ and 4.0, respectively. This behavior indicates the fact that the location of the maximum longitudinal stress has shifted from the inner boundary to near the outer surface of the graded sphere. As the grading index further increases to $m = 1.5$, the maximum longitudinal stress appears near the outer surface of the thick-walled sphere for all studied radii ratios $3 \le b/a \le 18$. As a result, the SCF curve for the grading index $m = 1.5$ becomes again very smooth. With increased radii ratio, the SCF rapidly converges to a constant. The corner no longer exists. For the largest considered grading index ($m = 2$), the SCF becomes nearly a constant and thus independent of the radii ratio.

For completeness, we also examined the distribution of the latitudinal stress in the graded thick-walled sphere. Figure 6 shows the variation of dimensionless latitudinal stress along its inner surface for the same five grading indices that have been previously considered. No severe stress concentrations were found, because the direction of the latitudinal stress is always normal to the applied uniaxial tension. Independent of the grading index, the maximum magnitude of the latitudinal stress always occurs on two poles of the inner boundary. It is clear that the maximum latitudinal stress at the inner surface continues to decrease as the grading index increases.

In analogy to Figure 3, Figure 7 shows the distribution of the latitudinal stress along the radial direction. As before, both the analytical and the FE solutions were presented. The disagreement between FE and analytical solutions also increases with the grading index. However, in contrast to the case of longitudinal stress (Figure 3), much better agreements can be found. It is noted that, for all five grading indices, the latitudinal stress climbs monotonically from the inner boundary toward to the outer surface of the thick-walled sphere. The impact of the grading index is very clear. At the inner boundary of the thick-walled

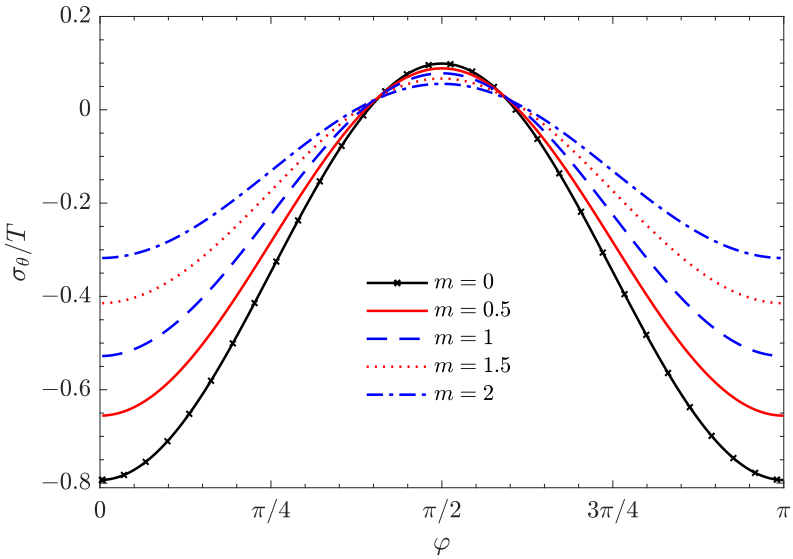

Figure 6. Variation of dimensionless latitudinal stress along the inner surface of the graded thick-walled sphere for five grading indices ($b/a = 3$, $R = a$).

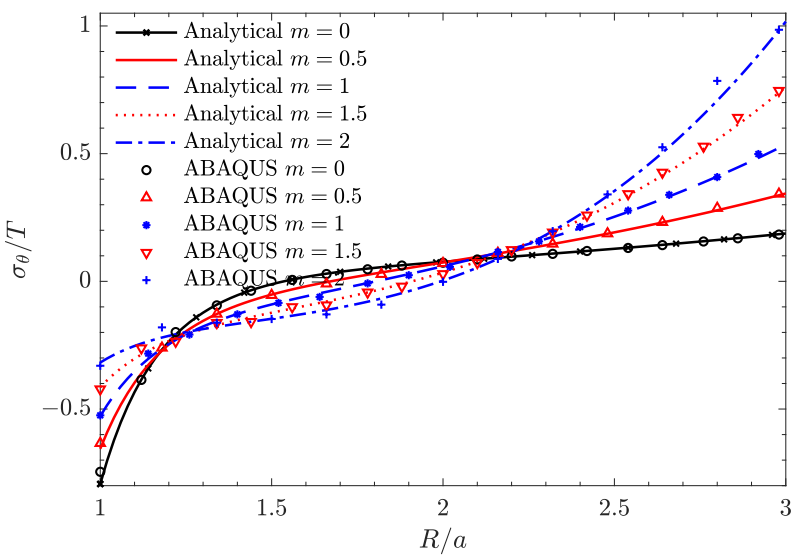

Figure 7. Variation of dimensionless latitudinal stress with radial distance for five grading indices ($b/a = 3$, $\varphi = 0$ or π).

sphere, the latitudinal stress decreases with increased grading index. At the outer surface, the opposite is true. As a balance, the intermediate grading index $m = 1$ seems to be the best choice of the five if the latitudinal stress is of the primary concern. For this particular case, $\sigma_\theta/T = -0.528$ and 0.535, respectively, at the inner and the outer surface of the thick-walled sphere.

m	0	0.25	0.5	0.75	1	1.25	1.5	1.75	2	$m_{\text{opt}} = 0.99$
$\lvert\sigma_\theta\rvert/T$	0.793	0.723	0.656	0.590	0.535	0.644	0.761	0.885	1.017	0.531
Reduction rate	0	8.9%	17.3%	25.6%	32.5%	18.8%	4.0%	−11.6%	−28.2%	33.0%

Table 2. The maximum SCF in latitudinal stress occurring at either boundary of a graded thick-walled sphere under the application of a uniaxial outer tension ($b/a = 3$, $\varphi = 0, \pi$).

Table 2 tabulates the maximum values of the latitudinal stress (in magnitude) in the graded thick-walled sphere for a few representative grading indices. For small grading indices ($m < 0.99$), the magnitude of the latitudinal stress at the inner surface is larger than that at the outer boundary. However, for $m = 0.99$, $|\sigma_\theta|/T$ at the outer boundary becomes equal to the one at the inner surface. Consistent with previous discussions, such a grading index can be defined as its optimal value (m_{opt}). For this case, the highest reduction rate (33.0%) in the maximum latitudinal stress is achieved. With the further increase of the grading index, the latitudinal stress at the outer boundary remains positive and continues to climb. As a result, the reduction rate of $|\sigma_\theta|/T$ starts to decrease. The effects of the inhomogeneous shear modulus on the reduction of latitudinal stress become nearly negligible when the grading index increases to $m = 1.5$. For $m = 2$, the latitudinal stress at the outer boundary of the sphere becomes even far larger than the classical SCF in the latitudinal stress.

Figure 8 shows the variation of the radial stress component along the symmetry axis of the mechanical model for five grading indices. In view of the uniaxial outer tension applied on the thick-walled sphere, it is along this direction ($\varphi = 0, \pi$) that the radial stress takes its maximum value. Both analytical and FE solutions are presented for all five grading indices. As can be observed from the figure, reasonable agreements between the two independent solutions are obtained for the radial stress component. This is

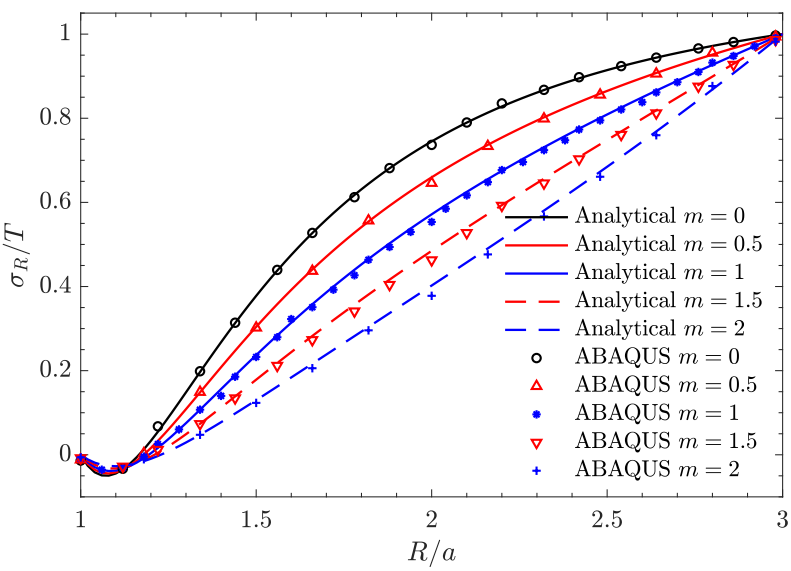

Figure 8. Variation of dimensionless radial stress with radial distance for five grading indices ($b/a = 3$, $\varphi = 0$ or π).

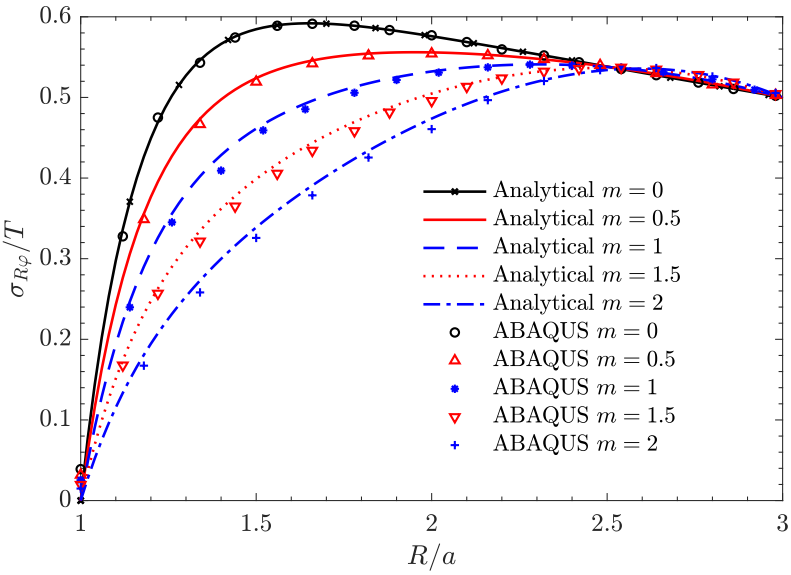

Figure 9. Variation of dimensionless shear stress with radial distance for five grading indices. ($b/a = 3, \varphi = 3\pi/4$)

true even for the largest grading index ($m = 2$), in contrast to the case of longitudinal stress. Limited by the boundary conditions $(3)_1$ and $(2)_1$, the dimensionless radial stress σ_R/T is exactly 0 and 1 at the inner and outer surfaces of the thick-walled sphere. Within the studied range of the grading index $0 \le m \le 2$, no stress concentrations in the radial stress were found. Nonetheless, the introduction of an inhomogeneous shear modulus is able to affect the distribution pattern of the radial stress. With increased grading index, the radial stress between the two boundaries of the thick-walled sphere becomes closer to a linear function of the radial coordinate.

Finally, in Figure 9, we present the variation of the shear stress component along the particular direction $\varphi = 3\pi/4$ for the same five grading indices. It is along this direction that the shear stress takes its maximum positive value. At the inner and the outer surfaces of the thick-walled sphere, the dimensionless shear stress $\sigma_{R\varphi}/T$ is exactly 0 and 0.5, respectively, as given by the boundary conditions $(3)_2$ and $(2)_2$. Similar to the case of radial stress, increasing the grading index helps to straighten the shear stress variation through the thickness dimension of the hollow sphere. As a result, the overall shear stress level becomes lower and lower than its classical counterpart. As before, although the disagreement between FE and analytical shear stresses also increases with the grading index, the discrepancy is acceptable and much less than that of the longitudinal stress.

4. Concluding remarks

In this paper, we successfully developed an analytical solution to a graded thick-walled sphere subjected to a uniaxial outer tension. While the Poisson's ratio of the sphere was fixed as a constant, its shear modulus was allowed to vary as a power-law function of the radial coordinate. The analytical solution was derived through directly tackling the equilibrium equations of displacements of the graded

thick-walled sphere. Informed by the distribution pattern of the applied uniaxial outer tension, function forms of both the radial and the longitudinal displacements were proposed in terms of three unknown functions of the radial coordinate. In this way, the two equations of equilibrium were recast into three differential equations of the Euler type involving the three fundamental unknown functions. The system of second-order differential equations were further reduced into six first-order ones by taking both the three fundamental unknown functions and their derivatives as new unknown variables. The new system is then converted into a first-order differential matrix equation and analytically solved by the joint use of the first-order differential equation theory and the eigenvalue theory. In order to validate the correctness of the derived analytical solution, finite element solution of the graded thick-walled sphere was also calculated and a reasonable agreement between the two independent methods were identified for both the stress distributions and stress concentration factors. On the basis of extensive parametric studies, a few observations and conclusions can be drawn as follows:

- In order to drive the high stress zone conventionally taking place near the inner boundary of a homogeneous thick-walled sphere, the modulus of elasticity of thick-walled spheres should be designed as an increasing function of the radial coordinate.
- In analogy to the case of a homogeneous thick-walled sphere, the longitudinal stress component remains to be the primary concern in the graded ones. No significant stress concentrations were found in latitudinal, radial and shear stresses.
- With increased shear modulus gradation, the high stress zone tends to shift from the inner surface toward to the outer boundary of thick-walled spheres. In contrast to homogeneous thick-walled spheres, for graded ones, two local stress maxima exist. As they become equal, an optimal grading index in the power-lower function of shear modulus can be defined.
- For a given grading index in the power-lower function of shear modulus, the stress concentration factor monotonically decays with increased radii ratio between the outer and the inner surface of the graded sphere and gradually converges to the factor of an infinite hollow sphere. This global maximum stress may occur either at the inner boundary or near the outer surface of the graded sphere, depending on both the radii ratio and the grading index. With increased grading index, a smaller radii ratio is required in order to shift the most sever stress concentration from the inner surface toward to the outer boundary vicinity.

Acknowledgements

This work was supported by the National Natural Science Foundation of China [grant numbers 11872149 and 11472079] and the Fundamental Research Funds for the Central Universities.

References

[Atashipour et al. 2014] S. A. Atashipour, R. Sburlati, and S. R. Atashipour, "Elastic analysis of thick-walled pressurized spherical vessels coated with functionally graded materials", *Meccanica* (*Milano*) **49**:12 (2014), 2965–2978.

[Barati and Jabbari 2015] A. R. Barati and M. Jabbari, "Two-dimensional piezothermoelastic analysis of a smart FGM hollow sphere", *Acta Mech.* **226**:7 (2015), 2195–2224.

[Barber 1992] J. R. Barber, *Elasticity*, Solid Mech. Appl. **12**, Kluwer, Dordrecht, Germany, 1992.

[Bayat and EkhteraeiToussi 2015] Y. Bayat and H. EkhteraeiToussi, "General thermo-elastic solution of radially heterogeneous, spherically isotropic rotating sphere", *J. Mech. Sci. Technol.* **29** (2015), 2427–2438.

[Birman and Byrd 2007] V. Birman and L. W. Byrd, "Modeling and analysis of functionally graded materials and structures", *Appl. Mech. Rev.* (*ASME*) **60**:5 (2007), 195–216.

[Dryden and Batra 2013] J. Dryden and R. C. Batra, "Optimum Young's modulus of a homogeneous cylinder energetically equivalent to a functionally graded cylinder", *J. Elasticity* **110**:1 (2013), 95–110.

[Evci and Gülgeç 2018] C. Evci and M. Gülgeç, "Functionally graded hollow cylinder under pressure and thermal loading: effect of material parameters on stress and temperature distributions", *Int. J. Eng. Sci.* **123** (2018), 92–108.

[Fukui and Yamanaka 1992] Y. Fukui and N. Yamanaka, "Elastic analysis for thick-walled tubes of functionally graded material subjected to internal pressure", *JSME Int. J. Solid Mech. Strength Mater.* **35**:4 (1992), 379–385.

[Ghannad 2013] M. Ghannad, "Elastic analysis of pressurized thick cylindrical shells with variable thickness made of functionally graded materials", *Compos. B Eng.* **45**:1 (2013), 388–396.

[Ghannad and Nejad 2012] M. Ghannad and M. Z. Nejad, "Complete closed-form solution for pressurized heterogeneous thick spherical shells", *Mechanika* **18**:5 (2012), 508–516.

[Ghayesh and Farajpour 2019] M. H. Ghayesh and A. Farajpour, "A review on the mechanics of functionally graded nanoscale and microscale structures", *Int. J. Eng. Sci.* **137** (2019), 8–36.

[Jabbari et al. 2013] M. Jabbari, S. Karampour, and M. R. Eslami, "Steady state thermal and mechanical stresses of a poro-piezo-FGM hollow sphere", *Meccanica* (*Milano*) **48**:3 (2013), 699–719.

[Jabbari et al. 2017] M. Jabbari, S. M. Mousavi, and M. A. Kiani, "Functionally graded hollow sphere with piezoelectric internal and external layers under asymmetric transient thermomechanical loads", *J. Press. Vessel Technol.* (*ASME*) **139**:5 (2017), art. id. 051207.

[Jin and Batra 1996] Z.-H. Jin and R. Batra, "Some basic fracture mechanics concepts in functionally graded materials", *J. Mech. Phys. Solids* **44**:8 (1996), 1221–1235.

[Kubair 2013] D. V. Kubair, "Stress concentration factors and stress-gradients due to circular holes in radially functionally graded panels subjected to anti-plane shear loading", *Acta Mech.* **224**:11 (2013), 2845–2862.

[Kubair and Bhanu-Chandar 2008] D. V. Kubair and B. Bhanu-Chandar, "Stress concentration factor due to a circular hole in functionally graded panels under uniaxial tension", *Int. J. Mech. Sci.* **50**:4 (2008), 732–742.

[Le 2017] K. C. Le, "An asymptotically exact theory of functionally graded piezoelectric shells", *Int. J. Eng. Sci.* **112** (2017), 42–62.

[Li et al. 2018] X. Li, Y. Hua, C. Zheng, and C. Mi, "Tuning stress concentrations through embedded functionally graded shells", *J. Mech. Mater. Struct.* **13**:3 (2018), 311–335.

[Liu et al. 2018] Z. Liu, J. Yan, and C. Mi, "On the receding contact between a two-layer inhomogeneous laminate and a half-plane", *Struct. Eng. Mech.* **66**:3 (2018), 329–341.

[Mohammadi et al. 2011] M. Mohammadi, J. R. Dryden, and L. Jiang, "Stress concentration around a hole in a radially inhomogeneous plate", *Int. J. Solids Struct.* **48**:3-4 (2011), 483–491.

[Nejad et al. 2016] M. Z. Nejad, M. Abedi, M. H. Lotfian, and M. Ghannad, "Exact and numerical elastic analysis for the FGM thick-walled cylindrical pressure vessels with exponentially-varying properties", *Arch. Metall. Mater.* **61**:3 (2016), 1649–1654.

[Nie and Batra 2010] G. J. Nie and R. C. Batra, "Exact solutions and material tailoring for functionally graded hollow circular cylinders", *J. Elasticity* **99**:2 (2010), 179–201.

[Poultangari et al. 2008] R. Poultangari, M. Jabbari, and M. R. Eslami, "Functionally graded hollow spheres under non-axisymmetric thermo-mechanical loads", *Int. J. Press. Vessels Pip.* **85**:5 (2008), 295–305.

[Sburlati 2013] R. Sburlati, "Stress concentration factor due to a functionally graded ring around a hole in an isotropic plate", *Int. J. Solids Struct.* **50**:22-23 (2013), 3649–3658.

[Sburlati and Cianci 2015] R. Sburlati and R. Cianci, "Interphase zone effect on the spherically symmetric elastic response of a composite material reinforced by spherical inclusions", *Int. J. Solids Struct.* **71** (2015), 91–98.

[Sburlati et al. 2014] R. Sburlati, S. R. Atashipour, and S. A. Atashipour, "Reduction of the stress concentration factor in a homogeneous panel with hole by using a functionally graded layer", *Compos. B Eng.* **61** (2014), 99–109.

[Sburlati et al. 2017] R. Sburlati, M. Kashtalyan, and R. Cianci, "Effect of graded interphase on the coefficient of thermal expansion for composites with spherical inclusions", *Int. J. Solids Struct.* **110-111** (2017), 80–88.

[Sburlati et al. 2018] R. Sburlati, R. Cianci, and M. Kashtalyan, "Hashin's bounds for elastic properties of particle-reinforced composites with graded interphase", *Int. J. Solids Struct.* **138** (2018), 224–235.

[Suresh et al. 1999] S. Suresh, M. Olsson, A. E. Giannakopoulos, N. P. Padture, and J. Jitcharoen, "Engineering the resistance to sliding-contact damage through controlled gradients in elastic properties at contact surfaces", *Acta Mater.* **47**:14 (1999), 3915–3926.

[Tutuncu 2007] N. Tutuncu, "Stresses in thick-walled FGM cylinders with exponentially-varying properties", *Eng. Struct.* **29**:9 (2007), 2032–2035.

[Tutuncu and Ozturk 2001] N. Tutuncu and M. Ozturk, "Exact solutions for stresses in functionally graded pressure vessels", *Compos. B Eng.* **32**:8 (2001), 683–686.

[Xin et al. 2014] L. Xin, G. Dui, S. Yang, and J. Zhang, "An elasticity solution for functionally graded thick-walled tube subjected to internal pressure", *Int. J. Mech. Sci.* **89** (2014), 344–349.

[Yan and Mi 2019] J. Yan and C. Mi, "A receding contact analysis for an elastic layer reinforced with a functionally graded coating and pressed against a half-plane", *J. Mech. Sci. Technol.* **33**:9 (2019), 4331–4344.

[Yan et al. 2019] J. Yan, C. Mi, and Z. Liu, "A semianalytical and finite-element solution to the unbonded contact between a frictionless layer and an FGM-coated half-plane", *Math. Mech. Solids* **24**:2 (2019), 448–464.

[Yang and Gao 2016] Q. Yang and C.-F. Gao, "Reduction of the stress concentration around an elliptic hole by using a functionally graded layer", *Acta Mech.* **227**:9 (2016), 2427–2437.

[Yang et al. 2009] Q. Yang, C.-F. Gao, and W. Chen, "Stress analysis of a functional graded material plate with a circular hole", *Arch. Appl. Mech.* **80**:8 (2009), 895–907.

[Yang et al. 2015] B. Yang, W. Q. Chen, and H. J. Ding, "3D elasticity solutions for equilibrium problems of transversely isotropic FGM plates with holes", *Acta Mech.* **226**:5 (2015), 1571–1590.

[Zheng et al. 2019] C. Zheng, X. Li, and C. Mi, "Reducing stress concentrations in unidirectionally tensioned thick-walled spheres through embedding a functionally graded reinforcement", *Int. J. Mech. Sci.* **152** (2019), 257–267.

Received 17 Jan 2020. Revised 18 Jul 2020. Accepted 12 Aug 2020.

CHENYI ZHENG: 594040623@qq.com
Jiangsu Key Laboratory of Engineering Mechanics, School of Civil Engineering, Southeast University, 2 Sipailou Street, Nanjing, 210096, China

CHANGWEN MI: mi@seu.edu.cn
Jiangsu Key Laboratory of Engineering Mechanics, School of Civil Engineering, Southeast University, 2 Sipailou Street, Nanjing, 210096, China

JOURNAL OF MECHANICS OF MATERIALS AND STRUCTURES
Vol. 15, No. 5, 2020
https://doi.org/10.2140/jomms.2020.15.605

FIELD INTENSITY FACTORS OF THREE CRACKS ORIGINATING FROM A CIRCULAR HOLE IN A THERMOELECTRIC MATERIAL

QING-NAN LIU AND SHENG-HU DING

The fracture behavior of three cracks originating from a circular hole in a thermoelectric material is studied. The basic theory of thermoelectric materials is given under the condition of the impermeable boundary of the heat flux and electric current. By introducing the conformal mapping function, the infinite plane on the physical plane is mapped into the inner unit circle on the mathematical plane. The formulas of the relevant temperature and stress fields are derived, and the analytical solutions of the complex stress functions are obtained by the complex variable function method. According to Cauchy integral formula, the analytical expressions of the electric current intensity factor and the stress intensity factor for three cracks originating from a circular hole are obtained. The effects of the hole radius and the crack lengths on the electric current intensity factor and stress intensity factors were investigated.

1. Introduction

Thermoelectric materials are functional materials that directly convert thermal energy to electric energy through the movement of a solid internal carrier. They are widely used in energy, refrigeration, microelectronics, aerospace military and other fields [Hone et al. 2013; Wu et al. 2018; Roncaglia and Ferri 2011; Wang et al. 2014; Liu et al. 2017]. Thermoelectric materials also have important applications in thermoelectric power generation [Roncaglia and Ferri 2011], such as industrial waste heat recovery and waste heat recovery systems, solid-state thermal management, solar energy collection, carbon emission reduction [Pierce and Vaudo 2010], automobile exhaust, etc.

Thermoelectric materials have become an important branch of modern functional materials [Narasimha et al. 2014; Yu et al. 2018]. However, thermoelectric materials are brittle materials. Due to the mechanical, thermal and electrical factors, cracks or microcracks will inevitably occur in the machining process [Bigoni and Movchan 2002; Xie et al. 2017; Shi 2020]. Craciun et al. [2014] studied the mode II fracture problem of an anisotropic unbounded elastic body with three collinear equal cracks. The effect of thermal load on the stress intensity factors of a finite length edge crack in an orthotropic infinite strip with finite thickness is studied by Singh et al. [2019] Therefore, the research on fracture or cracks in thermoelectric materials has important theoretical and practical significance. In recent years, some scholars have studied the theory and methods of cracks in thermoelectric materials. Using the complex function method, the two-dimensional problem of cracks in thermoelectric materials was studied in [Song et al. 2015], and the effect of a crack on the conversion efficiency of thermoelectric materials was discussed in [Song and Song 2016]. Considering the electrically and thermally impermeable crack model, Zhang and Wang

Sheng-Hu Ding is the corresponding author.
Keywords: thermoelectric material, circular hole, three cracks, complex variable function, intensity factors.

[2013] studied the crack problem in a medium possessing a coupled thermoelectric effect under thermal-electric loads. Considering the electric impermeable and heat semi-permeable crack model, the interface crack problem in a layered thermoelectric material is investigated in [Zhang and Wang 2016b]. By using the integral equation method, the thermal conductivity models of multilayer thermoelectric plates with Griffith cracks and non-collinear cracks under different loads are established in [Ding and Liu 2018; Ding and Zhou 2018]. The influence of the strip width of thermoelectric materials on the electric flux intensity factor and the heat flux intensity factor was studied. The general model of a bi-layered thermoelectric composite system with an interfacial crack is considered and the effect of interfacial cracking on the thermoelectric properties is investigated in [Wang et al. 2018]. Clin et al. [2009] studied the stress distribution of a thermocouple via numerical simulation. Turenne et al. [2010] studied the effects of the boundary conditions and the length of the thermocouple on the stress distribution of thermoelectric devices by numerical simulation. A finite element computational scheme for transient and nonlinear coupling thermoelectric fields and the associated thermal stresses in thermoelectric materials is studied in [Wang 2017].

As we all know, the holed structures play an important role in engineering. In the process of manufacturing and using a holed structure, cracks often appear around the hole [Tada et al. 1973; Ouchterlony 1976; Wu and Carlsson 1991]. In addition, when thermoelectric materials are subjected to thermal and electrical loads, the stress concentration near the hole will initiate and propagate cracks, which will lead to the failure of thermoelectric materials. Therefore, it is necessary and important to analyze the fracture behavior of thermoelectric materials, especially those with holes and cracks. For isotropic materials, the problem of multiple radial cracks originating from a circular hole using the complex variable method is studied in [Bowie 1956]. The problem of one and two cracks at the edge of an elliptic hole in an infinite isotropic material is solved using the integral transforms method from [Tweed and Melrose 1989]. Bertoldi et al. [2007] solved the problem of elliptical inclusions connected by the structural interface to an infinite matrix analytically. For the case of anisotropic materials, the solutions of the stress intensity factors of a single or two collinear edge cracks emanating from a curvilinear hole in an infinite anisotropic plane based on the boundary element method is investigated in [Liaw and Kamel 1991]. Zhang and Wang [2016a] solved the two-dimensional problem of an elliptical hole in thermoelectric materials by using the complex function method. The results show that the thermoelectric conversion efficiency can be higher than the maximum conversion efficiency of one-dimensional thermocouples at the same temperature when the current flow and heat flux are separated. The theoretical model of thermoelectric coupling for thermoelectric materials with inclined elliptical holes is established in [Wang and Wang 2017]. The effective properties of a thermoelectric material in the vicinity of an arbitrarily shaped hole are studied in [Song et al. 2019b]. The contribution of surface elasticity and electric current density on the thermal stress distribution around a circular nano-hole in a thermoelectric material is considered in [Song et al. 2019a]. Using complex variable methods, the closed-form solutions describing the corresponding thermoelastic fields in the vicinity of the nano-hole are given. Using the complex variable function method and the conformal mapping technique, the model of infinite thermoelectric material containing a circular hole with a straight crack is considered in [Pang et al. 2018]. Using the same method, Jiang et al. [2020] studied the two-dimensional problem of a circular hole with two unequal cracks in an infinite thermoelectric material under the action of uniform current and heat flux. However, the above two papers are both thermoelectric uncoupled model, which is inconsistent with the actual engineering situation. In

fact, thermoelectric material is coupled by thermal field and electric field. Therefore, considering the thermoelectric coupling effect, this paper studied the problem of three cracks at the edge of a circular hole in thermoelectric material. The effects of various parameters on current intensity factor and stress intensity factor are given.

The purpose of the present work to study the fracture problem of three cracks originating from a circular hole in a thermoelectric material under combined thermal and electrical loads. In addition, it is very interesting and challenging to obtain the analytical solutions for such complicated crack problems, since these solutions can provide the theoretical bases for fracture problems in thermoelectric materials, and can also be used as benchmark approximate methods to judge the accuracy and effciency of various numerical methods.

2. Basic equations

2.1. ***Governing equations.*** Consider an infinite thermoelectric material in which all fields are assumed to depend only on the in-plane coordinates x and y. When no free electric charge and heat source exist, the coupled transports equations of the heat and electrons in a thermoelectric material were given by [Perez-Aparicio et al. 2007]

$$\boldsymbol{J}_q = -\left(\frac{T^2\gamma\varepsilon}{e}\right)\frac{1}{T}\nabla V + (T^3\gamma\varepsilon^2 + T^2k)\nabla\frac{1}{T}, \tag{1}$$

$$\boldsymbol{J}_u = \left(\frac{T^2\gamma\varepsilon}{e}\right)\nabla\frac{1}{T} - \left(\frac{T\gamma}{e^2}\right)\frac{1}{T}\nabla V, \tag{2}$$

where $V = e\nu$, and the electric current density $\boldsymbol{J}_e$ is coupled with the heat flux $\boldsymbol{J}_q$ through the Seebeck coefficient ε. $\boldsymbol{J}_u$ is the energy flux. In the thermoelectric materials, the electric current density can be derived from the energy flux, where $\boldsymbol{J}_e = e\boldsymbol{J}_u$. In addition T, ν, γ, k are the temperature, electric potential, electrical conductivity and thermal conductivity.

It is easy to find that

$$\boldsymbol{J}_e = -\gamma\nabla\nu - \gamma\varepsilon\nabla T, \tag{3}$$

$$\boldsymbol{J}_q = -\gamma\varepsilon T\nabla\nu - (\gamma\varepsilon^2 T + k)\nabla T. \tag{4}$$

The energy flux can be expressed as

$$\boldsymbol{J}_u = \boldsymbol{J}_q + \boldsymbol{J}_e\nu. \tag{5}$$

Assuming that the energy and charge in thermoelectric materials are all conserved, the electric current density and energy flux have the form

$$\nabla\cdot\boldsymbol{J}_e = 0, \tag{6}$$

$$\nabla\cdot\boldsymbol{J}_q + \boldsymbol{J}_e\cdot\nabla\nu = 0. \tag{7}$$

2.2. ***General solution of the thermoelectric field.*** A new function F is introduced as

$$F = \nu + \varepsilon T. \tag{8}$$

Then the constitutive equations can be rewritten as

$$\boldsymbol{J}_e = -\gamma \nabla F, \tag{9}$$

$$\boldsymbol{J}_u = -\gamma F \nabla F - k \nabla T. \tag{10}$$

For the solution of two-dimensional problems in thermoelectric materials, the temperature field and electric field can be expressed by two decomposed complex functions. Substituting (9) and (10) into (6) and (7) respectively, the governing equations become

$$\nabla^2 F = 0, \tag{11}$$

$$k\nabla^2 T + \gamma (\nabla F)^2 = 0. \tag{12}$$

Following [Muskhelishvili 1975], let F be the real part of the analytic complex function $f_1(z)$, where $z = x + iy$. We get

$$F = \mathrm{Re}[f_1(z)]. \tag{13}$$

Substituting (13) into (9), we obtain

$$\begin{aligned} J_{ex} &= -\gamma \mathrm{Re}[f_1(z)]_x = -\frac{1}{2}\gamma (f_1'(z) + \overline{f_1'(z)}), \\ J_{ey} &= -\gamma \mathrm{Re}[f_1(z)]_y = -\frac{i}{2}\gamma (f_1'(z) - \overline{f_1'(z)}). \end{aligned} \tag{14}$$

or

$$J_{ex} - i J_{ey} = -\gamma f_1'(z). \tag{15}$$

From (3) and (6), we get

$$\boldsymbol{J}_e{}^2 = -\gamma k \nabla^2 T = \frac{\gamma k \nabla^2 v}{\varepsilon}. \tag{16}$$

Namely

$$\nabla^2 T = -\frac{\gamma}{k}[\nabla \mathrm{Re}[f_1(z)]]^2 = -\frac{\gamma}{k} f_1'(z)\overline{f_1'(z)}. \tag{17}$$

Considering the two-dimensional thermoelectric problem, the temperature field is superposed by two functions

$$T = T_1 + T_2, \tag{18}$$

where T_1 and T_2 satisfy

$$\nabla^2 T_1 = -\frac{\gamma}{k} f_1'(z)\overline{f_1'(z)}\,, \tag{19}$$

$$\nabla^2 T_2 = 0. \tag{20}$$

By integrating (17), we have

$$T = -\frac{\gamma}{4k} f_1(z)\overline{f_1(z)} + \mathrm{Re}[g(z)], \tag{21}$$

where $g(z)$ is an arbitrary analytic function.

From (10) and (18), the energy flux can be expressed as

$$J_{ux} - i J_{uy} = -\frac{\gamma}{2} f_1(z) f_1'(z) - k g'(z). \tag{22}$$

2.3. ***General solution of the stress field.*** For plane problems, combined with the compatibility equation, the stress function Φ satisfies

$$\nabla^4 \Phi = -\beta \nabla^2 T, \tag{23}$$

where β is a coefficient taking the value $E\alpha$ for plane stress and $E\alpha/(1-\nu)$ for plane strain, where E, ν, α are the Young's modulus, Poisson ratio and thermal expansion coefficient.

For planar two-dimensional problems, the stress function Φ is written as two complex decomposition functions,

$$\Phi(x, y) = \psi(x, y) + \psi_0(x, y), \tag{24}$$

where $\psi(x, y)$ is the special solution of the stress function, and $\psi_0(x, y)$ is the general solution of the stress function. Combining (20) and (21) with (23), we obtain

$$\psi = -\frac{\gamma \beta f_2(z) \overline{f_2(z)}}{16k}, \tag{25}$$

where $f_2'(z) = f_1(z)$.

According to the superposition principle, the stresses and displacements can be expressed as

$$\begin{aligned} \sigma_{xx} + \sigma_{yy} &= 4\mathrm{Re}[\varphi'(z)] + \frac{\mu\beta\gamma}{2k} f_1(z) \overline{f_1(z)}, \\ \sigma_{yy} - \sigma_{xx} + 2i\sigma_{xy} &= 2[\bar{z}\varphi''(z) + \phi'(z)] + \frac{\mu\beta\gamma}{2k} f_2(z) \overline{f_1'(z)}, \end{aligned} \tag{26}$$

$$2\mu[u_x + i u_y] = \kappa\varphi(z) - z\overline{\varphi'(z)} - \overline{\phi(z)} + 2\mu\alpha^* \int g(z)\, dz - \frac{\mu\beta\gamma}{4k} f_2(z) \overline{f_1(z)}, \tag{27}$$

where $\varphi(z)$ and $\phi(z)$ are complex stress functions, κ and α^* are defined as follows

$$\begin{aligned} \alpha^* &= \begin{cases} \alpha, & \text{for plane stress state} \\ (1+\upsilon)\alpha. & \text{for plane strain state} \end{cases} \\ \kappa &= \begin{cases} 3 - \upsilon \Big/ 1 + \upsilon, & \text{for plane stress state} \\ 3 - 4\upsilon. & \text{for plane strain state} \end{cases} \end{aligned} \tag{28}$$

The boundary condition of the stress in thermoelectric materials can be expressed as

$$\varphi(z) + z\overline{\varphi'(z)} + \overline{\phi(z)} = i \int (p_x + i p_y)\, ds - \frac{\mu\beta\gamma}{4k} f_2(z) \overline{f_1(z)} + \text{constant}, \tag{29}$$

where the constants p_x and p_y are the external forces exerted on the boundary, and they are assumed to be zero.

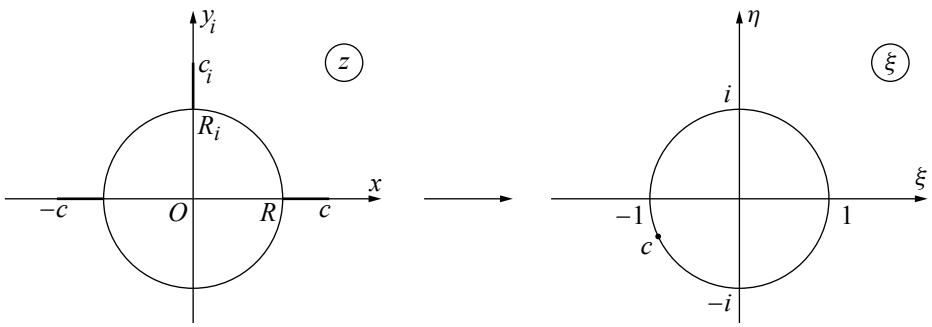

Figure 1. A circular hole with three cracks in thermoelectric material for z-plane and ξ-plane.

3. Thermoelectric field for a circular hole with three cracks

3.1. ***Formulation of problems.*** Consider a circular hole with three equal-length cracks on an infinite plane. The radius of the circle is R and the length of the crack is $c - R$. The boundary conditions on the circular hole surfaces are regarded as electrically and thermally insulated. The medium is subjected to a uniform electric current density and a uniform heat flux at infinity. Thus, the boundary conditions can be expressed as

$$\begin{cases} J_{qx} = 0,\ J_{qy} = 0, & |z| = R \ \text{ or } \ R < |x| < c \ \text{ or } \ R < |y| < c, \\ J_{ex} = 0,\ J_{ey} = 0, & |z| = R \ \text{ or } \ R < |x| < c \ \text{ or } \ R < |y| < c, \\ J_{ex} = 0,\ J_{ey} = J_{e0}, & |x| \to \infty,\ |y| \to \infty, \\ J_{ux} = 0,\ J_{uy} = J_{u0}. & |x| \to \infty,\ |y| \to \infty. \end{cases} \tag{30}$$

As shown in Figure 1, we transform the exterior of a circular hole with three cracks in the z-plane into the interior of a unit circle on the ξ-plane by introducing the conformal mapping function $z = \omega(\xi)$ by

$$z = \omega(\xi) = \frac{R}{2\xi}\left[\sqrt{-m_1\xi^2 + m_2(\xi^2+1)^2} + \sqrt{-m_1\xi^2 - 4\xi^2 + m_2(\xi^2+1)^2}\right], \tag{31}$$

where

$$m_1 = \frac{(c^2 - R^2)^2}{R^2c^2}, \quad m_2 = \frac{c^4 + R^4}{2R^2c^2}, \tag{32}$$

in which $\sqrt{-1} = \mathrm{i}$, and we take $\omega^{-1}(c) \to 1,\ \omega^{-1}(-c) \to -1,\ \omega^{-1}(ci) \to c$.

Substituting (31) into (26) and (29), we have

$$\begin{aligned} \sigma_\theta + \sigma_\rho &= 4\mathrm{Re}\left[\frac{\varphi'(\zeta)}{\omega'(\zeta)}\right] + \frac{\mu\beta\gamma}{2k} f_1(z)\overline{f_1(z)}, \\ \sigma_{yy} - \sigma_{xx} + 2i\sigma_{xy} &= 2\left[\overline{z}\left(\frac{\varphi'(\zeta)}{\omega'(\zeta)}\right)' + \frac{\phi'(\zeta)}{\omega'(\zeta)}\right] + \frac{\mu\beta\gamma}{2k} f_2(z)\overline{f_1'(z)}, \end{aligned} \tag{33}$$

$$\phi(\zeta) + \frac{w(\zeta)}{\overline{w'(\zeta)}}\overline{\phi'(\zeta)} + \overline{\varphi(\zeta)} = i\int (p_x + ip_y)\,ds - \frac{\mu\beta\gamma}{4k} f_2(\zeta)\overline{f_1(\zeta)} + \text{constant}, \tag{34}$$

where θ and ρ are the polar angle and polar radius of the polar coordinates at the crack tip of the ξ-plane.

3.2. ***Solution of the cracks.*** To solve the two-dimensional plane crack problem, the boundary conditions of the circular surfaces are electrically and thermally insulated, and the material plate is subjected to a uniform electric current density ($J_{ex} = 0,\ J_{ey} = J_{e0}$) and an energy flux ($J_{ux} = 0,\ J_{uy} = J_{u0}$) at infinity. When the potential difference and temperature difference are given, the current density and energy flux in the thermoelectric material are constantly distributed, and the heat flux is non-linear with spatial coordinates. Therefore, it is more convenient to use J_{e0} and J_{u0} to solve the far-field thermoelectric boundary conditions for circular hole problems with the boundary conditions of the electric current density and energy flux given by

$$f_1(z) - \overline{f_1(z)} = -\int J_{en}(s)\,ds + \text{constant}, \tag{35}$$

$$\operatorname{Im}\left[\frac{\gamma}{4} f_1^2(z) + \kappa g(z)\right] = -\int J_{un}(s)\,ds + \text{constant}, \tag{36}$$

where n indicates the normal direction, J_{en} and J_{un} stand for the electric current density and energy flux in the direction normal to s, respectively.

With considering the electric current impermeable cracks and the boundary conditions of the current density insulation at the edge of the hole, (35) can be rewritten as

$$f_1(z) - \overline{f_1(z)} = 0. \tag{37}$$

According to the electric current density condition at infinity, the complex function $f_1(z)$ can be expressed as

$$f_1(z) = a_1 z + f_0(z), \tag{38}$$

where a_1 is a complex constant related to the electric current density at infinity and $f_0'(\infty) = 0$.

Substituting (38) into (15), and then taking the limit $z \to \infty$ gives

$$a_1 = \frac{i J_{e0}}{\gamma}. \tag{39}$$

Substituting (31) and (39) into (37) and noting $\xi = \sigma = e^{i\theta}$ on the circular surface, we have

$$f_0(\sigma) - \overline{f_0(\sigma)} = -\frac{i J_{e0} \mathrm{R}}{2\sigma\gamma}\left[\sqrt{-4m_1\sigma^2 + 4m_2(\sigma^2+1)^2} + \sqrt{-4m_1\sigma^2 - 16\sigma^2 + 4m_2(\sigma^2+1)^2}\right]. \tag{40}$$

Multiplying both sides of (40) by $\frac{1}{2\pi \mathrm{i}} \frac{d\sigma}{\sigma - \xi}$ and carrying out the Cauchy integration yields, we obtain

$$f_0(\zeta) = -i\frac{2J_{e0}}{\gamma}\left[w(\zeta) - \frac{R\sqrt{m_2}}{\xi}\right]. \tag{41}$$

Substituting (31) and (41) into (38), we have

$$f_1(z) = -\frac{i J_{e0} R}{2\gamma\xi}\left[\sqrt{-m_1\xi^2 + m_2(\xi^2+1)^2} + \sqrt{-m_1\xi^2 - 4\xi^2 + m_2(\xi^2+1)^2} - 4\sqrt{m_2}\right]. \tag{42}$$

From (21) and (42), the function $g(z)$ related to the temperature function can be expressed as

$$g(z) = a_2 z^2 + b_2 z + g_0(z), \tag{43}$$

where a_2 and b_2 respectively represent the complex constants of the electric current density and energy flux at infinity, and $g_0'(\infty) = 0$

Substituting (42) and (43) into (22), and then taking the limit $z \to \infty$ gives

$$a_2 = \frac{{J_{e0}}^2}{4k\gamma},\ b_2 = \frac{i J_{u0}}{k}. \tag{44}$$

Substituting (42) and (44) into (36), considerating $\xi = \sigma = \mathrm{e}^{i\theta}$ on the circular surface and $J_{un} = 0$, and carrying out the Cauchy integration yields

$$g(z) = -\frac{i J_{u0} R}{2k\xi}\Big[\sqrt{-m_1\xi^2 + m_2(\xi^2+1)^2} + \sqrt{-m_1\xi^2 - 4\xi^2 + m_2(\xi^2+1)^2} - 4\sqrt{m_2}\Big]$$
$$\frac{{J_{e0}}^2 R^2}{16k\gamma}\Big[-2m_1 + 2m_2(\zeta+\zeta^{-1})^2 - 4 + \sqrt{[-m_1 + m_2(\zeta+\zeta^{-1})^2]^2 + 16m_1 - 16m_2(\zeta+\zeta^{-1})^2}\Big]. \tag{45}$$

Considering the problem of two-dimensional thermal stresses, the complex potentials $\varphi(\zeta)$ and $\phi(\zeta)$ in thermoelectric material have the form

$$\varphi(\zeta) = A_1(\zeta)\ln\zeta + \varphi_0(\zeta), \quad \phi(\zeta) = A_2(\zeta)\ln\zeta + \phi_0(\zeta), \tag{46}$$

where $A_1(\xi)$ and $A_2(\xi)$ are unknown complex functions at infinity.

Substituting (46) into (34), we obtain

$$\begin{aligned} A_1(\xi) &= R^2 m_2 A_0, \\ A_2(\xi) &= \overline{A}_1 + 2R^3 P_0\Big[\sqrt{4m_2(\xi+\xi^{-1})^2 - 4m_1} + \sqrt{4m_2(\xi+\xi^{-1})^2 - 4m_1 - 16}\Big], \end{aligned} \tag{47}$$

where

$$A_0 = -\frac{2\mu\alpha^* i J_{u0}}{k(\kappa+1)}, \quad P_0 = \frac{\mu\beta J_{e0}^2}{8k\gamma}. \tag{48}$$

By setting p_x and p_y as zero, the stress boundary condition in (34) can be rewritten as

$$\varphi(\sigma) + \frac{\omega(\sigma)}{\overline{\omega'(\sigma)}}\overline{\varphi'(\sigma)} + \overline{\phi(\sigma)} = -\frac{\mu\beta\gamma}{4k} f_2(\sigma)\overline{f_1(\sigma)}. \tag{49}$$

From (31), we have

$$\omega'(\zeta) = m_2 R(\zeta+\zeta^{-1})(1-\zeta^{-2})[(-4m_1 + 4m_2(\zeta+\zeta^{-1})^2)^{-\frac{1}{2}} + (-4m_1 + 4m_2(\zeta+\zeta^{-1})^2 - 16)^{-\frac{1}{2}}], \tag{50}$$

which leads to the following expression for $M = \omega(\xi)/\overline{\omega'(\xi)}$:

$$M = \frac{R}{4\xi}\frac{\sqrt{4m_2(\xi^2+1)^2 - 4m_1\xi^2} + \sqrt{4m_2(\xi^2+1)^2 - 4m_1\xi^2 - 16\xi^2}}{m_2 R(\xi+\xi^{-1})(1-\xi^2)\Big[(4m_2(\xi+\xi^{-1})^2 - 4m_1)^{-\frac{1}{2}} + (4m_2(\xi+\xi^{-1})^2 - 4m_1 - 16)^{-\frac{1}{2}}\Big]} \tag{51}$$

It can be deduced that $\omega'(\xi)$ and $\frac{w(\zeta)}{\overline{w'(\zeta)}}\overline{\varphi_0'(\zeta)}$ are analytically outside the unit circle and can be extended to an analytic function on the circle. Then using of the Cauchy integral at infinity leads to

$$\frac{1}{2\pi i}\int_\sigma \frac{w(\sigma)}{\overline{w'(\sigma)}}\frac{\overline{\varphi_0'(\sigma)}}{\sigma - \zeta}d\sigma = 0. \tag{52}$$

Note that on the circular surface, we have $\xi = \sigma = e^{i\theta}$. Then, substituting (51) and (52) into (49) and carrying out the Cauchy integration yields

$$\varphi_0(\xi) = \frac{R^2 m_2 \overline{A}_0}{\zeta}, \quad \phi_0(\xi) = (8R^3 p_0 \sqrt{m_2} + R^2 m_2 \overline{A}_0)\zeta^{-1}. \tag{53}$$

From (46) and (53), $\varphi(\zeta)$ and $\phi(\zeta)$ can be expressed as

$$\varphi(\xi) = m_2 R^3 p_0 \zeta \big[4\sqrt{m_2}\zeta^{-1} - 8\sqrt{m_2}(\zeta^2 + \zeta^{-2}) + \sqrt{-4m_1\zeta^2 + 4m_2(\zeta^2+1)^2} + \sqrt{-4m_1\zeta^2 - 16\zeta^2 + 4m_2(\zeta^2+1)^2}\big], \tag{54}$$

$$\phi(\zeta) = m_2 R^3 p_0 \zeta \big[\sqrt{-4m_1\zeta^2 + 4m_2(\zeta^2+1)^2} + 4\sqrt{m_2}(\zeta^{-1} - 2\zeta^{-4} - 2) + \sqrt{-4m_1\zeta^2 - 16\zeta^2 + 4m_2(\zeta^2+1)^2}\big] - \overline{M_2}\varphi_0'(\zeta). \tag{55}$$

For the problem of hole edge cracks, the current intensity factors at the crack tip c are defined as

$$\begin{aligned} K_e = K_{ex} - iK_{ey} &= \lim_{z\to R+c} \sqrt{2\pi(z - R - c)}(J_{ex} - iJ_{ey}) \\ &= -\gamma \lim_{\xi\to 1} \sqrt{2\pi[\omega(\xi) - \omega(1)]}\frac{f_1'(\xi)}{\omega'(\xi)}. \end{aligned} \tag{56}$$

Substituting (42) and (54) into (56), we have

$$K_e = K_{ex} - iK_{ey} = i\sqrt{\pi R}\sqrt{\frac{c^4 + R^4}{Rc}}\, j_{e0}. \tag{57}$$

For the problem of hole edge cracks, the stress intensity factor at the crack tip c can be expressed as

$$K_I - iK_{II} = \lim_{z\to R+c} 2\sqrt{2\pi(\omega(\xi) - R - c)}\varphi'(z) = \lim_{\xi\to 1} 2\sqrt{2\pi(\omega(\xi) - \omega(1))}\frac{\varphi'(\xi)}{\omega'(\xi)}. \tag{58}$$

Substituting (50) and (54) into (58), we have

$$K_I = \frac{m_2 R^3 \mu\beta J_{e0}^2}{8k\gamma}\sqrt{\frac{\pi}{c}}\left(\frac{16m_2 - 2m_1}{\sqrt{16m_2 - 4m_1}} + \frac{16m_2 - 2m_1 - 8}{\sqrt{16m_2 - 4m_1 - 16}} - 8\sqrt{m_2}\right)., \tag{59}$$

$$K_{II} = \frac{\mu\alpha^* J_{u0}}{k(\kappa+1)}\sqrt{\frac{\pi}{c}}\frac{c^4 + R^4}{c^2}. \tag{60}$$

Under limiting conditions, the new configuration can be simulated from the present result. If the length of crack c-R tends to zero, using (42), (15) reduces to

$$J_{ex} - \mathrm{i}J_{ey} = \mathrm{i}J_{e0}\frac{1 + \bar{\xi}^2}{\bar{\xi}\xi^{-2}} \tag{60}$$

which is the result for an infinite thermoelectric material containing only a circular hole [Zhang and Wang 2016a].

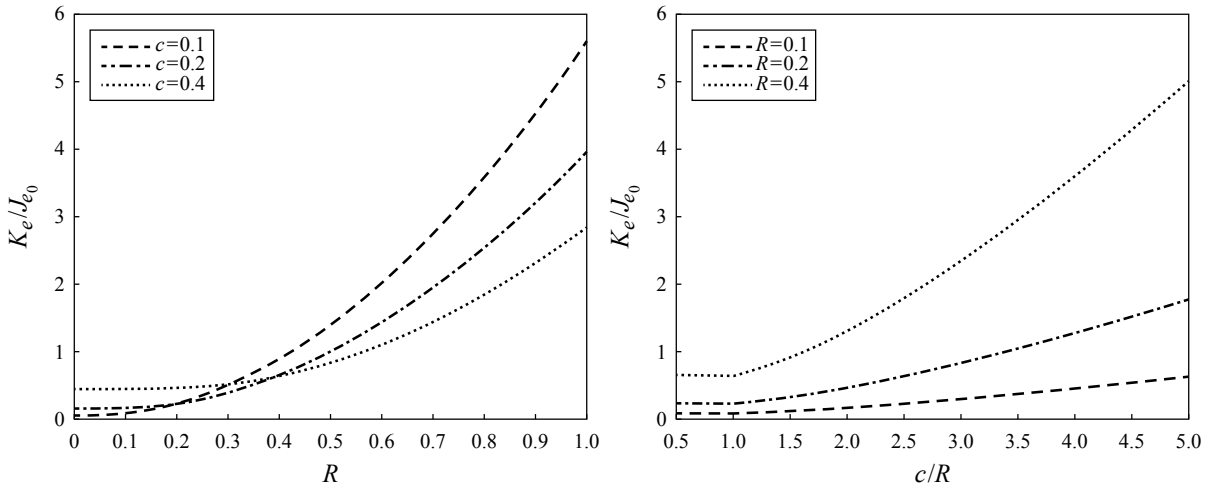

Figure 2. Variation of the electric intensity factor K_e with R (left) and c/R (right).

4. Numerical examples

When an infinite thermoelectric plate with three cracks originating from circular hole is subjected to a uniform current at infinity, the electric intensity factor at the crack tip c is shown in Figure 2. From (57), it can be seen that the electric intensity factor is related not only to the radius R of the circle, but also to the length c/R of the crack. When the radius of the circular hole is larger and other conditions remain unchanged, the electric intensity factor K_e at the crack tip increases as R increases, and the change speed becomes faster as R increases. When R is a constant value, the electric intensity factor K_e at the crack tip increases with an increase of c/R, and the change speed becomes faster as R increases. Figure 3 shows the variation of the stress intensity factor K_I at the crack tip c with parameters R/c and R. It can be found that when the orifice radius is constant, c/R increases as the value of K_I increases. When R/c is a fixed

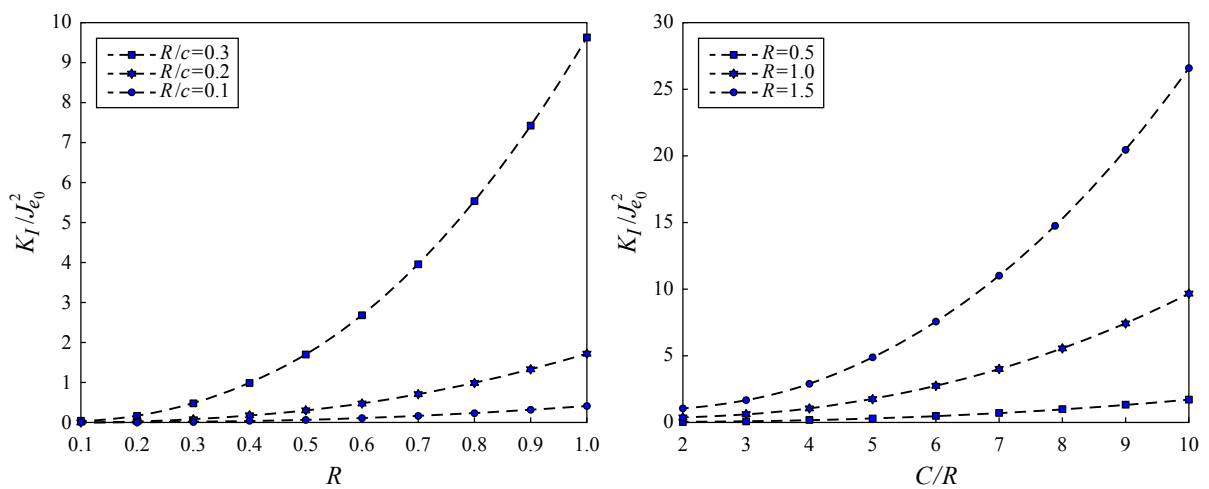

Figure 3. Variation of the stress intensity factor K_I with R (left) and c/R (right).

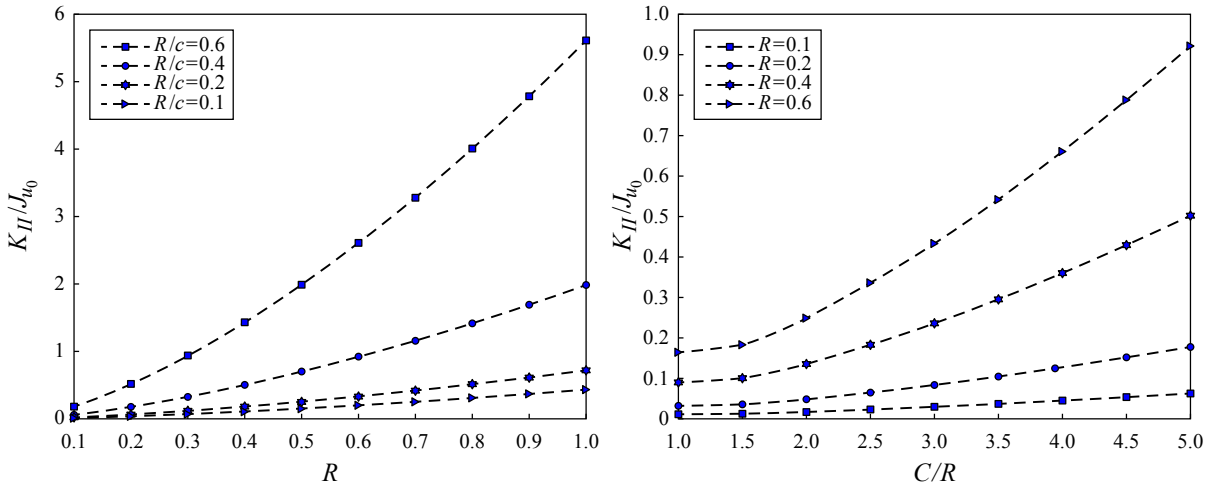

Figure 4. Variation of the stress intensity factor K_{II} with R (left) and c/R (right).

value, the stress intensity factor at the crack tip c increases as the aperture radius increases. When R/c is larger, the rate of K_I increases faster. Figure 4 shows the variation of the stress intensity factor K_{II} with parameters R/c and R. When the radius of the circular hole is larger and the other conditions remain unchanged, the stress intensity factor K_{II} at the crack tip c increases as R increases and the change speed becomes faster with an increase of R/c value. When R is a constant value, the stress intensity factor K_{II} at the crack tip c increases with the increase of c/R, and the change speed becomes faster as c/R increases.

5. Conclusions

Based on the general form of the temperature field and stress field in thermoelectric materials, the explicit solutions of the electric current density and heat flux are obtained by using the complex function method. A more practical case, thermoelectric coupling is considered in this paper. To solve the problem of a circular hole with three cracks, the boundary conditions and conformal mapping were used to map the outer part of the z-plane circular hole to the inner part of the ξ-plane unit circle. The influences of the radius of the hole and the length of the cracks on the electric intensity factor and the stress intensity factor are studied under the condition that the thermoelectric material plate is insulated only by the electric current at infinity.

Acknowledgements

Financial support from the National Natural Science Foundation of China (grants 11762016, 11762017 and 11832014) and the Natural Science Foundation of Ningxia (grant 2020AAC03057) are gratefully acknowledged.

References

[Bertoldi et al. 2007] K. Bertoldi, D. Bigoni, and W. Drugan, "Structural interfaces in linear elasticity, I: Nonlocality and gradient approximations", *J. Mech. Phys. Solids* **55**:1 (2007), 1–34.

[Bigoni and Movchan 2002] D. Bigoni and A. B. Movchan, "Statics and dynamics of structural interfaces in elasticity", *Int. J. Solids Struct.* **39** (2002), 4843–4865.

[Bowie 1956] O. L. Bowie, "Analysis of an infinite plate containing radial cracks originating from the boundary of an internal circular hole", *J. Math. Phys.* (*MIT*) **35** (1956), 60–71.

[Clin et al. 2009] T. Clin, S. Turenne, and D. Vasilevskiy, "Numerical simulation of the thermomechanical behavior of extruded bismuth telluride alloy module", *J. Electro. Mater.* **38**:7 (2009), 994–1001.

[Craciun et al. 2014] E. M. Craciun, T. Sadowski, and A. Răbâea, "Stress concentration in an anisotropic body with three equal collinear cracks in mode II of fracture, I: Analytical study", *Z. Angew. Math. Mech.* **94**:9 (2014), 721–729.

[Ding and Liu 2018] S. H. Ding and Q. N. Liu, "A multi-layered model for heat conduction analysis of thermoelectric material strip", *Comput. Model. Eng. Sci.* **114** (2018), 335–349.

[Ding and Zhou 2018] S. H. Ding and Y. Zhou, "Heat conduction in multilayered thermoelectric materials with multiple cracks", *Acta Mech. Solida Sin.* **4** (2018), 512–522.

[Hone et al. 2013] J. Hone, I. Ellwood, and M. Muno, "Thermoelectric power of single-walled carbon nanotubes", *Phys. Rev. Lett.* **13**:80 (2013), 1335–1338.

[Jiang et al. 2020] D. D. Jiang, Q. H. Luo, W. Liu, and Y. T. Zhou, "Thermoelectric field disturbed by two unequal cracks adjacent to a hole in thermoelectric materials", *Eng. Fract. Mech.* **235** (2020), art. id. 107163.

[Liaw and Kamel 1991] B. M. Liaw and M. Kamel, "A crack approaching a curvilinear hole in an anisotropic plane under general loadings", *Eng. Fract. Mech.* **1** (1991), 25–35.

[Liu et al. 2017] T. Liu, T. Wang, and W. Luan, "Optimal number of thermoelectric couples in a heat pipe assisted thermoelectric generator for waste heat recovery", *J. Electro. Mater.* **46**:5 (2017), 3137–3144.

[Muskhelishvili 1975] N. L. Muskhelishvili, *Some basic problems of mathematical theory of elasticity*, Noordhoff, Leyden, 1975.

[Narasimha et al. 2014] S. Narasimha, P. Taylor, and D. Nemir, "Shockwave consolidation of nanostructured thermoelectric materials", pp. art. id. 92260J in *Nanophotonics and macrophotonics for space environments VIII*, Proc. SPIE **9226**, 2014.

[Ouchterlony 1976] F. Ouchterlony, "Stress intensity factors for the expansion loaded star crack", *Eng. Fract. Mech.* **8** (1976), 447–448.

[Pang et al. 2018] S. J. Pang, Y. T. Zhou, and F. J. Li, "Analytic solutions of thermoelectric materials containing a circular hole with a straight crack", *Int. J. Mech. Sci.* **144** (2018), 731–8.

[Perez-Aparicio et al. 2007] J. L. Perez-Aparicio, R. L. Taylor, and D. Gavela, "Finite element analysis of nonlinear fully coupled thermoelectric materials", *Comput. Mech.* **40**:1 (2007), 35–45.

[Pierce and Vaudo 2010] J. Pierce and R. P. Vaudo, "Methods of depositing epitaxial thermoelectric films having reduced crack and/or surface defect densities and related devices", US patent 7804019 B2, 2010, Available at http://patentscope.wipo.int/search/en/detail.jsf?docId=WO2008097484.

[Roncaglia and Ferri 2011] A. Roncaglia and M. Ferri, "Thermoelectric materials in MEMS and NEMS: a review", *Sci. Adv. Mater.* **3**:3 (2011), 401–419.

[Shi 2020] P. P. Shi, "Singular integral equation method for 2D fracture analysis of orthotropic solids containing doubly periodic strip-like cracks on rectangular lattice arrays under longitudinal shear loading", *Appl. Math. Model.* **77**:2 (2020), 1460–1473.

[Singh et al. 2019] A. Singh, S. Das, and E. M. Craciun, "Effect of thermomechanical loading on an edge crack of finite length in an infinite orthotropic strip", *Mech. Compos. Mater.* **55**:3 (2019), 285–296.

[Song and Song 2016] H. P. Song and K. Song, "Electric and heat conductions across a crack in a thermoelectric material", *J. Theor. Appl. Mech.* (*Warsaw*) **46**:1 (2016), 83–98.

[Song et al. 2015] H. P. Song, C. F. Gao, and J. Y. Li, "Two dimensional problem of a crack in thermoelectric materials", *J. Therm. Stresses* **38**:3 (2015), 325–337.

[Song et al. 2019a] K. Song, H. P. Song, P. Schiavone, et al., "The effects of surface elasticity on the thermal stress around a circular nano-hole in a thermoelectric material", *Math. Mech. Solids* **24** (2019), 3156–3166.

[Song et al. 2019b] K. Song, H. P. Song, P. Schiavone, et al., "The influence of an arbitrarily shaped hole on the effective properties of a thermoelectric material", *Acta Mech.* **230** (2019), 3693–3702.

[Tada et al. 1973] H. Tada, P. C. Paris, and G. R. Irwin, *The stress analysis of cracks handbook*, Del Research, Hellertown, PA, 1973.

[Turenne et al. 2010] S. Turenne, T. H. Clin, and D. Vasilevskiy, "Finite element thermomechanicial modeling of large area thermoelectric generators based on bismuth telluride alloys", *J. Electro. Mater.* **39** (2010), 1926–1933.

[Tweed and Melrose 1989] J. Tweed and G. Melrose, "Cracks at the edge of an elliptic hole in out of plane shear", *Eng. Fract. Mech.* **3** (1989), 743–747.

[Wang 2017] B. L. Wang, "A finite element computational scheme for transient and nonlinear coupling thermoelectric fields and the associated thermal stresses in thermoelectric materials", *Appl. Thermal Engng.* **110** (2017), 136–143.

[Wang and Wang 2017] P. Wang and B. L. Wang, "Thermoelectric fields and associated thermal stresses for an inclined elliptic hole in thermoelectric materials", *Int. J. Eng. Sci.* **119** (2017), 93–108.

[Wang et al. 2014] T. Wang, W. Luan, and W. Wang, "Waste heat recovery through plate heat exchanger based thermoelectric generator system", *App. Energy* **136** (2014), 860–865.

[Wang et al. 2018] P. Wang, K. F. Wang, and B. L. Wang, "Effective thermoelectric conversion properties of thermoelectric composites containing a crack/hole", *Compos. Struct.* **191** (2018), 180–189.

[Wu and Carlsson 1991] X. R. Wu and A. J. Carlsson, *Weight functions and stress intensity factor solutions*, Pergamon, New York, 1991.

[Wu et al. 2018] Y. Wu, H. Zhang, and L. Zuo, "Thermoelectric energy harvesting for the gas turbine sensing and monitoring system", *Energy Conv. Manag.* **157** (2018), 215–223.

[Xie et al. 2017] S. Xie, D. Chen, and M. Gao, "Fracture regularity of thin plate model of main roof with elastic foundation boundary for backfill mining", *J. China Coal Soc.* **42**:9 (2017), 2270–2279.

[Yu et al. 2018] J. Yu, K. Xia, and X. Zhao, "High performance p-type half-Heusler thermoelectric materials", *J. Phys. D Appl. Phys.* **51**:11 (2018), 113001.

[Zhang and Wang 2013] A. B. Zhang and B. L. Wang, "Crack tip field in thermoelectric media", *Theor. Appl. Fract. Mech.* **66**:16 (2013), 33–36.

[Zhang and Wang 2016a] A. B. Zhang and B. L. Wang, "Explicit solutions of an elliptic hole or a crack problem in thermoelectric materials", *Eng. Fract. Mech.* **151** (2016), 11–21.

[Zhang and Wang 2016b] A. B. Zhang and B. L. Wang, "Temperature and electric potential fields of an interface crack in a layered thermoelectric or metal/thermoelectric material", *Int. J. Therm. Sci.* **104** (2016), 396–403.

Received 3 Jul 2020. Revised 10 Aug 2020. Accepted 16 Aug 2020.

QING-NAN LIU: 384831828@qq.com
School of Mathematics and Statistics, Ningxia University, Yinchuan, 750021, China

SHENG-HU DING: dshnx2019@nxu.edu.cn
School of Mathematics and Statistics, Ningxia University, Yinchuan, 750021, China

JOURNAL OF MECHANICS OF MATERIALS AND STRUCTURES
Vol. 15, No. 5, 2020
https://doi.org/10.2140/jomms.2020.15.619

EXPERIMENTAL STUDY OF DEFORMATION PROCESSES IN LARGE-SCALE CONCRETE STRUCTURES UNDER QUASISTATIC LOADING

IGOR SHARDAKOV, IRINA GLOT, ALEKSEY SHESTAKOV,
ROMAN TSVETKOV, VALERIY YEPIN AND GEORGIY GUSEV

Physical experiments with large-scale models of engineering structures provide invaluable information for understanding the deformation processes in objects of complex configuration and allow researchers to reproduce the interactions between the structural elements on different scales. The article presents test stand designed and assembled at the Institute of Continuum Media Mechanics (Perm, Russia). Using this stand, studies of deformation processes in a large-scale model concrete structure were carried out. The deformation response of structural elements to the locally applied quasistatic and impulse loads was studied. The patterns of the spatial-temporal distribution of deformation parameters over the structural elements were obtained. The tests conducted in the elastic deformation mode allowed to obtain the vibration portrait of the structure, which provided basic information for the future experiments aimed at studying inelastic deformation of the structure until its ultimate failure.

1. Introduction

The assessment of the stress-strain state of large engineering constructions and complex structures is of great importance. This issue arises at the stages of construction and operation of buildings, as well as at the stage of evaluation of risks associated with the occurrence of emergency situations. Estimating the stress-strain state in complex and large-sized buildings and engineering structures is based on a combination of experimental and theoretical approaches. The theoretical approaches involve the creating of a mathematical model of the examined structure and determination of principal regularities of its behavior using for this purpose the classic analytical and numerical simulation methods in the framework of elastic and non-elastic models. Today, the numerical implementation of these models is possible due to the application of a number of well-developed universal software systems for finite element analysis, such as ANSYS, ABAQUS, NASTRAN, COMSOL, LIRA-CAD. As a rule, such software packages offer a wide scope of options for describing the composition of the object and taking into account the interactions between structural elements. They involve various models to simulate the physical and mechanical properties of materials used in the structure. However, the development of a mathematical model of the structure composed of many elements of different size necessitates the simplification of its properties and the neglect of structural details beginning from a certain scale. Such a model is not always appropriate for displaying the whole variety of processes, which occur on different scales and can provoke the structure failure. In addition, the problem of furnishing such mathematical models with material parameters is not as simple as might appear at the first sight. Information about the physical and mechanical properties of materials obtained from the standard tests, which usually realize simple

Keywords: large-scale testing, concrete structure, deformation monitoring, vibration diagnostics, strength, fracture.

stress-strain state, is often insufficient for describing the state of a real structure. Therefore, an important stage in numerical simulation is a reliable verification of the mathematical model by means of comparing its predictions with the results of experiments simulating the deformation processes in real structures to the maximum possible accuracy.

Experimental approaches to the assessment of the stress-strain state of large structures are based on the monitoring of the behavior of real structures under real operating conditions, or examining the behavior of model structures subjected to loads reproducing to a certain extent the action of real loads. A review of experimental methods for studying large structures is given in [16; 22].

Traditionally, mechanical tests of complex large-sized structures conducted at the stages of their construction and operation with the aim to determine the actual bearing capacity, rigidity and crack resistance of structures, as well as to estimate the possibility of their future operation. Often, such tests are carried out to study the ways to strengthen the structure and assess the possibility of extending its life. Such tests are generally performed under conditions of elastic deformation, which does not allow the occurrence of irreversible strain states of the object [17; 14]. Some experiments are known on loading real structures to their complete destruction [31; 23]. However, for such studies, special conditions are required associated with the search for the test structure, the organization of the necessary loading system, the technology for recording experimental data in the field, etc.

Modeling of the deformation behavior of large structures in laboratory conditions makes it possible to study the impact of a wide variety of experimental loads. During the experiments the changes in the stress-strain state of model structure are under control and it is possible to register many different parameters of the structure. Modern test stands provide ample opportunities for conducting experiments, which can simulate not only elastic, but also inelastic deformation of examined object, the initiation and evolution of damages, and ultimate failure of the structure [19; 27].

Conducting large-sized structure tests is a complex and expensive procedure, which requires large material costs, special equipment and highly qualified specialists. However, in the past few years interest in such tests has quickened due to the fact that large-scale modeling allows realistic representation of physic-mechanical properties of structure materials and ensemble interactions of all dissimilar and different-scale elements of the structure. This is especially important due to the widespread use of new materials and technologies in engineering and construction. Large-scale experiments provide valuable information for interpreting the mechanical behavior of structures made of heterogeneous materials. They provide required data for the verification of mathematical models of deformation processes in complex structures. Furthermore, keen interest in such tests is generated by a rapid development of experimental devices for recording, gathering and processing of information, which allow one to study the behavior of the investigated objects with a desired accuracy. An analysis of resent publications indicates that large-scale modeling is actively progressing field of research.

Specialized stands for conducting large-scale structure experiments are unique structures in themselves. The experimental laboratories of this kind are generally organized on the principle of universality to allow studying structures made of various materials and reproducing a wide range of operating loads. Large test centers usually hold several types of strong floors and reaction walls, vibration platforms and shake tables with different degrees of freedom, and also contain a variety of devices for performing both the primary and secondary structure tests. The size and shape of these testing units are specified depending on the purpose of a test laboratory. Such laboratories often comprise the structural units of large industrial

corporations [30; 6; 9]. Therefore, as a rule, such research centers limit their interests to a certain class of objects and a certain range of impacts.

In the construction industry, the most-in demand area of experimental research is related to seismic impacts on buildings and engineering structures. Now, there are a number of world-class research centers with unique facilities, which simulate seismic impacts on the structure [26; 20; 11; 5; 25]. The studies conducted at these centers are mainly concerned with observation of the movement of structural elements under conditions of high amplitude dynamic loads, the analysis of the crack formation and propagation, and recording of scenarios of damage accumulation and failure [29; 8]. The focus of research is both on the behavior of load bearing structures and on the objects inside buildings, as well as the study of the ways to protect structures from seismic loads. Among the subjects of research are the structures of steel [21], concrete [18; 34] wood, large-scale fragments of low-rise and high-rise buildings [4; 15], fragments of bridges [12; 2], power transmission line supports and other engineering structures. The information obtained is used to solve the problems of seismic resistance of existing and newly constructed structures.

Information about the experimental studies of large-scale buildings and engineering structures under the action of static or slowly changing external loads is found less frequently in scientific publications. Such processes occur in structures under the action of operational loads, as well as due to changes in the state of foundations caused by karst effects, freezing of soils, and various technogenic processes in the surrounding soil massif. Laboratory tests of full-size reinforced concrete fragments under static and quasi-static loads are described in [7; 13]. Bench tests simulating the interaction of large-scale models of engineering structures with subgrade soil are reviewed in [1; 24; 33; 32]. The focus of those works is on the observed scenarios of damage evolution, detection of the most vulnerable structural elements and ascertaining whether the deformation state of the structure complies with building codes.

However, such issues as the early diagnosis of structural damage, the search for damage precursor, and the assessment of workability of structures with a certain level of accumulated damage should be investigated further. Information obtained during these studies is essential for the development of effective automated deformation monitoring systems. A desire to solve these problems has motivated researchers of the Institute of Continuous Media Mechanics of the Russian Academy of Sciences (Perm, Russia) to construct a large-scale test stand intended for studying the deformation processes in complex building and engineering structures.

Unlike most of the known experimental facilities of this kind, our stand was designed and created as a tool for exploratory research. It has great variability in the formulation of research tasks, the choice of research methods and registration tools. Our goal is to obtain fundamental knowledge about regularities of deformation processes, search for precursors of fracture, development of the methods for recording the early signs of failure in structures of various configurations and from different materials. Based on these tasks, it is very important to plan and correctly design the configuration of the power elements of the stand, providing the possibility of varying the external loads by type and value. An important point is the design of measuring and recording systems. It should be easily reconfigurable in accordance with the objectives of the study and the type of test structure. This paper provides information about the design of the stand, its equipment and capabilities.

Currently, a large cycle of experiments has developed and started at our stand. It aims to examine the behavior of a reinforced concrete structure under static and dynamic loading. We are going to study the spatial-temporal distribution of the deformation response of load-bearing elements to the onset of

critical processes, as well as to find and register damage precursors. In the experiment, such processes as contact interaction of structural parts, binding of structural elements due to steel reinforcement, real material composition, etc., are reproduced. These experiments provide the grounds for the development of automated deformation monitoring systems, which make it possible to control the current state of the observed structure and predict the development of critical processes in it. This paper presents the first results of the experiments simulating the deformation response of structural elements to the local quasi-static and impulse loads.

2. An experimental stand for mechanical testing of large-scale structures

The experimental stand of the Institute of Continuous Media Mechanics is a universal test site designed for mechanical testing of large-scale structures of various kinds. It is fitted with advanced equipment capable of applying various types of dynamic and static loads, and monitoring the observation of deformation processes in a wide range of execution times. The stand's equipment allows a variety of experiments, simulating the differential settlement of building foundation and impact of local static, vibrational and pulsed loads on various parts of model structure. The stand allows the observation of the structure through all stages of the deformation process including the elastic-to-inelastic transition. It allows researchers to observe the nucleation and evolution of damages, the failure of individual parts of the structure and, finally, the complete destruction of the specimen.

The main load-bearing elements of the stand are four load frames, combined by the horizontal and vertical connecting elements. The usable volume inside the frames is $8 \times 12 \times 8$ m (Figure 1). The load frames are based on a concrete foundation of 3 m depth. The design force, which can be realized within each loading frame, is 1000 kN. The stand is equipped with a beam crane, as well as supplementary devices and units, which provide assembling and loading of the model structure, registration, collection and processing of experimental data.

Differential settlement of building foundation is simulated using a specially designed jack system. It provides displacements of the base of each column using hydraulic jacks with the ability of fine adjustment. The jack control system ensures kinematic and force impacts on the structure in automatic mode according to the specified time dependencies. This makes it possible to realize different column settlement scenarios. The stand provides a vast variety of tools for realization of quasi-static loads.

The deformation response of the model structure to external loads is recorded using several recording systems. The stand is equipped with various types of sensors, which can register deformation processes with characteristic times ranging from 10 microseconds to several years. The lower boundary of this range corresponds to the acoustic emission signals. The registration of these signals is carried out with the aid of the original system developed by the team of co-authors. It provides the online, 8-channel registration of acoustic vibrograms with the accuracy comparable to the accuracy of the world-known brands of devices. The developed system has the advantages of easy increase of the number of channels and sensors, low cost, easy integration with well-known software products for processing primary data of acoustic vibrograms. Deformation processes with characteristic times of 0.1 ms are recorded using the system of 30 single-component vibration sensors (accelerometers). The physical and program-based integration of the sensors allows its synchronization and controlling the registration modes of the initial vibrograms. Dynamic deformation processes with characteristic times from 2 ms to 2.5 s are recorded

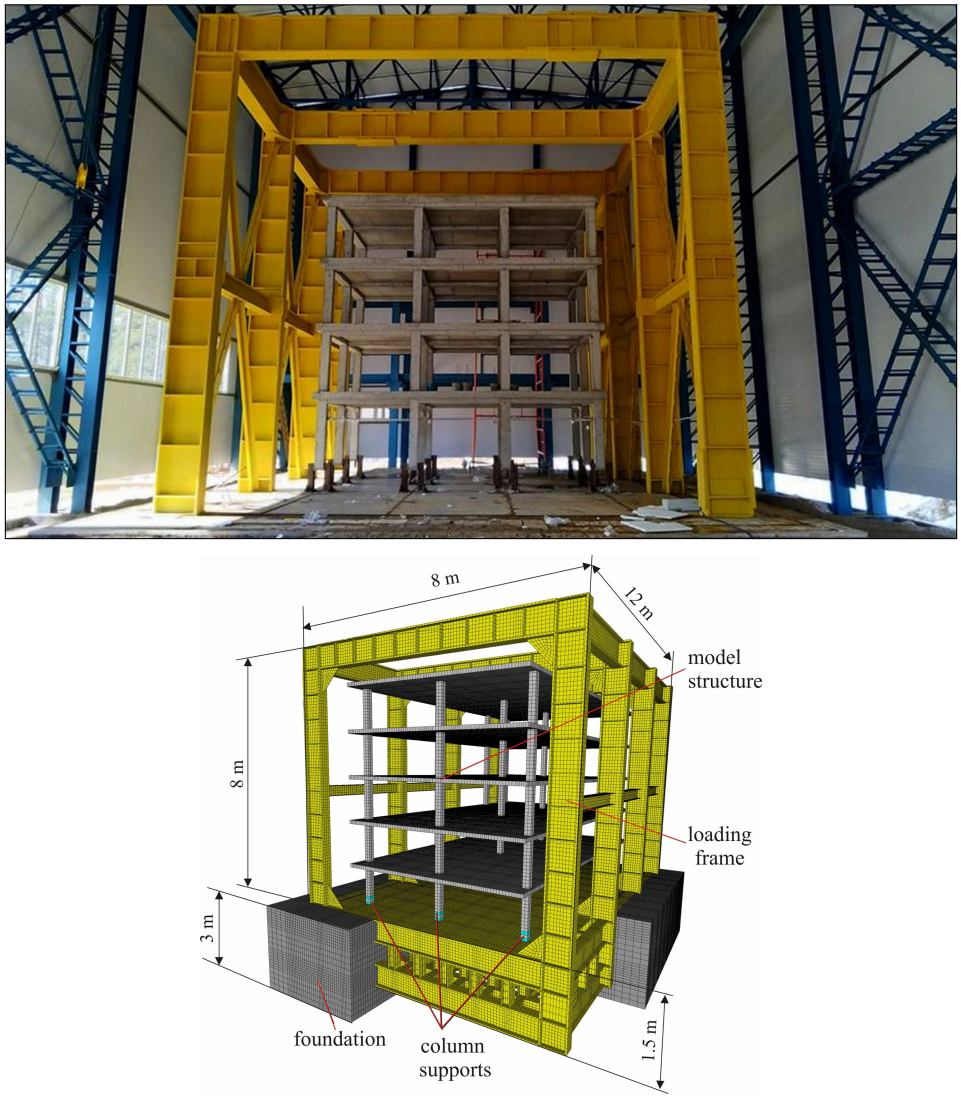

Figure 1. Test stand with installed model concrete structure: photo and schematic diagram.

by six 3-component seismic sensors.

The deformation response of the structural elements to a given local quasistatic load is measured by a system of 57 strain gauges and fiber-optic sensors integrated with the recording equipment. Registration of vertical displacements of the column bases is carried out by the system of hydraulic leveling sensors and the system of automatic data recording with web cameras [3].

In order to evaluate in practice the operability and functionality of the stand and the accompanying systems, an experiment was developed to study the deformation behavior of a model concrete structure subjected to quasi-static load. The experimental sample is a fragment of a precast-monolithic building on a scale of 1:2, including 24 standard cells combined into a 4-story structure (Figure 1). The dimensions

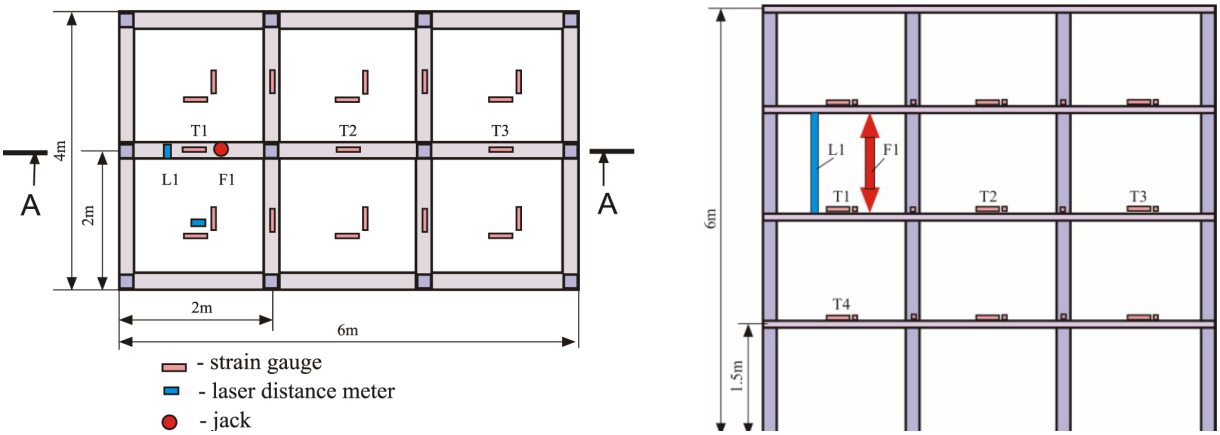

Figure 2. Scheme of load application and sensor location: second floor plan of model structure (left) and vertical section A-A (right).

of the sample are as follows: length 6 m, width 4 m, height 6 m. The model structure was designed based on the results of numerical simulation of the deformation processes in it, from an elastic state to inelastic one. These processes are accompanied by the occurrence and accumulation of cracks, formation of zones of damaged material in some parts of the structure and, finally, a complete loss of bearing capacity [28]. Analysis of the results of modeling made it possible to determine the dimensions and structural features of the model object, evaluate the mode and level of external loads. The deformation parameters, showing the greatest promise from the viewpoint of possibilities of recording subcritical and critical states, were identified, and the parameter ranges and accuracy of their recording were evaluated.

Creating an experimental sample took about 4 months. This included the development of a mathematical model, a numerical simulation of possible scenarios of elastic and inelastic deformation of the structure, and finally the sample manufacturing.

Now, the model structure is installed on the experimental stand. It is equipped with the following facilities.

– 12 hydraulic jacks are used to apply localized self-balanced force.

– 57 strain gauges are used to record deformations (gauges are distributed over the structure according to Figure 2).

– laser displacement sensors are used to record the relative displacements at the force application points (Figure 2).

– 24 one-component piezo-accelerometers are used to register the vibration response (gauges are distributed over the structure according to Figure 3, sensors are indicated by circles).

– A hammer equipped with an accelerometer is used to register a localized impulse force.

The deformation state of the structure during the experiment is controlled by an automated monitoring system. All measurement data are synchronized and collected in the monitoring database and go through primary mathematical processing. So, we obtain the opportunity of the online observation the deformation processes in the model structure during all stages of the experiment.

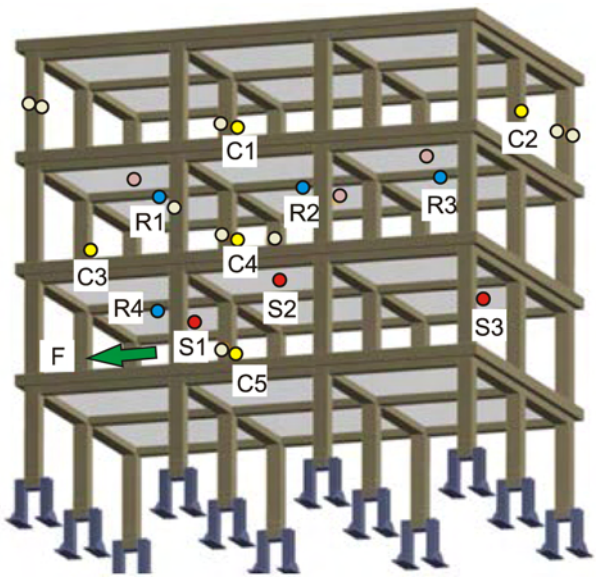

Figure 3. Scheme of accelerometer location.

3. Basic vibration portrait of the model structure

To study the dynamic processes in the model structure, it is necessary to know its vibration characteristics at the initial state. For this, we proposed to create a basic vibrational portrait of the structure. To obtain such information, a series of experiments was carried out. The experimental conditions were specified in such a way as to keep the structure in the elastic state. This was realized due to a reduced-impact mode in which the applied load could not cause inelastic deformation of its elements.

The vibration portrait is a set of information about the spatially distributed vibrational response of the structure to a series of test impulse impacts applied in its various parts. Having this information, we can compare it with the picture of the spatially distributed deformation response of the structure to certain external impact. Such comparison makes it possible to evaluate the change in the vibrational characteristics of the structure caused by a change in its deformation state, including the occurrence and accumulation of damage. Thus, it becomes possible to assess the magnitude and location of damage.

Obtaining the vibrational portrait of the structure is a complex procedure. The structure, which was under its own weight, was subjected to testing impulse force, which was applied sequentially at each basic element of the structure. Impact was produced by a hammer of 470 grams equipped with accelerometer. The force was applied to the surface of each vertical column in two perpendicular directions in the horizontal plane and to the floor slabs along the normal to their upper surface. The vibration response was recorded by a system of 24 accelerometers located on the columns, crossbars and floor slabs. The distribution of sensors by model structure is shown in Figure 3 (sensors are shown by circles). In total, 120 impulse forces were realized at different locations, and for each impulse a set of 24 vibrograms was obtained. Thus, we got 120 sets of 24 vibrograms which characterize spatial vibrational responses of the structure to 120 test impacts.

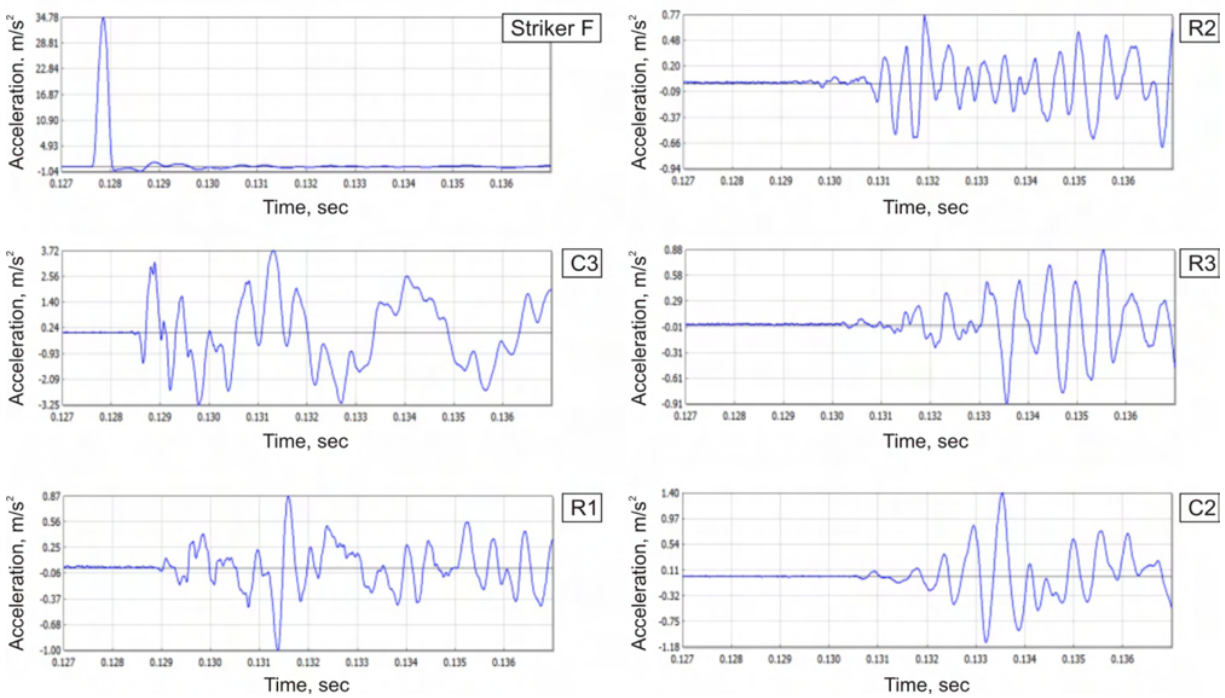

Figure 4. Acceleration vibrograms recorded on the striker and several sensors.

For each acceleration vibrogram, the corresponding Fourier and wavelet images were obtained. The total set of vibrograms and the results of their processing represent the basic electronic vibration portrait of the model structure. Composing the vibration portrait is a rather long procedure. In our case, it took about 1 month. But such number of measurements are necessary in order to describe the initial vibrational properties with sufficient accuracy. In addition, to generate statistically reliable data, it is advisable to perform this procedure repeatedly.

Figure 3 gives a schema of one test of this series. The point of application of test impulse force and its direction are shown by the arrow. Figure 4 presents vibrograms of accelerations in the direction normal to the surface of sensor attachment. The figure shows the data recorded by the striker sensor and sensors attached to 2 columns (C2, C3) and 3 crossbars (R1, R2, R3). Designation and arrangement of sensors correspond to Figure 3. Matching vibrograms clearly demonstrate the time of the wave front passage through each sensor and the delay of the wave front as the distance from the impact point increases.

The experimentally recorded pattern of the wave front propagation is in qualitative agreement with the results obtained by the numerical simulation [10]. Figure 5 displays the propagation of the displacement wave front caused by a localized impulse force applied at one ground floor column (result of simulation). The figure demonstrates the positions of the displacement wave front, which correspond to three successive instants of time, elapsed from the moment of impact: 0.36 ms, 1.1 ms and 2.4 ms. The histogram on Figure 5 compares the arrival times of the deformation wave front at some points of the structure obtained by the numerical simulation and during the experiment. These data were recorded by sensors

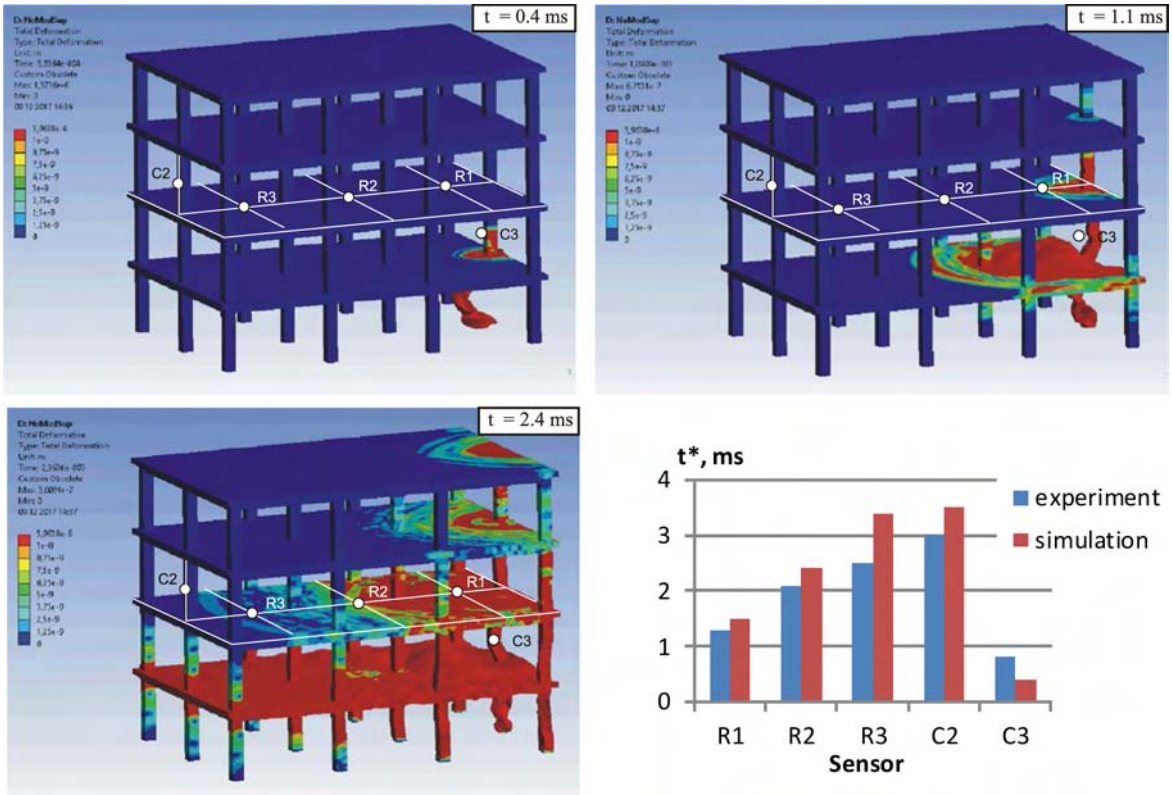

Figure 5. The displacement wave front in structural elements at three time instants and arrival time of the deformation wave at different points of structure.

located on three crossbars (R1, R2, R3) and two columns (C2, C3). The calculated and experimental data demonstrate a fairly good agreement.

Figure 6 shows several wavelet images of accelerations recorded by sensors located at different points of the structure. Designation of the sensors and their positions are indicated in Figure 3. The patterns clearly demonstrate the "lifetime" of free vibrations at different frequencies. The most long-lived vibrations have the frequency of ∼200 Hz. The vibration amplitudes for columns, crossbars and floor slabs differ significantly.

4. Quasistatic loading of the model structure

Thus, having complete information about the initial state of the model structure, we began to study its deformation response to static load. Here we demonstrate the results obtained by loading the structure in a low-impact mode in which deformations remain elastic.

First of all, the spatial deformation response of the structure to the applied localized self-balancing bursting force was studied. Static load F1 was applied by means of a jack, installed between two floor slabs (Figure 2). The loading was carried out stepwise, with increasing the load at each step and reset to zero before the next step. Figure 7 shows change in force F1 and corresponding changes in vertical

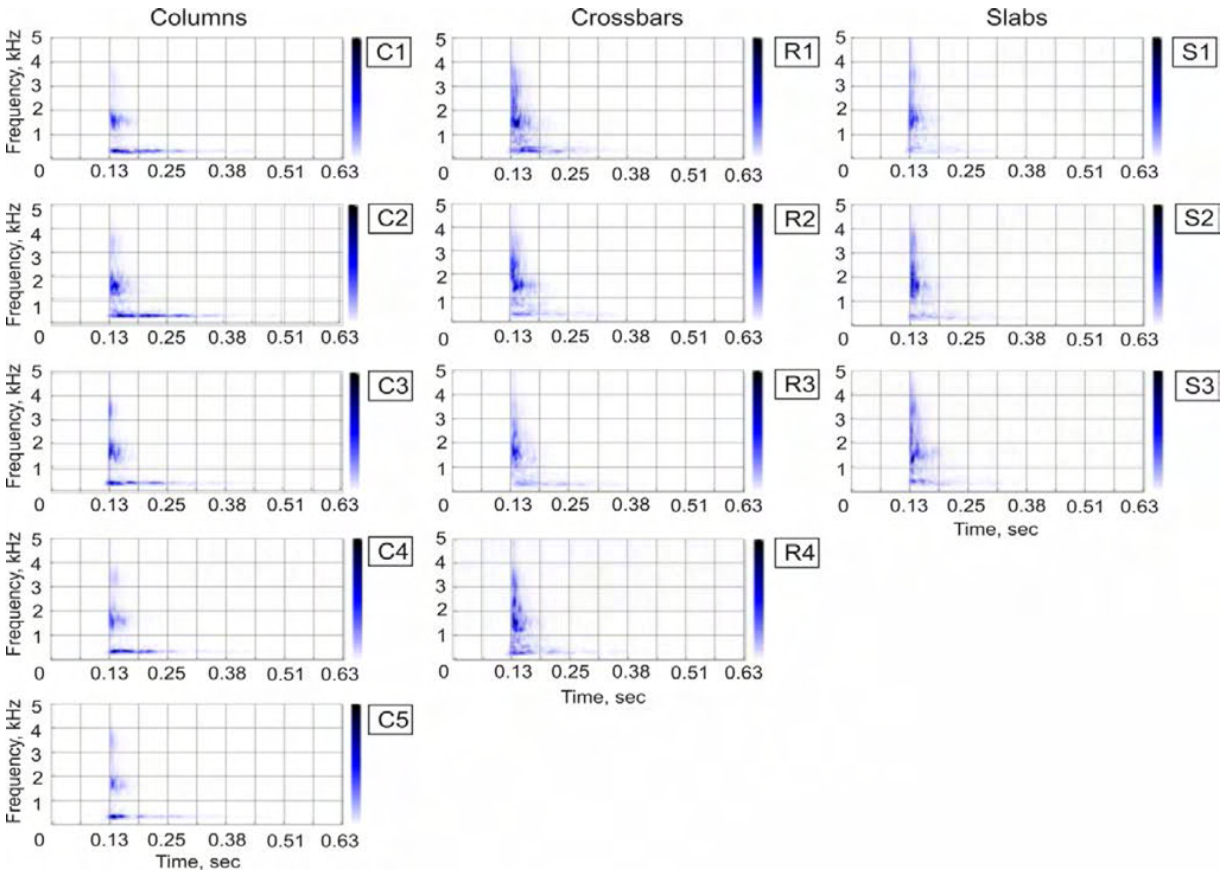

Figure 6. Wavelet images of acceleration vibrograms at different points of model structure.

displacement L1 in the vicinity of the loading point as well as deformation response of individual elements at the points T1–T4. Strain gauge notation corresponds to that given in Figure 2. Similar data were obtained for all points of the structure, equipped with strain gauges.

The above measurements were made for several quasi-static load arrangements. For all variants of loading we obtained the patterns of spatial distribution of deformations as well as the plots of deformation and displacement as a function of the applied force. An analysis of these graphs in Figure 7 shows that if the applied force is less than 20 kN, all structural elements remain elastic. As soon as the applied load exceeded 20 kN (this corresponds to the 5th loading step), the strain value in unloading state becomes non-zero. This fact indicates the beginning of inelastic processes in the structure. Comparing the graphs obtained from the sensors located at different distances from the jack, we can see that the strain decreases rapidly when the distance from the loading point increases. So, at a distance of 5 meters from the jack the strain level decreases by 30 times.

To study the dynamic properties of a structure subjected to static loading, we acted as follows. After each loading step, structural vibrations were excited at some points of the structure, and the acceleration vibrograms were obtained and compared with the vibrograms recorded prior to loading (vibrograms

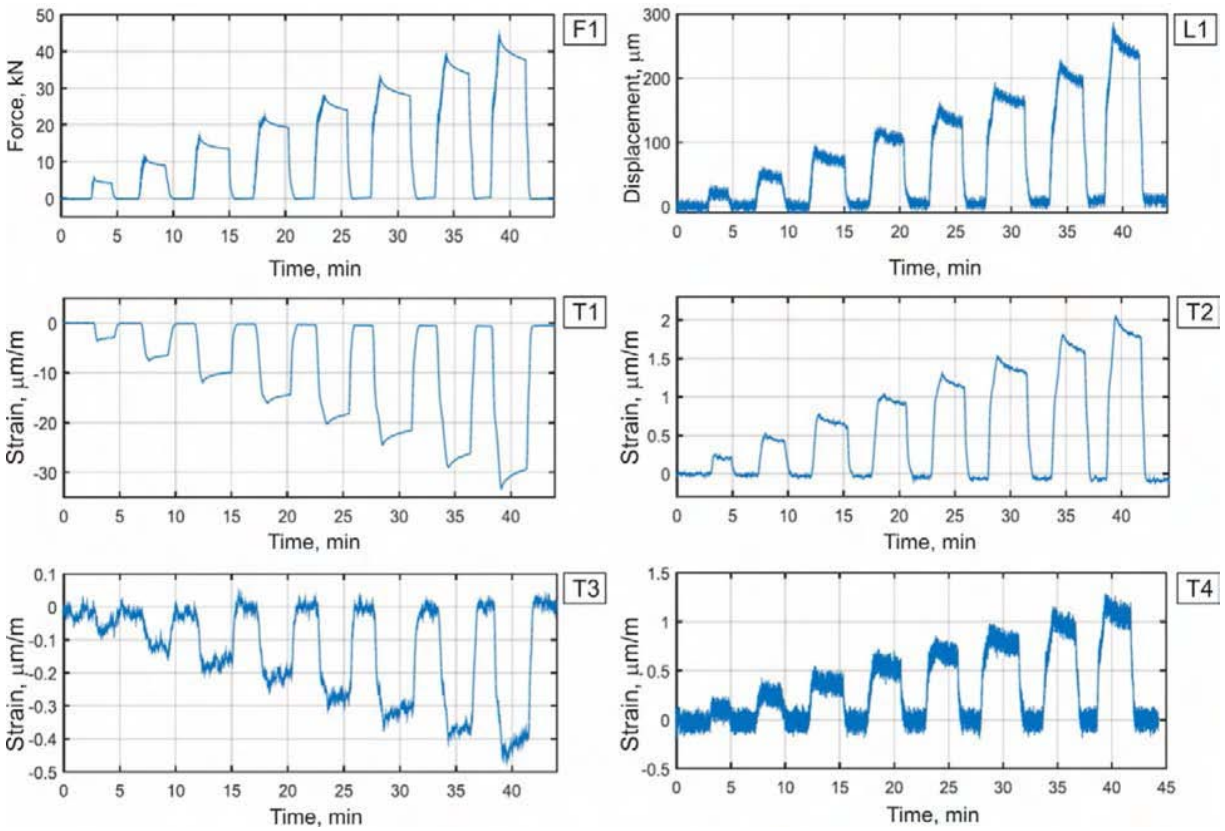

Figure 7. Changes in the applied force F1 and corresponding changes in the displacement L1 and strain at points T1-T4 of model structure.

from the basic vibration portrait). Figure 8 shows a diagram of half the sample with sensors and the vibrograms recorded by C4 sensor located on the column close to the jack. The position of the jack is shown by the red arrow, the position and direction of the pulse force is indicated by the green arrow. The vibrogram is normalized to the acceleration amplitude of the striker. The lower graph is a detailed image of the marked fragment of the upper graph. A comparison of the vibrograms taken from the basic vibration portrait and obtained after the third loading step shows that the difference is insignificant. Thus, we can conclude that the quasi-static loading in the low-impact mode does not significantly affect the dynamic deformation response of the structure to the external impulse loads. This fact is consistent with the current opinion that the "initial" stress state doesn't affect the dynamic behavior of a deformable system.

5. Conclusions

A review of information on modern test stands, which are used to study the deformation processes in large-scale building and engineering structures, showed that this line of research is in great demand and is actively progressing. On the one hand, this is connected with the tendency to create increasingly

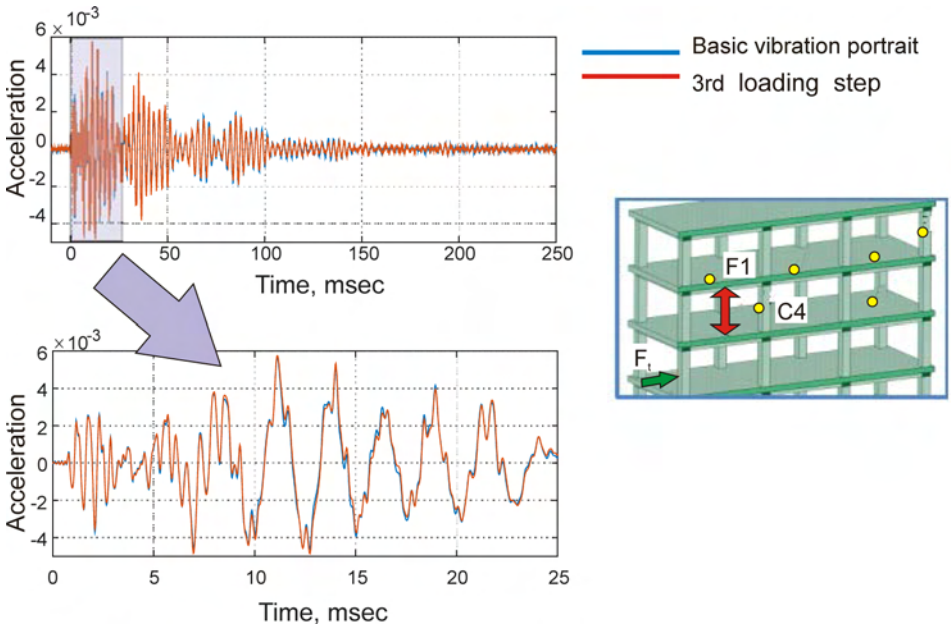

Figure 8. Vibrograms recorded by accelerometer C4 prior the loading and after the third loading step.

complex unique structures using new engineering materials and technologies. On the other hand, there is considerable progress in the development of experimental data recording systems, as well as the systems for processing large amounts of information. These circumstances significantly increase the informative value of experimental studies and gives impetus to the development of methods for the assessment of the stress-strain state of structures and prediction of their performance capacity.

The experimental stand created by the team of authors is aimed at studying the deformation processes in large-scale model structures, searching for precursors of failure, as well as elaborating criteria for establishing the pre-critical state of the structure. The research stand is designed and created as a tool for exploratory research. Our goal is to obtain fundamental knowledge about the patterns of the emergence of damage precursors, to develop the instruments for observations of early signs of destruction in structures of various configurations and from various materials. The stand is a multifunctional experimental site that allows you to explore the features of static and dynamic deformation processes in a variety of building and engineering structures.

Presented series of experiments demonstrates the capabilities of the experimental setup, which allows one to study deformation processes in large-scale objects with a multi-element structure, and dissimilar deformation interaction. The obtained results are as follows:

– A basic vibrational portrait of the model structure has been created, which provided basic information for the future experiments aimed at studying inelastic deformation of a structure until its ultimate failure.

– The deformation response of structural elements to the local self-balanced load specified in the loading-unloading mode has been studied. The spatial distribution of linear deformations over structural elements has been obtained under external loads applied at different points. It was shown that in the range of applied forces up to 20 kN, the structural elements experience elastic deformation.
– The dynamic response of structural elements to a locally applied impulse load has been studied. The patterns of the spatial-temporal distribution of deformation parameters over the structural elements have been obtained. The study has shown that the propagation of the deformation wave through the structural elements is of complex character. With regard to the characteristic times of propagation of the deformation wave over the structural elements, the obtained experimental data are found to be in good agreement with the results of numerical simulation.

The presented experiments allow us to accumulate unique data on the strength, reliability and durability of concrete structures under static and dynamic loads. These data are needed to understand the mechanisms of damage formation in concrete structures, to find precursors of failure, as well as to develop criteria allowing registration of the onset of the critical state.

Acknowledgements

The authors would like to acknowledge the Russian Science Foundation (project 9-77-30008), which funded this research.

References

[1] M. Al Heib, F. Emeriault, M. Caudron, et al., "Large-scale soil-structure physical model (1g): assessment of structure damages", *Int. J. Phys. Modelling in Geotechnics, ICE Virtual Library* **13**:4, 138–152.

[2] H. Dong, Q. Han, X. Du, and J. Wen, "Multiple shaking tables tests of seismic pounding effect of reinforced concrete bridge mode", *J. of Vibroengineering* **16**:7 (2014), 3565–3575.

[3] V. V. Epin, R. V. Tsvetkov, and A. P. Shestakov, "Application of feature recognition to hydrostatic leveling systems", *Meas. Tech.* **59**:4 (2016), 405–109.

[4] R. Esposito, F. Messali, G. J. P. Ravenshorst, et al., "Seismic assessment of a lab tested two storey unreinforced masonry Dutch terraced house", *Bull. Earth. Eng.* **17** (2019), 4601–4623.

[5] European Centre for Training and Research in Earthquake Engineering, http://www.eucentre.it. Accessed 3 Dec 2019.

[6] European Test Services (ETS) B.V., https://www.european-test-services.net/about.html. Accessed 3 Dec 2019.

[7] K. E. Frolov, "Experimental studies of reinforced concrete structures of hydraulic structures strengthened with composite materials", *Structural Mechanics of Engineering Constructions and Buildings* **15**:3 (2019), 237–242.

[8] R. Garcia et al., "Shake table tests on deficient RC buildings strengthened using post-tensioned metal straps", pp. 187–202 in *Seismic evaluation and rehabilitation of structures*, edited by A. Ilki and M. Fardis, Geotechnical, Geological, and Earthquake Engineering **26**, Springer, Dordrecht, 2014.

[9] Glenn Research Center, Facilities, https://www1.grc.nasa.gov/facilities/. Accessed 3 Dec 2019.

[10] I. O. Glot, V. P. Matveenko, R. V. Tsvetkov, et al., "Spatial-temporal distribution of deformation processes in a reinforced concrete structure under shock-wave action (calculation, experiment)", *Mech. Solids* **2**, 72–84.

[11] International Joint Research Laboratory of Earthquake Engineering (ILEE, Facilities, http://www.ilee-tj.com/en/data/list/tj%20u. Accessed 3 Dec 2019.

[12] N. Johnson, R. T. Ranf, M. S. Saiidi, et al., "Seismic testing of a two-span reinforced concrete bridge", *J. Bridge Eng.* **13**:2 (2008), 173–182.

[13] S. Kim and S. W. Choi, "Experimental and analytical investigation based on 1/2 scale model for a cleanroom unit module consisting of steel section and reinforced concrete", *Adv. Mater. Sci. Eng* **2016** (2016), art. id. 6920725.

[14] H. Lee, J. Min, and W. Chung, "Full-scale testing of precast concrete bridge using internal connector in negative moment region", *Adv. Civil Engng.* **2019** (2019), art. id. 6309859.

[15] S. Li, C. Cai Wu, and F. Kong, "Shaking table model test and seismic performance analysis of a high-rise RC shear wall structure", *Shock and Vibration, V.* **2019** (2019), art. id. 6189873.

[16] J. M. Lirola, E. Castaneda, B. Lauret, and M. Khayet, "A review on experimental research using scale models for buildings: application and methodology", *Energ. Buildings* **142** (2017), 72–110.

[17] D. Murià-Vila, A. R. Sánchez-Ramírez, C. H. Huerta-Carpizo, et al., "Field tests of elevated viaducts in Mexico City", *Struct. Eng.* **141**:1 (2015), art. id. D4014001.

[18] T. Nagae, W. M. Ghannoum, J. Kwon, et al., "Design implications of large-scale shake-table test on four-story reinforced concrete building", *ACI Struct. J.* **112**:2 (2015), 135–146.

[19] M. Nakashima, T. Nagae, R. Enokida, and K. Kajiwara, "Experiences, accomplishments, lessons, and challenges of E-defense-Tests using world's largest shaking table", *Jpn. Archit. Rev.* **1**:1 (2018), 4–17.

[20] National Center for Research on Earthquake Engineering, Laboratories, https://www.ncree.narl.org.tw/about/laboratory. Accessed 3 Dec 2019.

[21] J. A. Ortiz et al., "Full-scale experimental and numerical study about structural behaviour of a thin-walled cold-formed steel building affected by ground settlements due to land subsidence", *Proc. IAHS* **372** (2015), 141–144.

[22] A. Pinto, "Large scale testing", pp. 359–381 in *Earthquake engineering in Europe*, edited by M. Garevski and A. Ansal, Geotechnical, Geological, and Earthquake Engineering **17**, Springer, Dordrecht, 2010.

[23] J. A. Ramirez, "The George E. Brown, Jr. network for earthquake engineering simulation (NEES): reducing the impact of EQs and tsunamis", pp. 1–9 in *Experimental research in earthquake engineering*, edited by F. Taucer and R. Apostolska, Geological and Earthquake Engineering **35**, Springer, Switzerland, 2015.

[24] V. Sarhosis, D. Dais, E. Smyrou, et al., "Evaluation of modelling strategies for estimating cumulative damage on Groningen masonry buildings due to recursive induced earthquakes", *Bull. Earthquake Engng.* **17**, 4689–4710.

[25] S. V. Savkov and S. V. Demishin, "Center for complex seismic testing: current situation and prospects of development", Сейсмостойкое строительство: безопасность сооружений (*Earthquake Eng. Constr. Safety*) **2015**:5 (2015), 44–47. In Russian; English abstract at http://seismic-safety.ru/?q=article/376.

[26] SERA, Transnational access to European high-class laboratories, http://www.sera-eu.org/export/sites/sera/home/galleries/pdfs/SERA-TA-brochure.pdf. Accessed 3 Dec 2019.

[27] S. Shana, S. Lia, S. Xuc, and L. Xie, "Experimental study on the progressive collapse performance of RC frames with infill walls", *Engng. Struct.* **111** (2016), 80–92.

[28] I. Shardakov, I. Glot, A. Shestakov, et al., "A test stand for studying subcritical and critical states of full-size reinforced concrete structures", pp. 451–460 in *Advances in structural integrity: Proc. SICE 2016*, edited by R. Prakash et al., Springer Nature, Singapore, 2018.

[29] I. O. Toma and G. M. Atanasiu, "Modern trends in experimental earthquake engineering research", *Bull. Polytech. Inst. Jassy* **56** (60):4 (2010), 43–54.

[30] TSIAM: Central Institute of Aviation Motors, Experimental Facilities, https://ciam.ru/en/experimental-bases. Accessed 3 Dec 2019.

[31] T. Wang, Q. Chen, Z. H., and L. Zhang, "Experimental study on progressive collapse performance of frame with specially shaped columns subjected to middle column removal", *Shock and Vibration* **2016** (2016), art. id. 7956189.

[32] X. Weng and W. Wang, "Influence of differential settlement on pavement structure of widened roads based on large-scale model test", *Journal of Rock Mechanics and Geotechnical Engineering* **3**:1 (2011), 90–96.

[33] J. T. H. Wu, K. Ketchart, and M. T. Adams, "Two full-scale loading experiments of geosynthetic-reinforced soil (GRS) abutment wall", *Int. J. Geotech. Engng.* **2**:4 (2008), 303–317.

[34] A. S. Zolotcov, "Vibration tests on fragment of monolithic building unit destruction", *Magazine of Civil Engineering* **27**:1 (2012), 14–21.

Received 15 May 2020. Revised 22 Aug 2020. Accepted 9 Sep 2020.

IGOR SHARDAKOV: shardakov@icmm.ru
intelligent monitoring laboratory, Institute of Continuous Media Mechanics of the Ural Branch of Russian Academy of Science, 1, Akademic Korolev street, Perm, 614013, Russia

IRINA GLOT: glot@icmm.ru
intelligent monitoring laboratory, Institute of Continuous Media Mechanics of the Ural Branch of Russian Academy of Science, 1, Akademic Korolev street, Perm, 614013, Russia

ALEKSEY SHESTAKOV: shap@icmm.ru
intelligent monitoring laboratory, Institute of Continuous Media Mechanics of the Ural Branch of Russian Academy of Science, 1, Akademic Korolev street, Perm, 614013, Russia

ROMAN TSVETKOV: flower@icmm.ru
intelligent monitoring laboratory, Institute of Continuous Media Mechanics of the Ural Branch of Russian Academy of Science, 1, Akademic Korolev street, Perm, 614013, Russia

VALERIY YEPIN: epin.v@icmm.ru
intelligent monitoring laboratory, Institute of Continuous Media Mechanics of the Ural Branch of Russian Academy of Science, 1, Akademic Korolev street, Perm, 614013, Russia

GEORGIY GUSEV: gusev.g@icmm.ru
intelligent monitoring laboratory, Institute of Continuous Media Mechanics of the Ural Branch of Russian Academy of Science, 1, Akademic Korolev street, Perm, 614013, Russia

SUBMISSION GUIDELINES

ORIGINALITY

Authors may submit manuscripts in PDF format online at the Submissions page. Submission of a manuscript acknowledges that the manuscript is original and has neither previously, nor simultaneously, in whole or in part, been submitted elsewhere. Information regarding the preparation of manuscripts is provided below. Correspondence by email is requested for convenience and speed. For further information, write to contact@msp.org.

LANGUAGE

Manuscripts must be in English. A brief abstract of about 150 words or less must be included. The abstract should be self-contained and not make any reference to the bibliography. Also required are keywords and subject classification for the article, and, for each author, postal address, affiliation (if appropriate), and email address if available. A home-page URL is optional.

FORMAT

Authors can use their preferred manuscript-preparation software, including for example Microsoft Word or any variant of TEX. The journal itself is produced in LATEX, so accepted articles prepared using other software will be converted to LATEX at production time. Authors wishing to prepare their document in LATEX can follow the example file at www.jomms.net (but the use of other class files is acceptable). At submission time only a PDF file is required. After acceptance, authors must submit all source material (see especially Figures below).

REFERENCES

Bibliographical references should be complete, including article titles and page ranges. All references in the bibliography should be cited in the text. The use of BibTEX is preferred but not required. Tags will be converted to the house format (see a current issue for examples); however, for submission you may use the format of your choice. Links will be provided to all literature with known web locations; authors can supply their own links in addition to those provided by the editorial process.

FIGURES

Figures must be of publication quality. After acceptance, you will need to submit the original source files in vector format for all diagrams and graphs in your manuscript: vector EPS or vector PDF files are the most useful. (EPS stands for Encapsulated PostScript.)

Most drawing and graphing packages—Mathematica, Adobe Illustrator, Corel Draw, MATLAB, etc.—allow the user to save files in one of these formats. Make sure that what you're saving is vector graphics and not a bitmap. If you need help, please write to graphics@msp.org with as many details as you can about how your graphics were generated.

Please also include the original data for any plots. This is particularly important if you are unable to save Excel-generated plots in vector format. Saving them as bitmaps is not useful; please send the Excel (.xls) spreadsheets instead. Bundle your figure files into a single archive (using zip, tar, rar or other format of your choice) and upload on the link you been given at acceptance time.

Each figure should be captioned and numbered so that it can float. Small figures occupying no more than three lines of vertical space can be kept in the text ("the curve looks like this:"). It is acceptable to submit a manuscript with all figures at the end, if their placement is specified in the text by means of comments such as "Place Figure 1 here". The same considerations apply to tables.

WHITE SPACE

Forced line breaks or page breaks should not be inserted in the document. There is no point in your trying to optimize line and page breaks in the original manuscript. The manuscript will be reformatted to use the journal's preferred fonts and layout.

PROOFS

Page proofs will be made available to authors (or to the designated corresponding author) at a Web site in PDF format. Failure to acknowledge the receipt of proofs or to return corrections within the requested deadline may cause publication to be postponed.

Journal of Mechanics of Materials and Structures

Volume 15, No. 5 December 2020